A NOVEL MULTI-MODAL THERMAL FLOW SENSOR FOR BIOMEDICAL APPLICATIONS

Vasileios Kitsos

A thesis submitted to
University College London for the degree of
DOCTOR OF PHILOSOPHY

Supervised by
Dr. Xiao Liu
Professor Andreas Demosthenous

Department of Electronic and Electrical Engineering
University College London

DECLARATION

I, Vasileios Kitsos, confirm that the work presented in this thesis is my own. Where information has been derived from other sources, I confirm that this has been indicated in the thesis.

ACKNOWLEDGEMENTS

First, I would like to thank my first supervisor, Dr. Xiao Liu, for his guidance during my PhD. He was always willing to help and advice, and he offered me valuable insight in the field of electronics and experimental setup. Many thanks go to my second supervisor, Professor Andreas Demosthenous, for his support, guidance and technical suggestions that helped me complete my PhD. My gratitude goes to both of my PhD supervisors, who believed in me and provided me with the opportunity to pursue my PhD studies here at UCL.

Special thanks to UCL and the staff of the department who were always helpful to me, and to the Engineering and Physical Sciences Research Council (EPSRC) for their financial support throughout this PhD.

I would also like to thank all of my colleagues that made the daily life and atmosphere in the office pleasant and friendly. Special thanks to Evdokia Pilavaki, Matthew Schormans, Virgilio Valente, Arsam Shiraz, and Dai Jiang for their invaluable help and suggestions on the technical aspects of my work.

My special gratitude to my partner and to my friends, who always believed in me, supported and encouraged me during the hard times.

Lastly but most importantly, my deepest gratitude to my family for their unconditional love and support through all these years.

ABSTRACT

Heat and moisture exchangers (HMEs) are basic breathing system filters used by patients that have undergone tracheostomy and breathe through an airway hole at their neck called stoma. Their main function is to replace the normal humidification, warming and filtering of the inhaled air that used to be performed by the upper airways. Clinical evidence show the beneficial operation of the HME, however, there are patients who complain about difficulty in breathing while using it. Although efforts in clinical environment to assess HME's performance in terms of humidity, temperature, and filtering have been already conducted, the market currently lacks of a portable solution that can effectively measure the breathing pattern of the patient in situ. This thesis proposes novel methods and circuits towards thermal flow sensors intended for the in situ monitoring of the tracheostomee's respiration. This work addresses the two main restrains for a flow sensor of that purpose: power consumption and, safety concerns due to potential elevated temperatures at the sensor. Thermal flow sensors can operate in different modes, such as constant power (CP), constant temperature (CT), and constant temperature difference (CTD). While other published or commercial flow sensors operate in one of the pre-defined modes, the proposed sensor is able to toggle between modes avoiding high-temperature overshoots at low flow rates by using CP, and avoiding high power consumption at high flow rates by using CTD. Specifically, an overtemperature reduction up to 9.5% is achieved, and a heater power reduction up to 13.6%. This is the first dual-mode thermal flow sensor to operate in CP/CTD. Moreover, mechanisms for the accurate control of the CP, CT, and CTD are introduced to ensure better accuracy and reproducibility of the measurements. The issue of power consumption and output sensitivity are also addressed by modifications on the transducer; specifically, the effect of the temperature sensing elements' location on flow sensor's performance is investigated. This work proves that optimisation of the distance between the heater and the temperature sensing elements is required to achieve optimal sensitivity, and provides evidence of the interplay between power consumption and optimal distance. Based on the findings, a novel figure of merit that can be applied to any mode is proposed. Finally, this thesis provides experimental evidence that the output sensitivity for flows

greater than the turn-over point can be increased by placing the temperature sensors asymmetrically. For the current setup, sensitivity has been increased up to 6 times. That is an important breakthrough since flow rates greater than turn-over point can now be included in the measurement range without any increase in power.

IMPACT STATEMENT

Laryngectomy is the removal of the larynx and the separation of the upper and lower respiratory tracts. It is usually performed in the case of laryngeal cancer, and it includes tracheotomy, the incision and the opening in the trachea for the creation of an airway hole called stoma, which the patient uses to breathe without the use of the nose or mouth. Nevertheless, the by-pass of the upper respiratory tract and the use of the stoma create a variety of problems, such as involuntary cough, and forced expectoration; therefore, heat and moisture exchangers (HMEs) for tracheostomees have been already developed to alleviate patients from tracheostomy's side-effects. HMEs are basic breathing system filters for replacing the normal humidification, warming, and filtering of the inhaled air that used to be performed by the upper airways. Clinical reports suggest that HME users see a significant improvement in their daily life, nevertheless, many of those report difficulty in breathing. Literature suggests a significant increase in tidal volume, and in inhalation and exhalation breath lengths, due to increase in flow resistance. It is also suggested that this increase in breathing resistance might not be sustained for long periods by patients with severe chronic obstructive pulmonary disease; hence, the potential side-effects of an HME must be fully investigated. Therefore, a device capable to evaluate the operation and the efficiency of the HME quantitatively by monitoring in situ not only the temperature and relative humidity, but also the flow rate, is required.

Currently there is no commercial device as such. This work consists part of the project for the development of an inexpensive post-laryngectomy airway climate explorer (ACE) for the assessment of flow rate, temperature and humidity, and the influence of the HME. This ACE will carry three different sensors, a flow rate, a temperature and, a relative humidity sensor to evaluate the aforementioned parameters in a reliable and safe manner. The measurements would provide significant information not only for the patient, but also for the clinicians and the HMEs' manufacturers.

This thesis focusses on the newly-introduced for this application, and most challenging of the sensors, the flow sensor. Thermal flow sensors offer electronic

simplicity, reliability, and integration capability. Nevertheless, they are power hungry, while they might develop high temperatures that could cause discomfort, or even burn, when placed close to human tissue. This thesis presents simulations, designs, and experimental results of methods and novel electronic circuits which address the issues above. Optimisation techniques of the relative position of the sensor's elements are presented, ensuring maximum sensitivity for the available power. Power minimisation is experimentally achieved without compromising measurement range. In addition, a novel combinatory logic on how the power should be delivered on the heating element is proposed.

Although the primary focus of this work is towards the evaluation of HME's impact on respiratory pattern, the proposed solutions can be implemented on any flow sensor with power and/or safety restrictions, such as the measurement of inflammable gasses.

TABLE OF CONTENTS

LIST OF FIGURES

LIST OF TABLES

ABBREVIATIONS

AUX	Auxiliary
ACE	Airway Climate Explorer
CC	Constant Current
CMOS	Complementary Metal Oxide Semiconductor
CMRR	Common Mode Rejection Ratio
COPD	Chronic Obstructive Pulmonary Disease
CP	Constant Power
CT	Constant Temperature
CTD	Constant Temperature Difference
CV	Constant Voltage
DAC	Digital-to-Analog Converter
DAQ	Data Acquisition
DEMUX	Demultiplexer
ETT	Endotracheal Tube
FEA	Finite Element Analysis
FoM	Figure of Merit
HME	Heat and Moisture Exchanger
IC	Integrated Circuit
I^2C	Inter-Integrated Circuit
IN-AMP	Instrumentation Amplifier
MCU	Micro-Controller Unit

MFC	Mass Flow Controller
NMOS	N-Type Metal Oxide Semiconductor
OP-AMP	Operational Amplifier
PCB	Printed Circuit Board
PWM	Pulse Width Modulation
RTD	Resistance Temperature Detector
SEM	Scanning Electron Microscope
SLM	Standard Litres per Minute
SMD	Surface Mount Device
TB	Temperature Balance
TCR	Temperature Coefficient Resistance
TOF	Time-of-Flight
TS	Temperature Sensor
UI	User Interface

1

INTRODUCTION

Larynx is the organ in the neck placed at the end of pharynx, at the point where it is divided into the trachea and the esophagus and, it is a set of cartilages and muscles that also includes the vocal cords. It is involved in breathing, sound production and it protects the trachea from food or water swallowing. The breathing air always passes in and out through the larynx during inhalation and exhalation, while the respiratory muscles move the cords apart to facilitate breathing. To produce speech, the cords are stretched and the air that passes through creates vibrations in order to produce the right sound. As far as ingestion is concerned, the larynx is elevated while swallowing and with the help of a spoon-shaped, elastic cartilage named epiglottis, the path to trachea is closed to prevent lungs from food or water ingestion. Fig. 1.1 shows the anatomy of the respiratory tracts.

However, there are cases where cancer is developed in the larynx due to changes in the cells at that particular area, known as laryngeal cancer. The causes of this type of cancer are not completely clear but evidence show that smoking, alcohol and exposure to certain chemicals increase the risk. Statistics suggest that people who drink substantial amount of alcohol in a regular base are about three times more likely to develop laryngeal cancer, while people who smoke at least 25 cigarettes per day or have smoked for more than 40 years are about 40 times more susceptible [1].

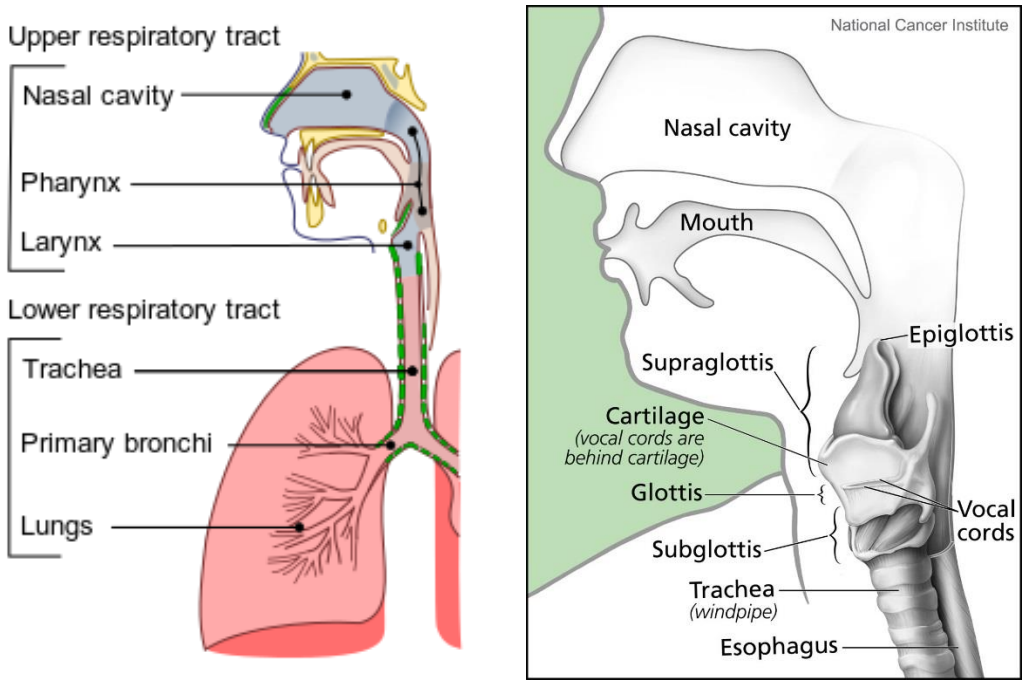

Fig. 1.1: (Left): the anatomy of both, the upper and lower, respiratory tracts. (Right): a more detailed illustration of the upper respiratory tract.

This type of cancer develops in the vicinity of the vocal cords, therefore, the change in the sound of a patient's voice is among the first and most noticeable symptoms. Other symptoms are persistent including cough, difficulty in swallowing and swelling in the neck. Yet, since these symptoms are the same as those of other common conditions, the diagnosis of the cancer is sometimes delayed. In the UK alone, there are about 2,300 new cases of this type of cancer each year, 39,900 in Europe, and 157,000 worldwide; hence, even it is not the most prevalent type of cancer, it does affect a great number of people [2].

Laryngectomy is the removal of the larynx and the separation of the upper and lower respiratory tracts. This separation is necessary since the larynx is in charge of isolating the trachea from the throat during ingestion. Hence, if the larynx is removed and the lower tract is not separated from the upper, food or water might reach the lungs. Laryngectomy is a procedure usually performed in the case of laryngeal cancer, and it includes tracheotomy, the incision and the opening in the trachea for the creation of an airway hole known as stoma (Fig. 1.2). The stoma serves as an airway allowing the patient to breathe without the use of the nose or mouth and the upper respiratory path in general.

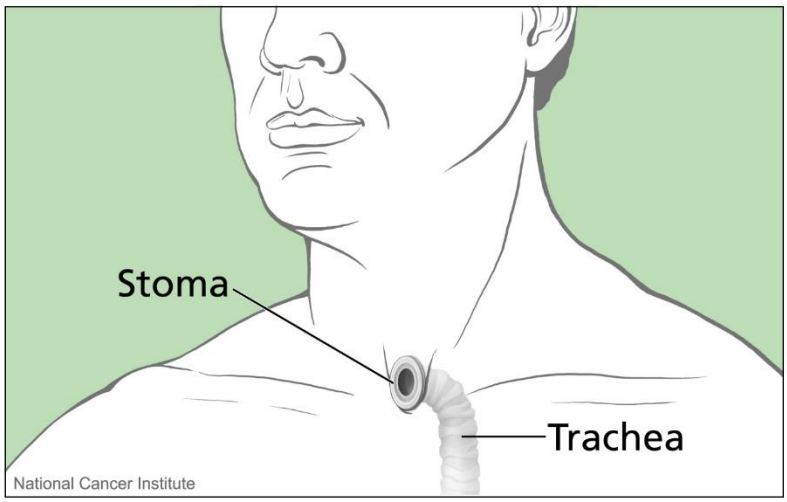

Fig. 1.2: Illustration of the end result of a tracheostomy. Upper respiratory tract is by-passed and patient now breathes through the stoma.

Apart from laryngeal cancer, there is a great list of other reasons when tracheostomy is performed such as epiglottitis or croup infection, severe neck or mouth injuries, chest muscles or diaphragm dysfunction and, anatomical abnormalities of the respiratory path. Also, temporary tracheostomy is conducted in patients in intensive care units (ICUs) in case of long stay.

1.1 The Effect of Heat and Moisture Exchangers

The upper respiratory tract function is basically to trap small particles like pollen and dust through the secretion of mucus and to remove them from the respiratory passage. Apart from filtering, the upper respiratory tract is also in charge of moisturizing and warming the inhaled air before it reaches the lungs. Therefore, the by-pass of the upper airways and the use of stoma to breathe create a variety of problems, with most of the patients who undertook surgery complaining about involuntary cough, sputum production and forced expectoration [3].

Thus, heat and moisture exchangers (HMEs) for ventilated and/or spontaneously breathing patients have been already developed to counter the side-effects of the tracheotomy and reduce the symptoms mentioned above. HMEs are basic breathing system filters for replacing the normal humidification, warming, and filtering of the inhaled air that used to be performed by the upper airways. In most cases, the principle

of their operation is to reserve a part of the heat and moisture of the exhaled air to use it as heated humidifier for the inhaled air that will follow, while at the same time, the air is filtered from possible harmful substances and the stoma is kept clean.

Patients who use an HME report less coughing, less mucus production and less stoma cleaning and, generally, a substantial improvement in their daily life [4]. However, the HME is a quite basic and simple device in structure and operation, without any elaborate mechanism. The goal of the HME is to mimic the functionality of the upper respiratory system, nonetheless, there is no feedback mechanism to provide the necessary information to quantify the HME's efficiency. The HME does not simulate the upper respiratory tract's operation to full extent since it is a passive device that does not provide extra humidity and/or heat; it only tries to maintain the existing ones to a satisfactory level for a short period of time (maximum a day), thus, its efficiency is reduced with time. Moreover, although reports show an unquestionable improvement of patient's life, these are only based on qualitative measurements subject to each patient's opinion.

Although clinical evidence show the beneficial operation of the HME [5], in situ physical effects have not been studied extensively. Hence, it becomes apparent that a mechanism should be devised in order to check the operation and the efficiency of the HME quantitatively by monitoring the different parameters of the respiration, such as temperature, relative humidity and flow rate of the incoming/outcoming air. The latter parameter is particularly important; although the positive impact of the HME on temperature and humidity is unquestionable, patients report an increase in breathing resistance when HME is used. In fact, studies show a significant difference on inhalation and exhalation length with and without HME [6], and it has been suggested that the increase in breathing resistance might not be sustained for long periods by patients with severe chronic obstructive pulmonary disease (COPD) [5].

1.2 Current Solutions for the Evaluation of HME's Efficiency

Currently there is no commercial device for the assessment of either temperature, humidity or flow rate of the trachea after tracheostomy. However, there are studies in

literature that evaluate the efficiency of the different commercially available HMEs [7][8]. These research experiments have been conducted on laryngectomized patients in controlled environment for better assessment of the parameters of interest. However, the structures used for this purpose, usually known as airway climate explorer (ACE), are sizeable and cumbersome devices that can be only used in clinical environment [9]. Consequently, this methodology sets certain limitations, such as reduced number of available participants, and respiration under certain clinical conditions and patient's conscious control. In other words, those studies were conducted with a small portion of patients and only for voluntary respiration in clinical environment, compromising the universality of the results.

On the other hand, devices that mimic the lungs' operation have been constructed. Fig. 1.3 presents a modified version of the International Standards Organisation (ISO) 9360 test apparatus, used for the evaluation of four popular at that time HMEs that can be found on the market. A lung model has been built comprising two rubber lungs in a chamber, a piston ventilator and a heated water bath. The whole apparatus imitates the operation and the environment of the lungs; therefore, the temperature and relative humidity of the water bath are constant at 34^{o}C and 100%, respectively. The apparatus is placed on a scale to measure the weight loss from the water bath, thus, the drop in humidity.

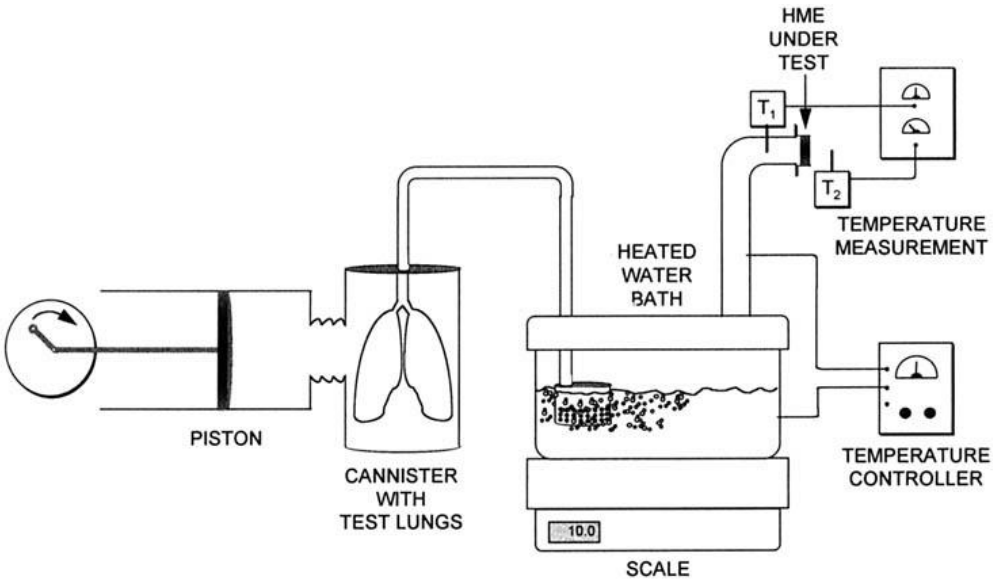

Fig. 1.3: [10] Drawing depicting the modified ISO 9360 test apparatus

Evidently, this is a cumbersome and expensive structure for the assessment of HMEs' efficiency. Furthermore, the measurements are not in situ but they are produced by a mechanism that mimics the operation and environment of the lungs. Hence, although it might be useful to compare the performance of different HMEs, the actual usefulness and efficiency of each one separately and in situ is hard to be determined.

1.3 PROPOSED SYSTEM AND THESIS GOALS

This work is part of a project for the development of a post-laryngectomy ACE for the assessment of flow rate, breathing rate, inhaled air temperature and humidity, and the influence of the HME. To achieve that, a system-on-chip that incorporates three different sensors, a flow rate, a temperature and a relative humidity sensor should be designed, to evaluate the aforementioned parameters in a reliable and safe manner. The entire system will provide a portable solution, able to be mounted on the HME, while addressing the main problems explained regarding the assessment of HME's efficiency. The measurements would provide significant information not only for the patient, but also for the clinicians and the HMEs' manufacturers.

The humidity and the temperature sensor of the system are not going to be investigated in this thesis, hence the work presented here focusses on the most challenging of the sensors, the flow sensor. A flow sensor that makes use of thermal principles to determine flow rate has been chosen, mainly due to its electronic simplicity, reliability, and integration capability. Nevertheless, thermal flow sensors make use of heaters, hence, they are power hungry, especially when a wide measurement range is required, while they might develop high temperatures that could cause discomfort, or even burn, if they are placed close to human tissue.

This thesis presents simulations, designs, and experimental results of methodologies and novel electronic circuits which address the aforementioned issues of thermal flow sensors. Optimisation techniques of the relative position of the flow sensor's elements for the flow range of human respiration are presented, ensuring maximum sensitivity for the available power. Power minimisation is also achieved experimentally by making parts of the output range, which are rarely used in the

literature, functional. In addition, a novel combinatory logic on how the power is delivered on the flow sensor's heating element is proposed, that is capable of ensuring low enough temperatures while maintaining a low power budget on high velocities of air.

To facilitate the flow sensor's prototyping and testing, the proposed methods and designs have been implemented using off-the-shelf components. Nevertheless, it will be apparent in this thesis that miniaturisation is not only feasible, but it will also produce an even more low-power flow sensor. Miniaturisation eventually will be required towards the development of the post-laryngectomy ACE.

Although the application of this work is in respiratory monitoring, the same designs and principles could be implemented in any thermal flow sensor regardless of the application, towards low-power and biomedically safe operation [11][12].

1.4 ORIGINAL CONTRIBUTIONS

The work reported in this thesis provides the following original contributions to the research of thermal flow sensors:

1. A review of the different topologies and operation modes of the thermal flow sensors, including the main technological trends of this field. (Chapter 2)

2. An optimisation method of the distance between the heater and the other sensing elements of a thermal flow sensor, to achieve a broad measurement range with minimum power consumption. (Chapter 3)

3. First time experimental evidence that usually disregarded parts of the output range can become functional with the use of asymmetrically located sensing elements. (Chapter 3)

4. Design and implementation of topologies that have not been used before for thermal flow sensors to establish the sensor's operating mode. (Chapter 4)

5. A novel multi-modal system of how the power is delivered to the heater,

ensuring lower temperatures in low flows, and lower power consumption in high flows. (Chapter 5)

Although the application of the work is in the biomedical field, the same designs and principles could be implemented in all thermal flow sensors, regardless of the application.

1.5 AUTHOR'S PUBLICATIONS

The work presented in this thesis has led to the following publications:

Journals

V. Kitsos, A. Demosthenous, and X. Liu, **"A Smart Dual-Modal Calorimetric Flow Sensor,"** *submitted to IEEE Sensors Journal*, May 2019.

Conferences

V. Kitsos, M. Schormans, A. Demosthenous, and X. Liu, **"Asymmetrical Sensing Configuration for Improved Sensitivity in Calorimetric High Flow Measurements in Constant Power Mode,"** in *IEEE SENSORS*, 2018, pp. 1–4

V. Kitsos, S. West, A. Demosthenous, and X. Liu, "**Design Considerations and Optimization of Calorimetric Flow Sensor for Respiratory Monitoring,"** in *IEEE Biomedical Circuits and Systems Conference (BioCAS)*, 2016, no. 2, pp. 26–29

1.6 THESIS OVERVIEW

This thesis is organised into 6 chapters.

Chapter 1 provides the motivation and the intention of this work. Specifically, it provides a brief introduction to the laryngeal cancer, its side-effects on the patients and how those side-effects are confronted using the HMEs. It also provides the proposed system and how the work presented in this thesis contributes towards that

goal.

Chapter 2 provides a description of the fundamental principles and the classification of the thermal flow sensors. That is important for the reader in order to understand how a low-power, high-sensitive thermal flow sensor can be possibly materialised, especially for the case of respiratory monitoring.

Chapter 3 investigates the effect of the relative position of flow sensor's elements on the sensitivity and the output range of the flow sensor, without further power increase. That is of great importance considering that high sensitivity and large output range is usually achieved in the literature by increasing the power consumption or by using expensive post-processing techniques. The results presented are derived by both computational modelling using the Comsol Multiphysics simulation software and experimental methods, showing a six-fold sensitivity increase.

Chapter 4 introduces new heater control circuit designs with appreciable benefits, such as better compliance with fundamental equations (King's Law), in order to achieve a better accuracy and repeatability. A novel multi-modal design is also introduced, promising lower power consumption and temperatures.

Chapter 5 provides experimental measurements and analysis of the designs introduced in the previous chapter. An overtemperature reduction up to 9.5% and a power reduction up to 13.6% has been achieved. It also evaluates the effect of sensing elements' position presented in chapter 3 on the current setup, confirming the sensitivity increase for high flow rates.

Chapter 6 presents an overview of this work, its impact and important results. In addition, possible future directions for further enhancement and miniaturisation of the thermal flow sensor are discussed.

2

PRINCIPLES AND ADVANCES OF THERMAL FLOW SENSORS

Flow sensors play an important role in various fields such as industrial processes, environmental monitoring [13] and in medical diagnostics [14][15]. In fact, flow sensors are widely used in medicine for measuring respiratory flows. The purpose of their use vary from routing monitoring, such as for mechanically ventilated patients [16], to early diagnosis of certain diseases or medical complications, such as asthma [17]. The majority of the flow sensors found in literature are thermal flow sensors. This chapter explains the popularity of this category of flow sensors, and provides a description of the fundamental principles and their classification. The purpose of this chapter is for the reader to understand their operation, familiarise with the state-of-art, and realise the topics that still need to be improved toward a portable, highly sensitive flow sensor for respiratory monitoring.

.

2.1 THE BENEFITS OF THERMAL FLOW SENSORS

The principle of a flow measurement can be based on a variety of topologies and techniques and it can be divided into two main categories based on the principle of their operation: thermal [18][19] and non-thermal [20][21][22] flow sensors. Some of the non-thermal topologies do have some unique advantages such as broad range or, two-phase flow measurement capability. However, they are usually more complex in fabrication, hence, they can be expensive and mass production is not simple. Also, their measuring dependence on mechanical moving parts leads to performance degradation over time due to mechanical wear.

On the other hand, thermal flow sensors have no moving parts, consisting of heating elements (heaters) and, most of the times, temperature sensing elements. Those elements are already available and easy to implement, even in standard CMOS technology, or as off-the-shelf components; hence, their implementation and fabrication is inexpensive compared to that of the non-thermal flow sensors, and mass production is facilitated. In addition, considering that the measurement of a physical property such as that of the flow, requires an electronic readout circuit that will transform the measured value to an electrical signal, the implementation of the sensor in CMOS facilitates the readout integration since the sensing elements and the readout circuit can be fabricated on the same substrate.

Nevertheless, designing a thermal flow sensor is a challenging task due to the complex multi-physics phenomena that take place, such as heat transfer and fluid dynamics. Therefore, analytical solutions are not always feasible, and numerical models are not always accurate [23], hence, in the vast majority of times a thermal flow sensor must be experimentally characterised and tuned accordingly to achieve the desired performance. Additional disadvantages of the thermal flow sensors are that they might suffer from non-linearity at the output, and that they can be power hungry due to heater's use. Nonetheless, thermal flow sensors are the prevalent topology in the literature due to their structural and electronic simplicity, and their long term reliability.

2.2 FUNDAMENTAL THERMAL FLOW SENSOR'S TOPOLOGIES

To measure flow, thermal flow sensors make use of the effect of fluid's velocity on a heating element or the area around the heater. Based on the exact topology of heater and/or temperature sensor, thermal flow sensors can be also categorised into three main groups [18][24]:

- Time-of-flight
- Hot-wire (or hot-film)
- Calorimetric

2.2.1 Time-of-flight

Typically, time-of-flight flow sensors consist of a heater, and a temperature sensor at a known distance, *D*, from the heater [25][26], as Fig. 2.1 depicts. To measure the flow rate, this topology makes use of the propagation time of a heat pulse generated at the heater to reach the temperature sensor. Time-of-flight flow sensors have been reported for the first time by Yang and Soeberg [27]. It was then van Kuijk et al. [28] that created a model to predict the expected propagation time for a flow measurement as:

$$TOF = \frac{-2a + \sqrt{4a^2 + v^2 D^2}}{v^2} \tag{2.1}$$

where TOF (time-of-flight) is the propagation time, α is the thermal diffusivity of the fluid in m^2/s, *D* the distance between the heater and the temperature sensor in metres, and v the fluid's velocity in m/s.

The great benefit of this topology is the linear relationship between the flow's velocity, v, and the inverse of the propagation time, 1/TOF, facilitating the measurement readings and, reducing the complexity of a possible readout circuit. Secondly, the flow direction information is also feasible by placing two temperature sensors, instead of one, one at each side of the heater [29]. However, the flow measurement is strongly dependent on the properties of the fluid and specifically on the fluid's thermal diffusivity, as shown in equation (2.1). Therefore, accurate flow

measurements can be only acquired for a known fluid of a stable composition. That is an important drawback that makes time-of-flight flow sensors less practical and explains the reason why they are less popular compared to the rest of the topologies described below.

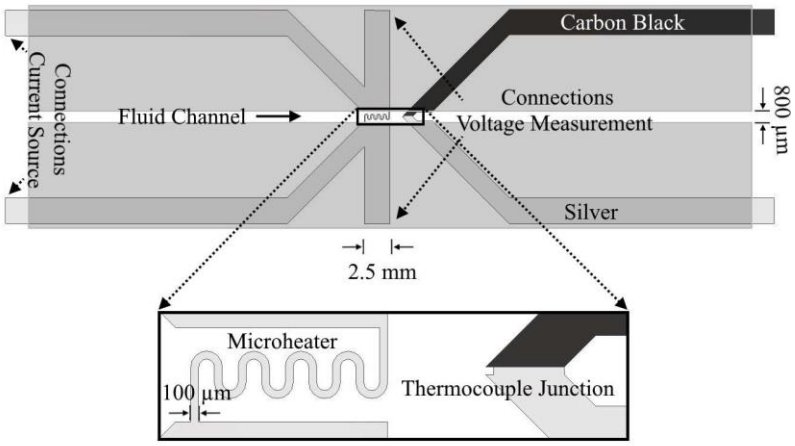

Fig. 2.1: A time-of-flight thermal flow sensor by Offenzeller et al. [30]. A microheater and a thermocouple are placed at flow's direction as a heating and a temperature sensing elements, respectively.

2.2.2 Hot-wire (Hot-film)

The second type of thermal flow sensor presented is the hot-wire, or hot-film [31], anemometer. This is probably the simplest topology of all three since it only consists of a heating element, either a heated wire or a heated surface (film) [32], immersed in the fluid. As the fluid passes over the heater, thermal energy is carried away from the heater due to convection, and it is proven that the amount of the convective thermal energy increases as the fluid's velocity increases. The effect of the flow, either on the supplied power or, on heater's temperature, determines the velocity of the fluid. This effect has been experimentally quantified for the first time by King [33] in 1914. His experiments and studies led to the equation below that commonly used in thermal flow sensors and usually referred as King's law:

$$\frac{P}{T_H - T_\infty} = A + B\, v^n \tag{2.2}$$

P: power consumed by the heater

T_H: heater's temperature, assuming it is homogeneous

T_∞: initial fluid's temperature, unaffected by heater

v: fluid's velocity

A, B, n: constants dependent on fluid's properties, and on flow sensor's geometry and materials. The value of n is usually in the range of 0.5, but values in the range of 0.7 has been also experimentally found [34].

The temperature difference between the fluid and the heater $T_H - T_\infty$, can be found in literature as *overheat* or *overtemperature*, and represented as T_{OVER}. It is also represented in some literature as ΔT. For the sake of clarity, T_{OVER} only is going to be used in this thesis for this particular temperature difference, while ΔT will be reserved for a different parameter presented later in this chapter.

Equation (2.2) clearly shows that the flow can be determined by measuring the overtemperature in a topology where the power is kept constant, or by measuring the consumed power by the heater in a topology where the overtemperature is constant. A qualitative illustration of a hot-wire/hot-film anemometer's output for both cases can be seen in Fig. 2.2.

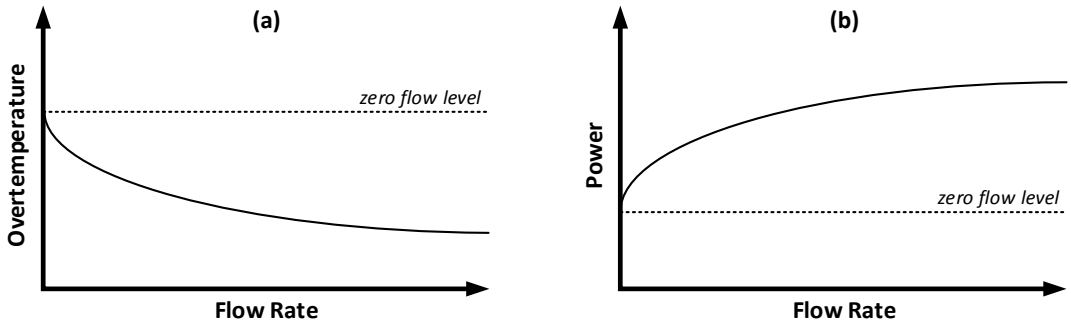

Fig. 2.2: Output representation of the expected output of a hot-wire/hot-film anemometer operating by keeping constant its (a) power, and (b) overtemperature.

From this point, the words "hot-wire" and "hot-film" will be used interchangeably in this thesis and both will refer to both topologies, since both share the same principle of flow sensing.

The development of the first hot-wire anemometer cannot be accurately determined [35]. Nevertheless, the first anemometer in silicon has been presented in

1974 by van Putten [36]. From that point, a great amount of micromachined hot-wire flow sensors have been published either for different applications [37][11], or to address certain issues of the hot-wire topology [38][39]. The greatest benefit of hot-wire flow sensors is the electronic and structural simplicity, which makes their implementation straight-forward. However, the flow measurement is still dependent on fluid's properties as (2.2), diminishing the topology's practicality. In addition, when a wire is used instead of a film as a heater, it might be prone to mechanical shock and fracture in case of fast velocities. Nonetheless, hot-wire remains probably the prevalent thermal flow sensor due to the easy and low-cost implementation. Fig. 2.3 shows two already published flow sensors: a hot-wire flow sensor that makes use of a wire for wire-bonding as a heating element, and a hot-film flow sensor. Although both have the same principle of operation, they have their own advantages and disadvantages in terms of power, consumption, sensitivity, and mechanical strength. Those aspects will be discussed later in this chapter.

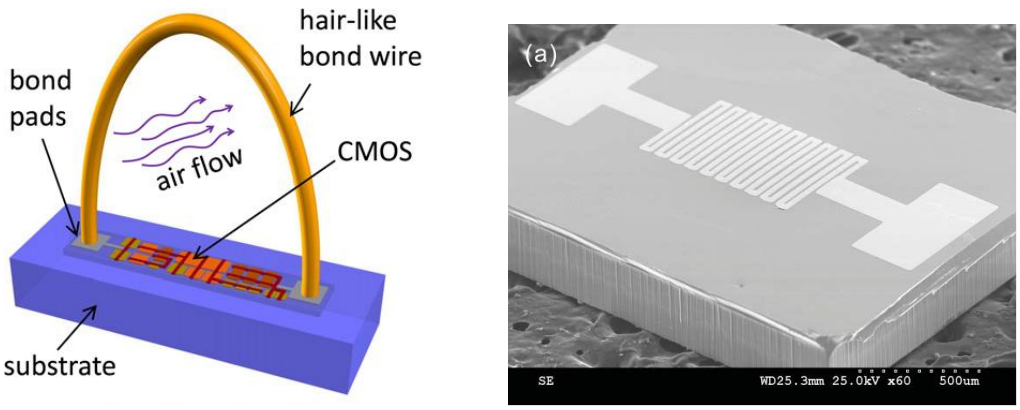

Fig. 2.3: (Left): [40] an illustration of a low-cost, hot-wire flow sensor using gold wire intended for wire-bonding as a heater. (Right): [31] an SEM photo of a hot-film sensor.

2.2.3 Calorimetric

The third type of thermal flow sensor, and the one where this thesis is focussed on, is the calorimetric flow sensor. This topology suggests an improved version of the hot-wire principle, and it consists of a central heating element and two equally spaced temperature sensors, one at the upstream and the other one at the downstream of the flow. Its operation is based on the flow-induced temperature gradient. In other words,

the heater creates a symmetrical heat distribution around it under no-flow conditions and, as a result, the temperature sensors ideally sense the same temperature. Yet, when flow occurs, this thermal distribution alters and a thermal gradient occurs where temperature is lower at the upstream than the downstream. The temperature difference between those two temperature sensors can be translated to the flow's velocity. An illustration of its operation is shown in Fig. 2.4.

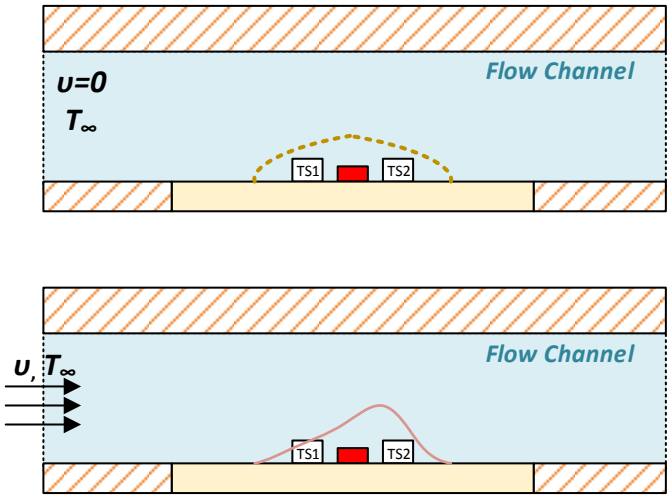

Fig. 2.4: A cross-sectional illustration of a calorimetric flow sensor. The heater is shown in red, whereas TS1 and TS2 are the temperature sensors symmetrically placed next to the heater, at the upstream and at the downstream, respectively. (Top): the dotted line represents an isothermal line, depicting the symmetrical thermal layer when there is no flow. (Bottom): the thermal layer is now shifted to the downstream due to flow of velocity υ.

Different models have been developed [28][41] to describe the correlation between this temperature difference, ΔT, and the fluid's velocity. Those theoretical studies showed that, it can be approximated as:

$$\frac{\Delta T}{T_H - T_\infty} = c_0 \frac{k_f W}{k_c\, a_c} \left(\frac{L^2}{v\, \rho_c\, a} \right)^{\frac{1}{3}} \sqrt{v} \tag{2.3}$$

ΔT: temperature difference between temperature sensors at inlet and outlet

T_H: heater's temperature, assuming it is homogeneous

T_∞: initial fluid's temperature, unaffected by heater

k_c, α_c, ρ_c: thermal conductivity, thermal diffusivity, and density of the substrate

k_f, α, v: thermal conductivity, thermal diffusivity, and kinematic viscosity of the fluid

W: size of transducer's area

L: distance between temperature sensors

c_0: an independent constant

υ: fluid's velocity

The first integrated calorimetric flow sensor has been published in 1987 [42], and since then, different variations have been developed to address issues such as power consumption [43], signal-to-noise ratio [44], and sensitivity [45]. Compared to the hot-wire topology, a calorimetric flow sensor can provide direction information, which is useful in certain applications [41][46].

A special category of calorimetric flow sensors is that of wind sensors. Those sensors have usually four temperature sensing elements, one placed every 90^o around the heater. Using the measurements from all the temperature sensors, one is capable to determine not only the wind's magnitude, but also its direction in two dimensions. The accuracy of the direction measurement is mainly related to the structural and thermal symmetries of the transducer, rather than on materials or techniques [45]. Fig. 2.5 shows a calorimetric flow sensor and a wind sensor. Notice that a typical calorimetric flow sensor has one heater (*R*h) and two temperature sensing elements (*R*u, *R*d), whereas the wind sensor has four heaters and four temperature sensing elements (thermopiles).

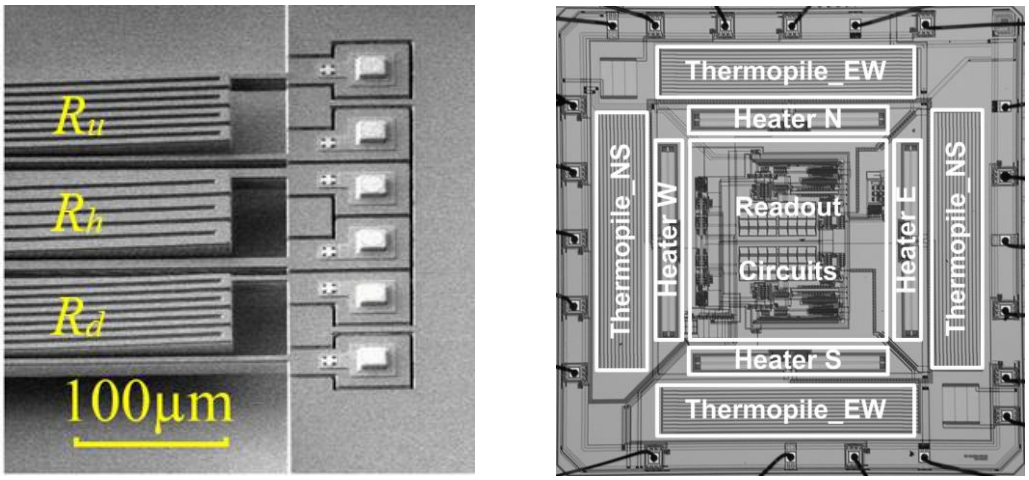

Fig. 2.5: (Left): a calorimetric flow sensor by Ahmed et al. [47], where *R*h is the heater, and *R*u and *R*d are the temperature sensing element at the upstream and at the downstream, respectively. (Right): a wind sensor by Wu et al. [48]. The four thermopiles serve as temperature sensing elements, whereas four heaters, instead of one, adjacent to the thermopiles are used.

Apart from orientation information, a calorimetric flow sensor offers improved transient response compared to hot-wire topology, and its output is less dependent on the fluid's properties. Nevertheless, models like the one presented in equation (2.3) are rarely accurate, making the initial design of the sensor difficult. In addition, a common issue of the calorimetric sensor is the manufacturing tolerance that could result in an offset at the output [49]; although, the two temperature sensors are designed to be in equal distance from the heater, practically that it is not the usually case. A proposed method to solve this problem came from Bruschi et al. [50] (Fig. 2.6) who suggested to use two heaters instead of one. The intended heater power is now directed to two heaters, however, it is not delivered equally but in the ratio that cancels out the offset created by the fabrication spread.

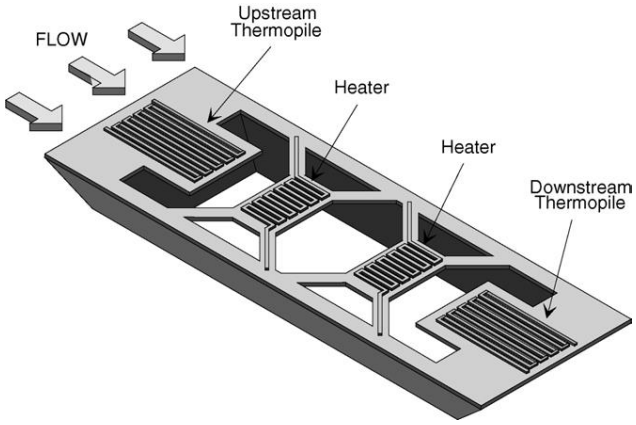

Fig. 2.6: The double heater calorimetric flow sensor [50]. Thermopiles serve as temperature sensing elements

2.2.4 Discussion

Section 2.2 presented the three main topologies of the thermal flow sensors: time-of-flight, hot-wire, and calorimetric, including some of their main attributes. It was evident that there are different aspects where one topology might be superior to the rest, while at the same time, it might be substantially inferior in some other aspects. An obvious example is the linearity at the output of the time-of-flight which the other topologies lack. However, there are cases where flow sensor designers attempted to fix the non-linearity to an extent by using lookup tables [51].

Calorimetric flow sensors, although they offer orientation information and higher sensitivity in low flows, their output range is substantially smaller than that of the hot-wire [52]. Therefore, flow sensors that make use of more than one topology have been proposed [53]. In fact, the proposed flow sensors are designed to operate as a calorimetric sensor for low flows, and as a hot-wire for high flows.

2.3 Operation Modes and Heater Control Circuits

It was evident in the above hot-wire section that in order to make flow measurements easier one has to comply with the King's law and equation (2.2) and maintain certain parameters constant throughout the measurements. This rule also applies in the calorimetric flow sensors, therefore, when a calorimetric flow sensor is presented, the parameter that is kept constant must be also stated. The choice of this parameter defines the mode of operation of the flow sensor. In literature, one can find them as *modes of operation*, or *operation modes*, or *operating modes*. In this thesis, all three terms will be used interchangeably, as in literature. The commonly found operating modes are:

- Constant Power (CP)
- Constant Temperature Difference (CTD)
- Constant Temperature (CT)
- Constant Voltage (CV)
- Constant Current (CC)
- Temperature Balance (TB)

In order to maintain the preferred parameter constant, a dedicated heater control circuit is needed to perform that task. Note that although the measuring parameter is different between a hot-wire flow sensor and a calorimetric flow sensor, the development and implementation of a heater control circuit is the same for both topologies. Therefore, examples of heater control circuits for the different modes can be drawn from either topology.

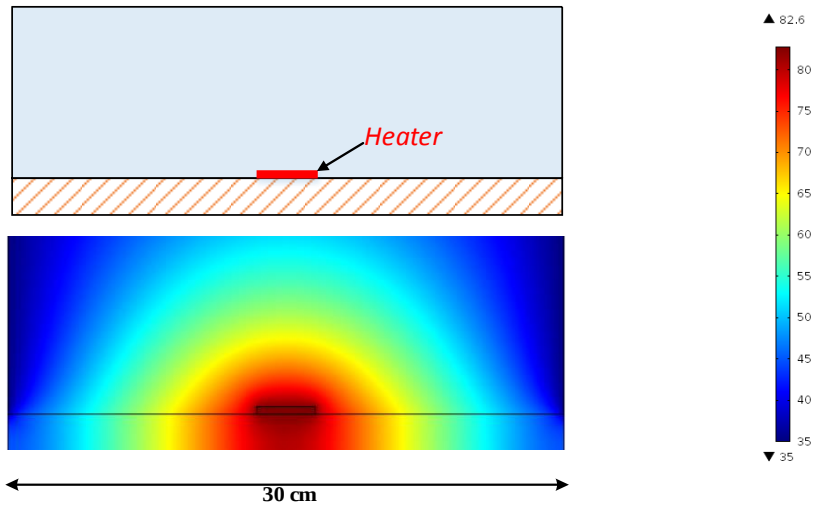

Fig. 2.7: (Top): A cross-sectional view of a thermal flow sensor model, with a heating element of dimensions 3.15cm by 0.5mm placed on top of a board. (Bottom): a heat map of the same topology at stable conditions: power, overtemperature, and flow's velocity are constant. In this case velocity is zero.

2.3.1 Constant Power (CP)

In constant power mode, it is the power delivered at the heater that needs to be maintained constant. According to (2.2), that means that the heater's temperature, T_H, is not controlled and it will take any value necessary to comply with (2.2). Fig. 2.8 provides simulation results of the topology presented in Fig. 2.7 for two different flow velocities U_1 and U_2, where $U_1<U_2$, at a constant fluid's temperature, T_∞, where, as expected, heater cools down as the flow increases. Most importantly, note the change in the temperature profile as shown at the bottom plot of Fig. 2.8. This plot depicts the temperature profile at the top surface of the board, from inlet to outlet. Assuming that temperature sensing elements are placed symmetrically next to the heater at a distance x_1, their temperature difference, ΔT, is a function of the fluid's velocity.

In the vast majority of cases, CP is implemented by supplying a constant current (CC) [54] or a constant voltage (CV) [55] to the heater. However, CV and CC can be approximated as CP only when the temperature coefficient resistance (TCR) of the heater is negligible. In case of CC or CV with non-zero TCR, the calorimetric flow sensor's output, ΔT, will not be able to be accurately reproduced every time.

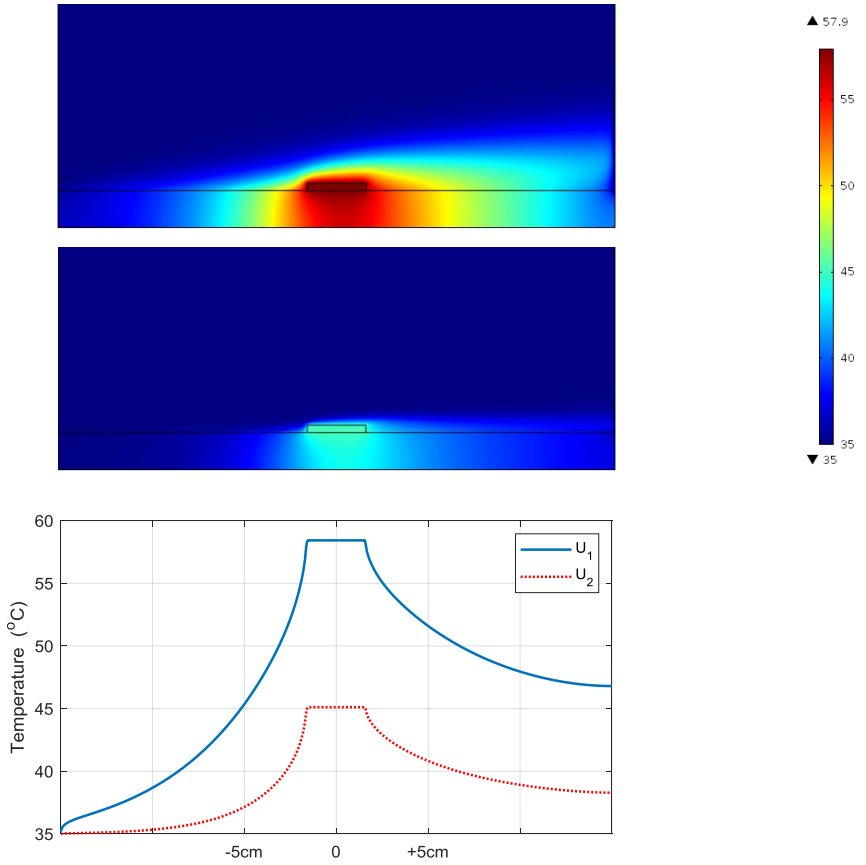

Fig. 2.8: A heat map for flow velocity U_1=0.25m/s (top), and U_2=3m/s (middle) under CP. At the bottom, the temperature profile at the board's top surface level from inlet to outlet. Note that $U_1<U_2$, and flow's direction is from left to right.

It is apparent that the aforementioned heater control circuit for the CP can be rather simple, assuming that a stable constant voltage or current can be easily generated. On the other hand, Kaltsas et al. [56] developed a PC software that continuously monitors the supplied current to regulate the supplied voltage accordingly, in order to maintain a stable power at the heater. In addition, data acquisition cards (DAQs) have been also used in the literature [57] to establish CP mode on a thermal flow sensor.

Although, the CP mode has the advantage of a possibly simple heater control circuit, it has an important disadvantage, as well, and that is its temporal behaviour. In fact, its response time to the flow changes is strongly dependent on the thermal capacity of the whole sensor. Hence, the larger the transducer area, the longer the time needed for the calorimetric flow sensor to reach its equilibrium. Therefore, small micromachined calorimetric flow sensors have a better temporal behaviour and, this is an important factor why great effort has been given in reducing the thermal capacity

of the flow sensor, such as using different materials.

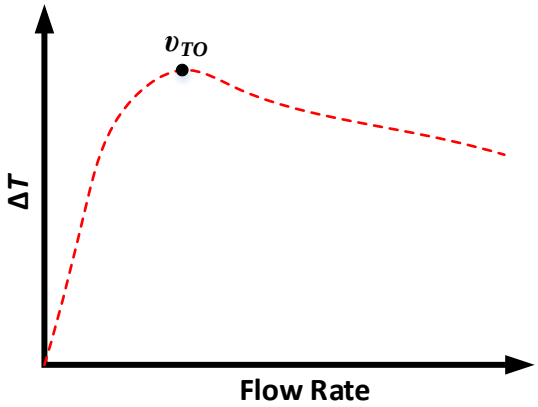

Fig. 2.9: An illustration of the output, Δ*T*, .of a calorimetric flow sensor for a range of different flow rates in CP mode.

The output of a calorimetric flow sensor is qualitatively drawn in Fig. 2.9. One can notice that the output almost linearly increases for low velocities. Then, it reaches a maximum, usually called turn-over velocity, v_{TO}, since the output starts decreasing and becoming non-monotonic. The sensitivity after the turn-over point is usually small, therefore, only the section from zero flow to v_{TO} is used for most of the cases. This output behaviour can be commonly found in the literature [57][58][59]. Models to estimate the v_{TO} have been developed, and an equation has been produced:

$$v_{TO} = \frac{2D}{W} \tag{2.4}$$

where *D* is the distance between the heater and the temperature sensor, and *W* is the size of sensor. However, this equation is rather simplistic to accurately calculate the turn-over point, due to the different physics involved. Similar to equation (2.3), (2.4) can be used as a guide regarding the variables that affect the parameter of interest, rather than an accurate estimator of the absolute value of the parameter. In fact, it has been shown in [58] that the experimental value might differ substantially from the calculated value of (2.4).

2.3.2 Constant Temperature Difference (CTD)

Compared to the CP mode where the power is constant, it is the overtemperature, $T_H - T_\infty$, that must remain constant throughout the measurements for the constant temperature difference (CTD) mode. As a result, the heater control circuit must be capable to draw any value of power required in order to keep the T_{OVER} stable. That might be a challenging task and many considerations must be taken into account regarding possible flow conditions. For example, the power demand might elevate significantly if the ambient temperature, T_∞, increases considerably. Another probably crucial case is when the fluid's velocity has risen greatly, hence, substantial amount of power might be required to maintain the heater's temperature constant.

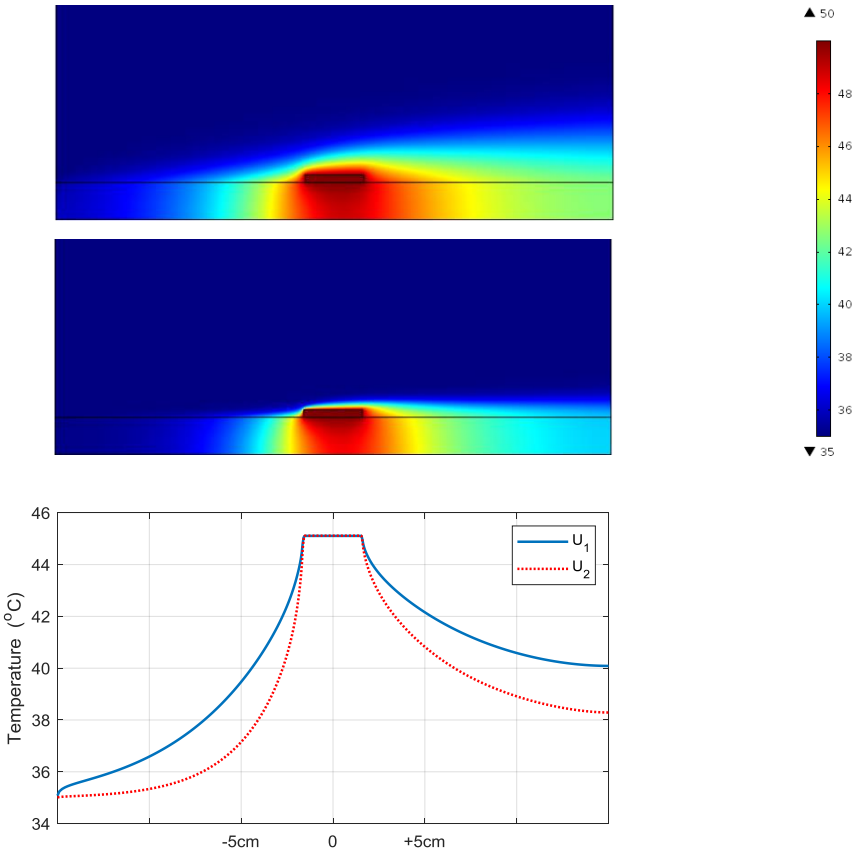

Fig. 2.10: A heat map for flow velocity U_1=0.25m/s (top), and U_2=3m/s (middle) under CTD. At the bottom, the temperature profile at the board's top surface level from inlet to outlet. Note that $U_1<U_2$, and flow's direction is from left to right.

Similarly to Fig. 2.8, Fig. 2.10 presents simulation results for the same velocities but for the CTD mode. Note that the temperatures at the inlet and at the heater are the same for both velocity scenarios. However, it can been noticed that the temperature

difference, ΔT, between the two symmetrical-to-the-heater points (i.e. at distance x_1) is a function of the fluid's velocity.

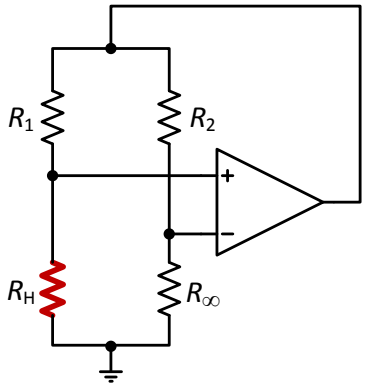

Fig. 2.11: A Wheatstone bridge operating as a CTD heater control circuit.

The most common heater control circuit used is a Wheatstone bridge and it has been firstly introduced in 1986 [60] to that purpose. Fig. 2.11 depicts the circuit where R_H is the heater, and R_∞ is the ambient temperature sensor. In this topology, the operational amplifier will create the necessary voltage at its output in order to the make its two input voltages equal. Assuming the latter is true, one can have:

$$\frac{R_H}{R_\infty} = \frac{R_1}{R_2} \tag{2.5}$$

Hence:

$$\frac{R_{H0}\left(1 + a_1(T_H - T_{REF})\right)}{R_{\infty 0}\left(1 + a_1(T_\infty - T_{REF})\right)} = \frac{R_{10}\left(1 + a_2(T_R - T_{REF})\right)}{R_{20}\left(1 + a_2(T_R - T_{REF})\right)} \tag{2.6}$$

where R_{H0}, $R_{\infty 0}$, R_{10}, R_{20}, are the nominal resistance values at temperature T_{REF}, and a_1, a_2, are the temperature coefficients of the resistors. Assuming T_{REF} is equal to zero for simplicity, one gets:

$$\frac{T_H}{T_\infty} \cong \frac{R_{\infty 0}\, R_{10}}{R_{H0}\, R_{20}} \tag{2.7}$$

Therefore, one can achieve a constant temperature ratio by choosing and trimming the right resistors' values of the Wheatstone bridge. Nevertheless, this is a ratio rather than a temperature difference which results in reduced accuracy at the output, especially

when the T_∞ varies substantially. Thus, modifications have been proposed [34], such as the one in Fig. 2.12. By setting the newly introduced resistor:

$$R_C = a_1 \, R_{\infty 0} \, T_{OVER} \tag{2.8}$$

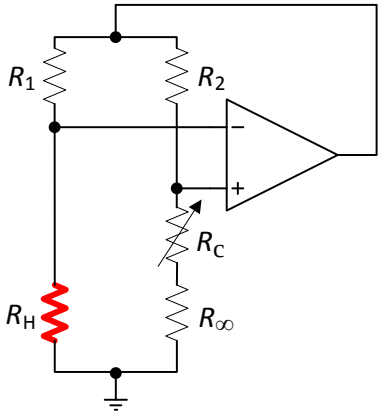

Fig. 2.12: Modified Wheatstone bridge to achieve accurate ΔT operating as a CTD heater control circuit.

and assuming:

$$\frac{R_\infty + R_C}{R_H} = \frac{R_2}{R_1} \tag{2.9}$$

it can be proved that $T_H = T_\infty + T_{OVER}$, hence, the flow sensor operates in CTD mode.

CTD mode outperforms CP mode in terms of transient performance, since once the transducer heats up, the heater must not change its temperature, while the temperature at the rest of the transducer area does not change vastly. Hence, the transient performance of a calorimetric flow sensor in CTD mode relies less on the thermal capacity of the transducer. Nevertheless, a closed loop heater control circuit is required to operate the mode, which is more elaborate compared to a heater control circuit of the CP. Another drawback that usually draws attention in the literature, is the position of the R_∞, especially in micromachined flow sensors. Ideally R_∞ must measure the fluid's temperature only, being totally unaffected by the heat energy produced in the heater. That is a challenging task when R_H and R_∞ are mounted on the same substrate, and it is usually tackled by using isolation techniques or choosing small overtemperatures [48].

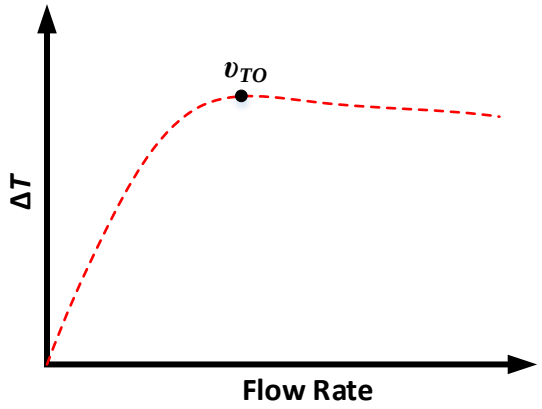

Fig. 2.13: An illustration of the output, Δ*T*, .of a calorimetric flow sensor for a range of different flow rates in CTD mode.

An illustration of the typical output of a calorimetric flow sensor in CTD is qualitatively drawn in Fig. 2.13 [38][61]. For low flows, the output, Δ*T*, almost linearly increases until it starts to saturate. After that flow rate point, minimal change at the output can be seen. Therefore, it is common that only the initial part until the saturation is used for flow measurements.

2.3.3 Constant Temperature (CT)

At the constant temperature (CT) mode, it is only the T_H that is kept constant. Although great inaccuracies might appear at the output, CT is one of the most common operating modes. The reason is the simplicity of the heater control circuit and its implementation. In fact it is a Wheatstone bridge like the ones presented before, but without any ambient temperature sensor to compensate for T_∞. Hence, by adjusting the other three resistors of the bridge accordingly, one can achieve the T_H required without worrying about how and where to measure T_∞.

Also, it has some other practical benefits such as a power budget that is easier to estimate, and a predefined heater's temperature. The latter is rather useful when strict limits of absolute maximum temperature are dictated either by the materials and components used or by health and safety rules. It can be also implied that CT mode finds use where the fluid's velocity is generally stable and high accuracy is not important.

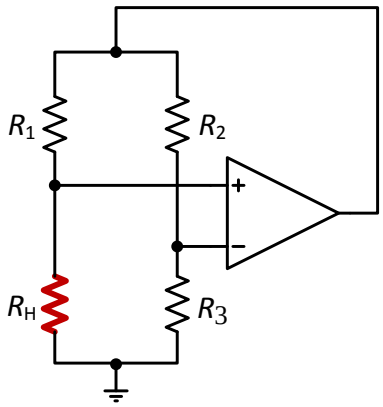

Fig. 2.14: A Wheatstone bridge operating as a CT heater control circuit.

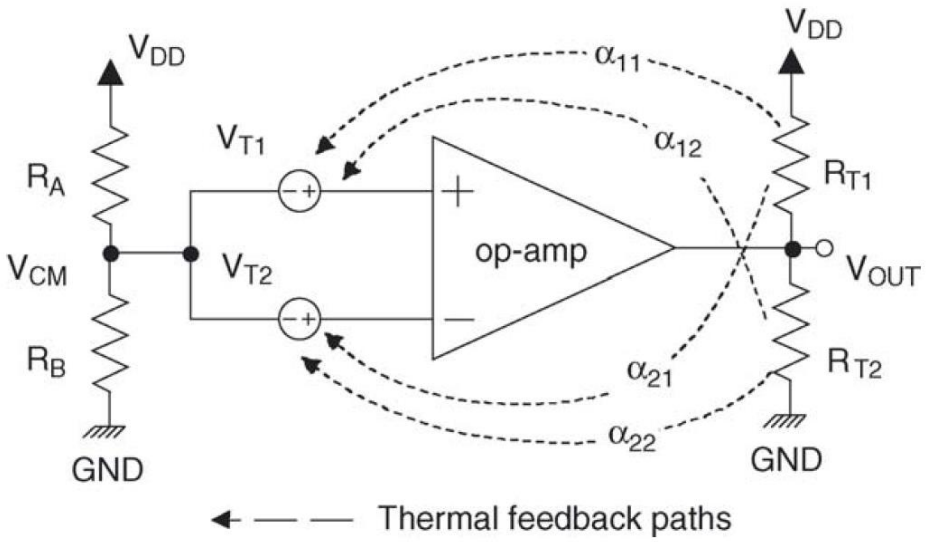

Fig. 2.15: Schematic view of a TB circuit for calorimetric flow sensor [50]. V_{T1}, V_{T2} are the voltage outputs of the temperature. $R_{T1,}$ R_{T2} are the heaters, and a_{ij} are the flow dependent coefficients.

2.3.4 Temperature Balance (TB)

A temperature balance (TB) is a mode that is prevalently utilised in wind sensors, rather than flow sensors. The reason is that it requires one independent heater for every temperature sensing element, similar to Fig. 2.6 presented before. However, the power ratio delivered to the heater is that in order to cancel out any temperature difference measured between the temperature sensing elements. Fig. 2.15 present a suggested

heater control circuit for the TB mode by Bruschi et al. [50], where V_{T1} and V_{T2} are the voltage outputs of the temperature sensors as a linear function of the temperatures measured. R_{T1} and R_{T2} are the heaters, and a_{ij} is the flow dependent coefficient of the j-th heater on the i-th temperature sensor. When there is flow over the sensor, the downstream temperature sensor will measure a higher temperature than the one at the upstream, creating a voltage at the output of the opamp that will unbalance the power delivered at the two heater. Eventually, the output will settle at the value which brings the V_{T1} and V_{T2} at the same value. In fact, the same circuit is a heater control circuit and a flow measurement circuit, as well, since the opamp's output V_{OUT} can be used to quantify the flow.

A similar topology can be seen quite often in wind sensors, and a simple schematic of it is presented in Fig. 2.16. "Heater N" and "Heater S" are the two heaters, while their temperature difference is measured using a single thermopile. The operation of a thermopile will be presented in a later section of this chapter. The temperature difference measured by the thermopile is amplified and fed into a flip-flop. The flip-flop will create a bitstream at its output that will drive one of the heaters, while its complementary output will drive the second one, creating a duty-cycle proportional to the flow's velocity above the wind sensor.

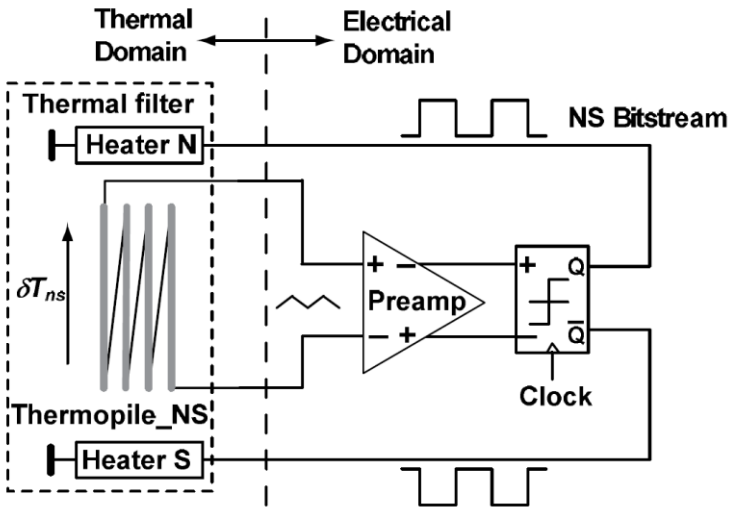

Fig. 2.16: Block diagram of a heater control circuit of a wind sensor [48] .

2.3.5 Discussion

Section 2.3 presented the main modes of operation of the calorimetric flow sensors, including their common heater control circuits. It is evident that most of these circuits are rather simple, and in some cases simplifications and assumptions are required. One example is the CV or the CC mode that are considered as CP mode with a heating element of negligible temperature coefficient. Another example is the calculation of the output, ΔT, as calculated in equation (2.7). It is certain that the vast majority of the published work has been focussed on improving the sensitivity and/or the power consumption of the sensor, whereas less attention has been given to the heater control circuit. The latter is evident since only a small part of the published work mentions an elaborate heater control circuit, while the number of heater control circuits integrated on the same substrate with the transducer, is even smaller.

Topologies that have been tested in more than one operating mode also exist [56][62][63]. Yet, a smart wind sensor that justifies the choice of a different mode based on flow has been suggested only once by Wang et al. [64]. The authors suggested the operation in CV in low flows and in TB in high flows, for improved accuracy. To the author's best knowledge, that is the only smart multi-modal system in the literature.

To certain extent, the non-use of multi-modal systems is encouraged by the fundamentally different specifications among the operating modes. Specifically, heaters of negligible temperature coefficient are preferred for CP systems to simplify the design of the heater control circuit. On the other hand, heaters of great temperature coefficient are required for CT or CTD systems, to improve the accuracy of heater's temperature.

As a heating element different materials have been used, such as Nickel, Polysilicon, Germanium, Platinum, and Tungsten, with the last two preferred for medical applications due to their biocompatibility, while Tungsten is also mechanically strong.

2.4 TRANSDUCTION METHODS AND FLOW MEASUREMENT CIRCUITS

Calorimetric flow sensors can be also categorised into three main topologies based on the method of transduction, and subsequently, on their flow measurement circuit. The flow measurement circuit, or else the output circuit, is the topology that provides the temperature difference, ΔT, between the upstream and the downstream temperature sensing elements, and it strongly relies on the temperature sensing elements used and their principle that transforms temperature to a property that can be processed by an electronic circuit. These categories are:

- Thermoresistive
- Thermoelectric
- Thermoelectronic

Specifically, the first category makes use of temperature sensitive resistors, the thermoelectric group uses thermopiles, whereas the third category utilises diodes, or transistors, as temperature sensing elements.

2.4.1 Thermoresistive

Commonly used temperature sensitive resistive materials are the Germanium [65], Platinum, Nickel [66], and Polysilicon [34]. Apart from the Germanium, the resistance of the rest can be assumed as linearly dependent on the temperature as:

$$R_M = R_0\big(1 + a(T_M - T_{REF})\big) \tag{2.10}$$

where R_M is the resistance measured in temperature T_M, and R_0 the nominal resistance in reference temperature T_{REF}. a is the temperature coefficient of the material. In contrast, Germanium exhibits an exponential relationship to the temperature, in the form of:

$$R_M = R_0\, exp\big(a(T_M - T_{REF})\big) \tag{2.11}$$

The most common and simple topology to measure the resistance changes is to connect the resistor of interest in series with a known value resistor and measure its

voltage drop. In order to get the difference in the resistances the temperature sensing elements are connected in the form of a Wheatstone bridge as Fig. 2.17 depicts. In Fig. 2.17a, one can get:

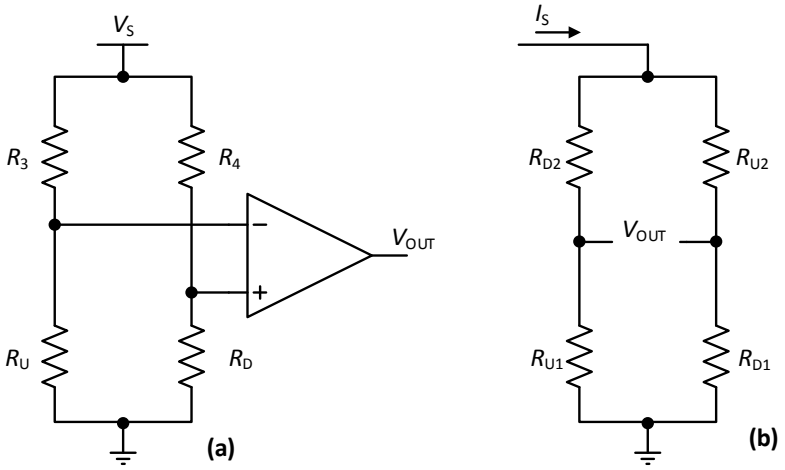

Fig. 2.17: Wheatstone bridges used as flow measurement circuits of thermoresistive calorimetric flow sensors. R_U, R_{U1}, R_{U2} and, R_D, R_{D1}, R_{D2} are the temperature sensors at the upstream and at the downstream, respectively. (a) A bridge operating with constant voltage V_S. (b) A bridge operating with constant current, I_S, while using four temperature sensors.

$$V_{OUT} = V_S \frac{R_D\, R_3 - R_U\, R_4}{(R_D + R_4)(R_U + R_3)} \tag{2.12}$$

Assuming that $R_3 = R_4 = R_0$, and $R_D = R_0\,(1+a\,T_D)$ and $R_U = R_0\,(1+a\,T_U)$, the (2.12) can be re-written as:

$$V_{OUT} = V_S \frac{a(T_D - T_U)}{4\left(1 + \frac{a}{2}T_D\right)\left(1 + \frac{a}{2}T_U\right)} \tag{2.13}$$

Therefore, it can be assumed [34]:

$$V_{OUT} \approx \frac{1}{4}\, a\, V_S\, \Delta T \tag{2.14}$$

The output voltage can be also acquired using a constant supply current, I_S, instead of voltage. In literature [65][67], one can find topologies where two pairs of temperature sensing elements are used, R_{U1}-R_{D1}, and R_{U2}-R_{D2}, all of them connected in the same bridge, as Fig. 2.17b depicts. The output V_{OUT} in this case would be:

$$V_{OUT} = I_S \frac{R_{U1}\,R_{U2} - R_{D1}\,R_{D2}}{R_{U1} + R_{U2} + R_{D1} + R_{D2}} \tag{2.15}$$

As equations (2.12) and (2.15) show, the output is a complex function of ΔT, rather than linear. That does affect the output's waveform but not the reproducibility of the results.

Thermoresistive flow sensors offer a large temperature range of measurements, good accuracy and, Pt resistors in particular, great linearity. Thermistors offer low cost, high sensitivity, and small size. Nevertheless, topologies such as those presented in Fig. 2.17 assume a perfect match of the resistors' nominal values and of their temperature coefficients which is not easy to achieve. In addition, it is likely that self-heating of the resistors might occur, which will lead to erroneous measurements. Finally, a special process is required in order to integrate thermistors on a silicon chip, hence, time and cost of manufacture rises.

2.4.2 Thermoelectric

A thermopile consists of a number of thermocouples connected in series. The thermocouple consists of a pair of different wires merged at one point. Considering temperature T_{REF} at one end of the wires (Fig. 2.18), any different temperature (T_{S}) sensed at the point of the junction produces an electric potential proportional to this change, due to the Seebeck effect. Seebeck effect is the effect when heat is directly converted into electricity at the junction of different types of wire. The output of a thermocouple is:

$$V_{AB} = S_{AB}\,(T_S - T_{REF}) \tag{2.16}$$

where S_{AB} is the difference in Seebeck coefficient between materials *A* and *B*. Table 2.1 presents the Seebeck coefficient of commonly used materials [19]. The most common combinations found in the literature are those of n-poly/Al [68], p-poly/Al [69], and p-poly/n-poly [54]. The output of a thermopile is the sum of the thermocouples' output.

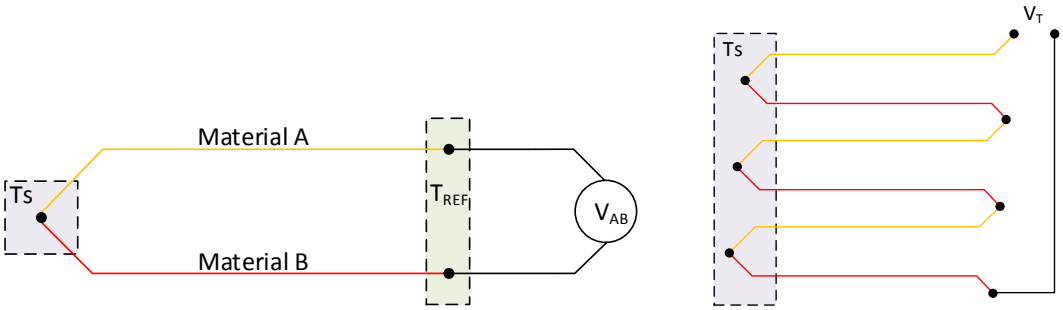

Fig. 2.18: A drawing of a thermocouple (left), and of a thermopile (right).

TABLE 2.1: Seebeck coefficient of materials typically used for thermocouples

Material	**Seebeck coefficient (μV/K)**
Aluminum	3.5
Gold	6.25
Copper	6.15
p-type Silicon	300~1000
n-type Silicon	-500~-200

The design of a thermopile is straightforward, while it is inexpensive and self-powered. Moreover, it can be fabricated in standard CMOS, facilitating the bulk, inexpensive production. However, a thermopile is unable to measure the absolute temperature, but the localised temperature gradient, hence, if the T_{REF} area is not completely isolated by the heater, the output of a thermopile is likely to be considerably small. In addition, it is highly likely that the T_{REF} of the thermopile at the upstream is not equal to the T_{REF} of the thermopile at the downstream, compromising the accuracy of the measurement. Also, the implementation of a thermopile demands greater area compared to other temperature sensing implementations.

Since the electrical quantity representing the temperature is already in voltage, the temperature difference between upstream and downstream, ΔT, can be easily acquired using an instrumentation amplifier [54]. Assuming that the T_{REF} of both of thermopiles is the same, and n_{TH} is the number of thermocouples per thermopile, the output of the thermal flow sensor will be:

$$V_{OUT} = n_{TH}\, S_{AB}\, \Delta T \tag{2.17}$$

A typical thermoelectric flow sensor is shown in Fig. 2.19.

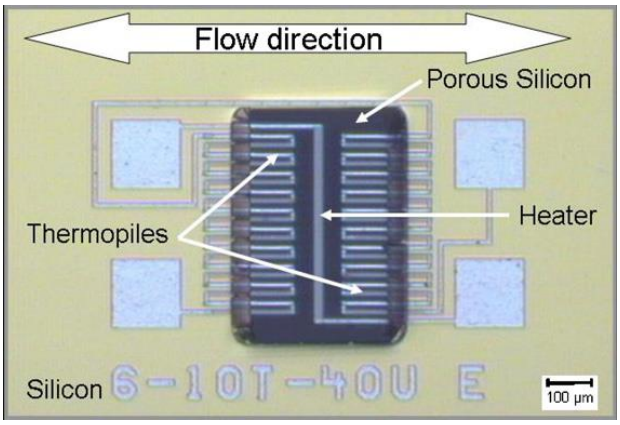

Fig. 2.19: A top view of a thermoelectric calorimetric flow sensor [56]. Two thermopiles are symmetrically placed next to a polysilicon heater. Note that the heater and the thermopiles' hot junction are placed on top of porous silicon layer in order to thermally isolate the cold junctions.

2.4.3 Thermoelectronic

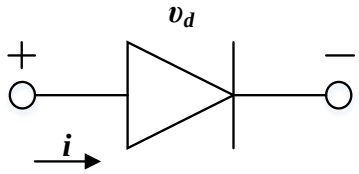

Fig. 2.20: Basic schematic of a diode, including its basic parameters, i and υ_d.

The thermoelectronic transduction method is usually realised by diodes operating as temperature sensing elements [70]. It is well-known that the i-υ relationship of a diode is [71]:

$$i = I_C \left(exp\left(\frac{v_d}{n_C\, V_T}\right) - 1 \right) \tag{2.18}$$

i: current through diode

I_C: saturation current

υ_d: voltage drop across the diode

n_C: constant depending on materials and structure of the diode. Usually n_C =1 for standard integrated circuits

$$V_T = \frac{k_B\, T}{q} \tag{2.19}$$

V_T is called thermal voltage where k_B is the Boltzmann constant, q the electron charge, and T the temperature in K. Assuming $i >> I_C$, (2.18) can be re-written as:

$$i \cong I_C\, exp\left(\frac{v_d}{n_C\, V_T}\right) \tag{2.20}$$

which can be also expressed as:

$$v_d = \left[\frac{n_C\, k_B}{q}\, ln\left(\frac{i}{I_C}\right)\right] T \tag{2.21}$$

Considering the diode is supplied with a constant current, i, (2.21) clearly shows that the voltage drop across the diode is a linear function of the temperature.

Diodes used as temperature sensing elements provide many benefits, such as easy integration in standard CMOS, high sensitivity, linearity, small area, while the electrical quantity representing the temperature is already in voltage, simplifying the readout topology. However, their accuracy at the important range of 300K is compromised, affecting their reliability [72].

2.4.4 Discussion

It is evident that all the transduction methods presented above have their own advantages and disadvantages. The choice of method is usually based on the fabrication methods and materials available.

Similar to heater control circuits, it was also evident that the majority of the calorimetric flow sensors found in the literature do not present an elaborate measurement circuit, let alone an integrated flow measurement circuit [47].

2.5 TOWARDS LOW-POWER, HIGHLY SENSITIVE CALORIMETRIC FLOW SENSORS

2.5.1 Methodology

As mentioned before, thermal flow sensors can be power hungry due to the use of heating elements; hence, great effort has been given to limit the power consumption without compromising the robustness of the flow sensor. Power dissipation at the heater varies substantially in the literature, and it significantly depends on the materials, dimensions, and the intended flow rate measurement range; thus, power consumption from hundreds of μW to hundreds of mW have been reported. Assuming the flow rate range is not to be compromised, the obvious method to reduce power consumption is the miniaturisation. Considering that all the power supplied to the heater, *P*, is transformed as a whole to thermal energy, one can get:

$$P = \dot{E_{st}} + \dot{E_{out}} \tag{2.22}$$

where $\dot{E_{st}}$ is the rate that thermal energy is stored at the heater, whereas $\dot{E_{out}}$ is the rate that thermal energy leaves the heater. Assuming $\dot{E_{cond}}$ the rate of the thermal energy lost due to conduction, and $\dot{E_{conv}}$ due to convection:

$$\dot{E_{out}} = \dot{E_{cond}} + \dot{E_{conv}} \Rightarrow$$

$$\dot{E_{out}} = k_c\, A_{sub}(T_H - T_\infty) + h\, A_F\, (T_H - T_\infty) \tag{2.23}$$

While:

$$\dot{E_{st}} = m\, C\, (T_H - T_\infty) \tag{2.24}$$

Equation (2.22) can be re-written as:

$$P = (m\, C + k_c\, A_{sub} + h\, A_F)\, (T_H - T_\infty) \Rightarrow$$

$$\frac{P}{T_{OVER}} = m\, C + k_c\, A_{sub} + h\, A_F \tag{2.25}$$

m: heater's mass

C: heater's thermal capacity

k_C: substrate's thermal conductivity

A_{sub}: heater's surface exposed to the substrate

h: heat transfer coefficient

A_F: heater's surface exposed to the flow

Equation (2.25) clearly shows that one can get the same overtemperature with less power (or achieve higher overtemperature with same power) by decreasing the size of the heating element and/or by shrinking the heat losses through the substrate.

In addition, miniaturisation not only decreases the power dissipation but also improves the transient response of the thermal flow sensor. Specifically, the thermal time constant of a material exposed to a flow is [73]:

$$\tau = \frac{\rho\, C\, Vol}{h\, A_F} \tag{2.26}$$

ρ: heater's density

C: heater's thermal capacity

Vol: heater's volume size

A_F: heater's surface exposed to the flow

h: heat transfer coefficient

Although equation (2.26) is generic, one can still identify the correlation and the effect of the heater's size and material on heater's thermal speed.

Equations (2.25) and (2.26) confirm the benefits of a miniaturised flow sensor, therefore, a large number of this kind of sensors have been reported. However, the prevalent substrate material is that of the silicon which exhibits a high thermal conductivity, *k*. High thermal conductivities are to be avoided since they increase the thermal losses through the substrate. Therefore, different methods have been used to further improve the power consumption of the heater.

One of those methods is the use of other than silicon material as a substrate. Porous materials have been used [74] to thermally isolate the heating element, reporting a fast response time. In addition, Glass-in-Silicon has been also used [75] as a substrate recording better performance in terms of power consumption. Other materials such as ceramic [13], has been also utilised. Although, the use of materials

other than silicon improved the performance of the sensor, one must also consider that using other materials than silicon hinders the smooth and easy integration of the transducer with the rest of the electronic circuitry, which eventually results in increased fabrication time and cost.

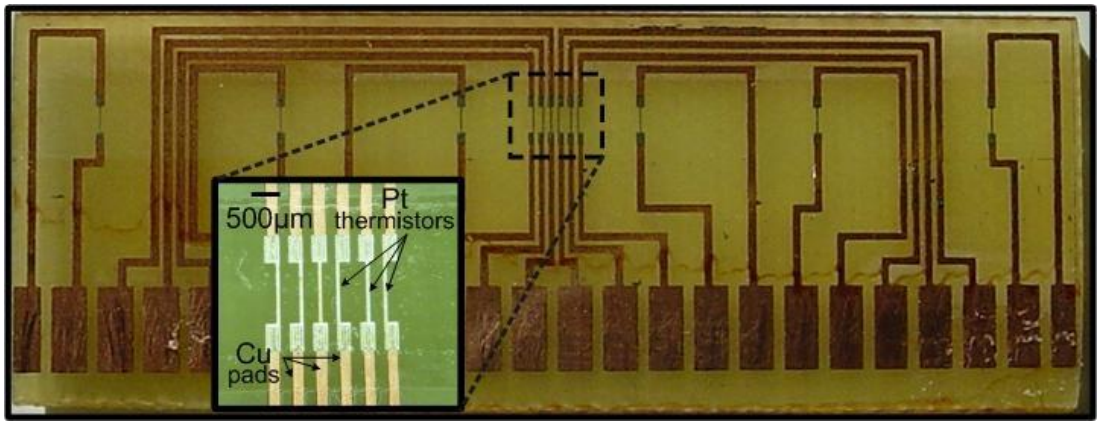

Fig. 2.21: A photograph of a thermoresistive flow sensor realised on PCB by Petropoulos et al. [62].

Printed circuit boards (PCBs) have also been used as a substrate material [76][77], as Fig. 2.21 depicts. Although the size of the flow sensor might be significantly greater than that of a Si-substrate sensor, the thermal conductivity of the FR4 is approximately 500 times smaller than that of the Si, greatly reducing the thermal losses and, subsequently, the power dissipation of the heater.

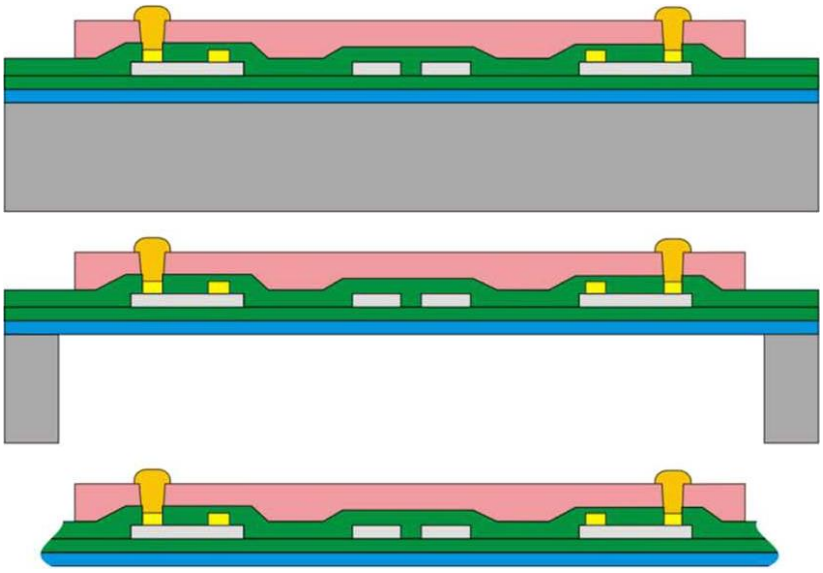

Fig. 2.22: A schematic of thinning process by [78]. Firstly the biggest part of the substrate is etched, and then, the sensor is separated from the silicon wafer

Another method used for reducing heat losses is the thinning of the substrate [32]. Using etching techniques, the height of the substrate can be diminished. Fig. 2.22 shows the steps of a thinning process, where silicon substrate is completely removed. However, the sensor might end up to be fragile and prone to fracture in case of mechanical shock. The same problem occurs in another method, where the heating element suspends [40][79], being completely immersed in the flow.

Etching techniques have also been implemented not only on the back side, but also at the sensing side among the transducer's elements [63][66]. This way, the heater's surface exposed to the air increases, whereas the surface attached to the substrate, A_{sub}, diminishes. It has been reported that such a construction improves the transient behaviour of the sensor substantially, while it affects to a lesser extent its mechanical stability.

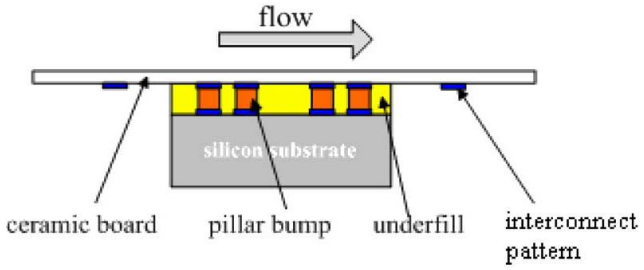

Fig. 2.23: A cross-sectional illustration of a packaged sensor [80]. The chip is bonded to a ceramic board, which protects the transducer from contamination.

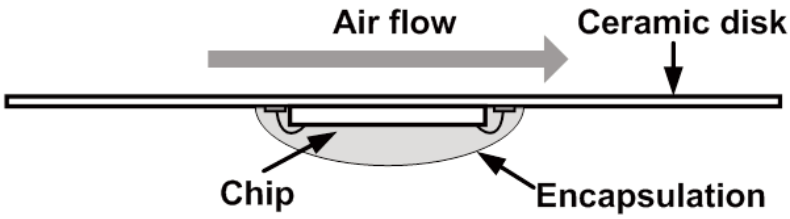

Fig. 2.24: A cross-sectional illustration of a back surface sensing [81]. The back side of the chip used of the flow measurement while the front side with the wire-bonds are encapsulated.

Nevertheless, there is another cause of reduced sensitivity and increased power consumption that requires new methods in order to suppress it. Specifically, packaging and protection of the transducer's area have a negative effect on the sensor's performance [80]. In practical applications and without packaging, the transducer is

exposed to contaminants affecting its performance over time. In addition, implementations where the transducer is a suspended membrane or where the different elements are suspended, the transducer becomes fragile and it is prone to deformation due to thermal stress [82]. Even if the transducer is not suspended, the use of wire-bonding to connect the transducer to the rest of the circuitry does not permit the measurement of high velocities since they can be easily damaged. Therefore and in practical applications, a ceramic disc is glued on the sensor to create a flat, clean surface that protects the chip from any pollutants (Fig. 2.23) and increases its mechanical rigidity.

Fig. 2.24 shows a different but common technique used to address the same issue; it is the back surface sensing where the transducer's side including the wire-bonds are protected by encapsulation, while the actual flow measurement is realised at the back side of the chip. This method offers great protection to the chip, hence, better reliability, however, the increase in distance between the sensor's elements (heater and temperature sensors) and the flow has a significant effect on the power consumption and sensitivity. Note that the power consumption reported for back surface sensing is usually more than 25mW.

2.5.2 Discussion

It is evident that although etching techniques improve the robustness of the flow sensor in power and sensitivity, their cost forbids the productions of an inexpensive but robust flow sensor. In addition, practical issues dictate the protection of the transducer, especially when they are implemented in harsh environments, compromising low-power operation; thus, the development of a low-power but practical and reliable flow sensor is challenging. Therefore, more ways must be devised to improve sensor's performance in terms of power dissipation and sensitivity without increasing its cost. One methodology developed [83][62] to improve sensitivity or measurement range for the same setup was to find the optimal distance between the heater and the temperature sensing elements. Nevertheless, more work needs to be conducting since they both refer to the same mode of operation.

Another effect of the power is on the flow measurement range. As explained

before, it is usually the range from zero until the turn-over velocity, or where saturation starts to occur, that is considered useful and it is directly related to power at the heater. Hence, new methods that reduce the power without compromising the measurement range must be considered.

3

EFFECT OF TEMPERATURE SENSORS' POSITION ON FLOW SENSOR'S MEASUREMENTS

A flow sensor for respiratory monitoring applications needs to be as small as possible in order to minimise interference to flow. Any impeding to the flow may lead to turbulence, which, consequently, results in an increase in the flow resistance. It is important that any considerable increase in flow resistance, especially in cases of continuous respiration monitoring for patients with breathing difficulties, should be avoided. In addition, sensor's portability target dictates not only small size but also high sensitivity with minimum power consumption, without compromising the measurement range.

This chapter investigates the impact of the temperature sensors' location relatively to the heater on a calorimetric flow sensor's performance, and it is divided into two parts. The first, consists a study for the optimisation of the distance, *D*, between heater and temperature sensor, with the assistance of simulation software and Finite Element Analysis (FEA). Minimising *D* is important since it reduces the size of the transducer area. However, this should not happen at the expense of output sensitivity. The second part is an experimental investigation of the effect of asymmetrically located temperature sensors on flow sensor's sensitivity, and measurement range.

3.1 CALORIMETRIC FLOW SENSOR OPTIMISATION USING FEA

Among the most common topologies of thermal flow sensors in miniature medical devices or microsystems is the calorimetric type, as it can be implemented in an easy and inexpensive way while it offers good accuracy as well as flow orientation information. Their operation is based on the temperature gradient near the central heater that arises when flow occurs. This gradient can be measured by two equally spaced temperature sensors at the upstream and downstream of the flow, respectively [24].

As previously described, a flow sensor's heater can possibly work in one of the following three operating modes: Constant Power (CP) where P is constant; Constant Temperature (CT) where T_H is constant (and P is varied); and Constant Temperature Difference (CTD) where $T_H - T_\infty$ is constant (and P is varied). The majority of previous and existing works on flow sensors limit themselves to one [80] or several of the operating modes, such as constant power and constant temperature. However, they gave no clear justification why a particular mode was chosen and provided no evidence for the chosen distance between the heater and the temperature sensors [56].

For miniature calorimetric flow sensors, the power consumption and the physical size of a flow sensor system are the two of the most important parameters that need to be optimised. The power consumption of a flow sensor system consists of the heater power and the power of the electronics. The latter is usually much smaller than the former, and the optimization of the power for electronics depends on the circuit design techniques and manufacturing. The size of the electronics (incl. temperature sensors, ADCs, etc.) can be made very small, should commercial purpose-made integrated circuits are used. Therefore, the size of a flow sensor is defined proportional to the distance between the heater and the temperature sensor.

In this chapter, I compare the calorimetric flow sensor's performance under the three possible operating modes and provide guidelines on how to optimise sensor design towards a novel figure of merit which is defined as the product of heater power and sensor size.

3.1.1 Simulation Setup

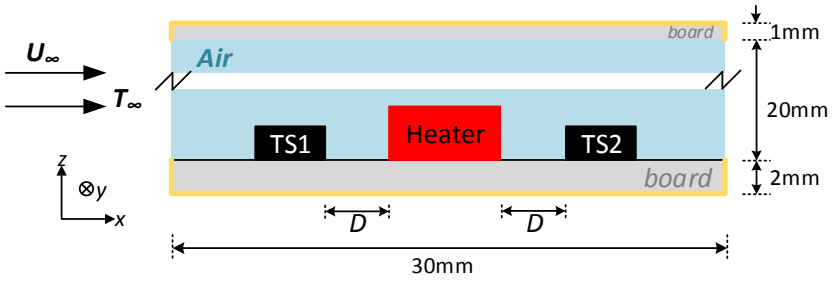

Fig. 3.1: Illustration of the simulation setup. The temperature sensors TS1 and TS2 are placed symmetrically to the heater at distance *D*. The yellow line highlights the thermal insulation points of the model.

A basic drawing of the simulation model is shown in Fig. 3.1. A two-dimensional design of a flow sensor has been developed using the COMSOL Multiphysics® software, consisting of a heater with dimensions 3.15 mm (width) × 0.4 mm (height) placed on a printed circuit board (PCB), while a tunnel of 20 mm diameter is created over it. U_∞ is the far-field, uniform velocity of the incoming air. Although, temperature sensors TS1 and TS2 are depicted in the figure, the actual simulation model does not include any geometries for the temperature sensors. Instead, the temperature at the top surface of the board is considered. Assuming that there is not any heat or velocity gradient in *y* direction, a 2D model should be adequate to optimise the flow sensor.

In addition, the flow within the tunnel is defined as laminar, starting developing from the edge of the board. The choice of a laminar flow is rather important since it defines the set of equations that describe the flow profile and the temperature distribution in the fluid. Since the contribution of radiation towards heat transfer is practically insignificant when being compared to that of the forced convection, only the latter is considered in the simulation which also makes the simulation run quicker. On the other hand, the main heat transfer phenomenon within the boards and heater, is conduction, described by the diffusion equation:

$$\nabla^2 T + \frac{q}{k} = \frac{1}{a}\frac{dT}{dt} \tag{3.1}$$

where q is the volumetric heat rate and α the thermal diffusivity of the material of interest. However, since it is a steady-state problem while heat is generated only in the

heater, Eq. (3.1) can be simplified to the Laplace's equation:

$$\nabla^2 T = 0 \tag{3.2}$$

for the board, and to:

$$\nabla^2 T + q/k = 0 \tag{3.3}$$

for the heater. The rest of the boundary conditions are the insulation at the external walls of the boards highlighted in Fig. 3.1, and the convection surface condition between the inner boards' walls and the fluid. The heat loss from the heater is either through the flow or to the substrate. The latter is dictated by the thermal conductivities of the board and heater, and it can be minimised by choosing a board material with smaller *k*. The optimisation of the heat loss through the substrate is beyond the scope of this work as it would be specific to different board materials.

The different properties of various parts in the setup are listed in Table 3.1. Furthermore, the relative humidity of the fluid is defined as 90% while the simulations are performed for two different T_∞, 20 ^{o}C and 35 ^{o}C, in an effort to reproduce the environment of a medical flow sensor during respiration, such as that at the distal end of an intratracheal tube.

TABLE 3.1: Important parameters of the materials used

			Heater (Ni)	**Board (FR4)**	**Air (35^{o}C)**
Thermal Conductivity	k	*(W/m·K)*	11.3	0.3	0.027
Density	ρ	*(kg/m^3)*	8400	1900	1.13
Specific Heat Capacity	C_P	*(J/kg·K)*	450	1369	1007
Dynamic Viscosity	μ	*(kg/m·s)*			1.9×10^{-5}

The output of the flow sensor is the temperature difference, $\Delta T(D,U_\infty)$, between the two temperature sensors (see TS1 and TS2 in Fig. 3.1) which are placed symmetrically on either side of the heater. For a defined velocity, a high temperature difference is important because i) it indicates the sensor is sensitive to the flow, hence able to measure small changes of flow and ii) it is then relatively easy to implement a temperature readout circuit. However, the high temperature difference may come at the expense of an elevated power consumption and increased sensor size. The

simulated velocities are 0.25, 1.25 and 3 m/s, which correspond to 4.7, 23.6 and 56.5 slm for the aforementioned setup. A respiratory rate of 12 to 18 breaths per minute is considered normal for healthy adults at rest [84]. Considering a tidal volume of 500 mL, the flow rate of a healthy individual at rest can be approximated as 12 to 18 slm. Hence, the simulated velocities cover a variety of breathing conditions of different flow rates.

The initial conditions for all three modes are set as 5 W for 3 m/s inlet velocity at 35 ^{o}C. As a result, the CP operates at 5 W, the CT at 45.1 ^{o}C, and the CTD at 10.1 ^{o}C overtemperature.

3.1.2 Simulation Results

3.1.2.1 Different Operating Modes

Fig. 3.2 shows the simulation results for different operating modes. The first column shows the heater power vs. velocity (in bar graphs) and heater temperature vs. velocity (in line curves) for the CP, CT and CTD modes while the second column shows the temperature difference between the two temperature sensors when the distance between the temperature sensor and the heater is swept from 0 to 13.4 mm. In the CP mode the T_H varies depending on the T_∞ and velocity (Fig. 3.2a). It is also shown that for a defined distance D from the heater, the output is independent of T_∞ (Fig. 3.2b). Hence, the CP mode does not need an extra temperature sensor which is distant to the heater for measuring the original gas temperature. However, excessive temperatures might be reached at the heater when there is low or no flow through the sensor, and consequently, they may cause discomfort to the patient if the flow sensor is placed close to human tissue.

In the simulations for the CT mode, a wide range of power (2.15 ~ 12.4 W) is needed to keep the temperature constant (Fig. 3.2c). Hence electronics with high power rating might be needed, increasing the dynamic range and physical size of the feedback circuits. In addition, Fig. 3.2d shows that for different T_∞, the output ΔT for a given distance D, is not constant. As a result, an inlet temperature sensor is necessary for the correct velocity prediction, further increasing the complexity of the feedback circuitry. This is why most of the existing sensors [83] that operate in the CT mode

have stable inlet gas temperature for eliminating the need for inlet temperature compensation. For a given inlet air temperature, a higher heater temperature results in better sensitivity to the flow at the expense of higher power consumption.

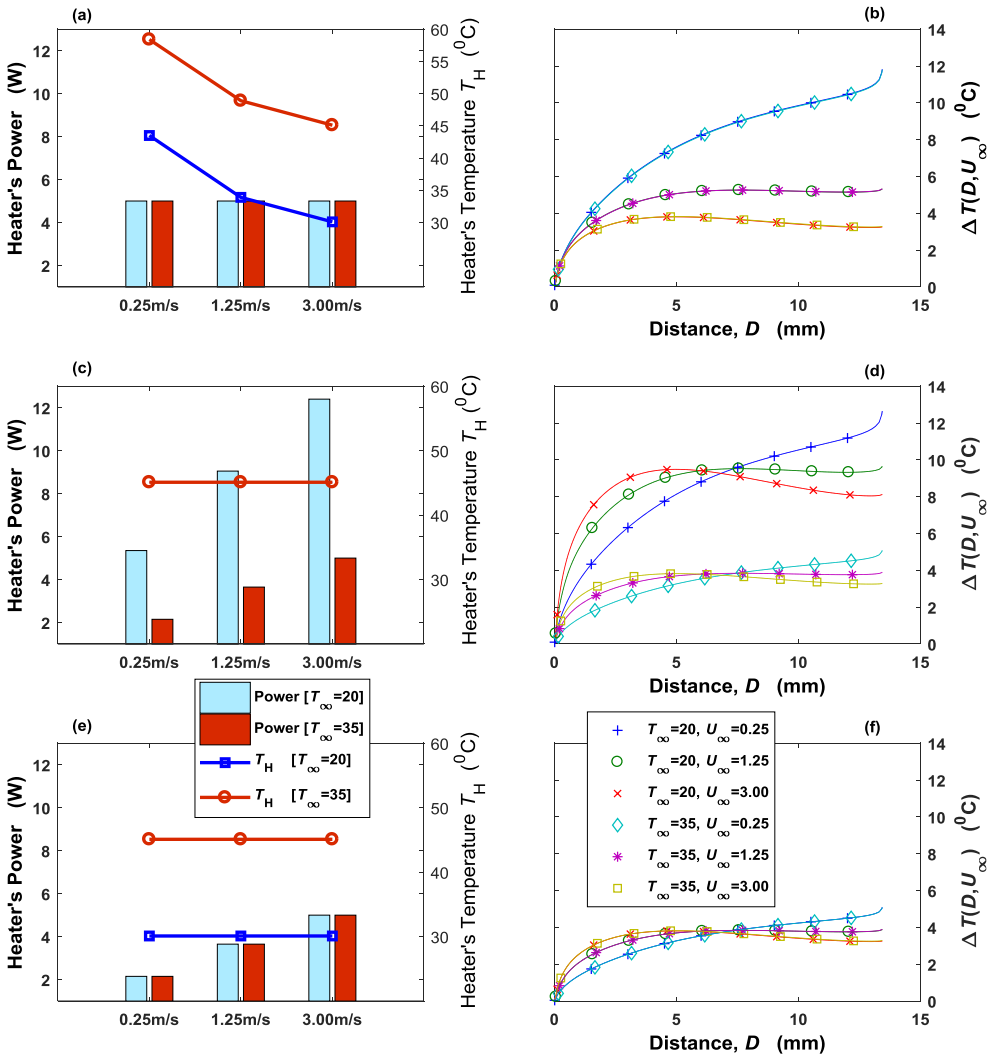

Fig. 3.2: The CP, CT and CTD mode at the first, second and third row, respectively. The power consumption and the heater temperature are shown in the first column. The temperature difference versus the distance from the heater is indicated in the second column.

The CTD operates in a similar manner to the CT, where the inlet temperature must be known in order to regulate the heater's temperature to the correct overtemperature. It also requires the monitoring of inlet temperature for the correct flow measurement. Based on how my experiment has been set up, and according to Fig. 3.2f, the output of the CTD, i.e., ΔT, has the least sensitivity to flows among the three modes. Hence, the CTD mode requires high-resolution temperature sensors for distinguishing small changes of flow rates. However, a significant advantage of the CTD is that it requires

least power among the three modes, as they operate.

All three modes require a certain mechanism of feedback. The CP mode needs to monitor the voltage and current to the heater simultaneously and then regulates the product of the voltage and current, whereas the CT and CTD modes need to regulate the heater temperature and heater-inlet temperature difference, respectively. A precise flow measurement will rely on a speedy response from the heater to different velocities which very much depends upon the thermal time constant of the heater and transducer area. Hence, minimizing the sensor size and keeping the power low help to improve the measurement accuracy and transient response.

The simulation results also validate the King's law:

$$\frac{P}{(T_H - T_\infty)} = A + B\,U^n \tag{3.4}$$

for all the modes as:

$$\frac{P}{(T_H - T_\infty)} = 0.093 + 0.24\sqrt{U} \tag{3.5}$$

3.1.2.2 Optimisation of Heater to Temperature Sensor Distance

For each mode, each velocity corresponds to a temperature difference between the two temperature sensors. This difference, i.e., ΔT, for the same velocity, alters as the point of measurement moves away or closer to the heater. I prefer to focus on 0.25 and 1.25 m/s velocity values since they include the most important volume rate range of human respiration. For each mode separately, the goal is to find the distance from the heater where the absolute difference between the $\Delta T_1(D, U_\infty=1.25)$, and $\Delta T_2(D, U_\infty=0.25)$ is the greatest, hence, to increase output range and sensitivity.

The reason I am looking for the spot of the greatest difference in the outputs is that for a pre-defined number of resolution steps, the size of measurement step increases as the difference becomes greater, simplifying the temperature sensor design to a certain extent. Consider 30 steps between the 0.25 and 1.25 m/s or, a resolution of approximately 0.033 m/s. By placing the temperature sensors 1.8 mm far from the heater while using the CTD mode, the necessary resolution for the temperature sensors

will be 0.8 / 30 = 0.027 °C (the 0.8 value is derived by the CTD plot of Fig. 3.3a at 1.8 mm). However, if the temperature sensors are placed 0.3 mm away from the heater, the resolution becomes 0.4 / 30 = 0.013 °C, making the temperature sensor design more challenging, requiring a temperature sensor with a finer resolution for the same velocity resolution (0.033 m/s).

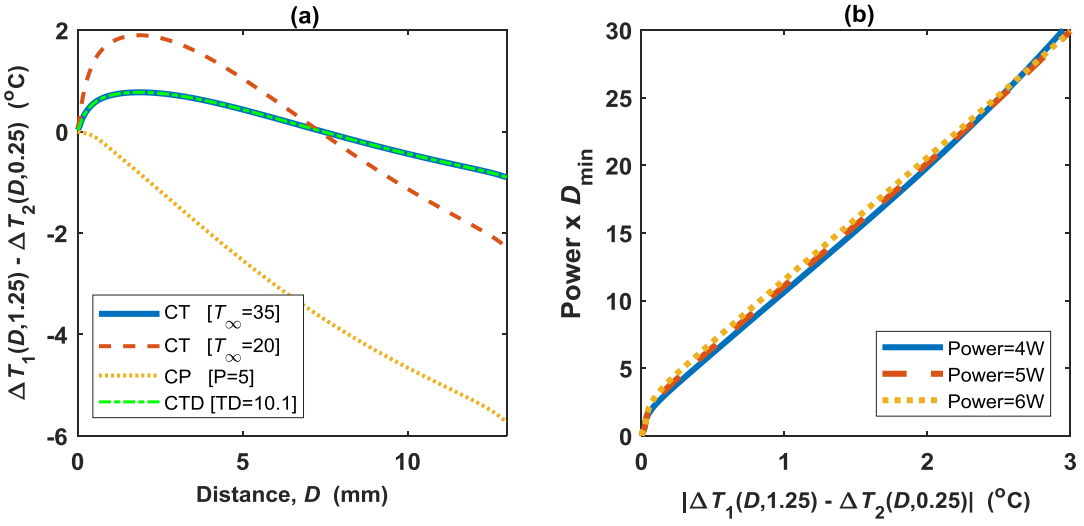

Fig. 3.3: (a) Output difference for 0.25 to 1.25 m/s, for all distances away from the heater. The "CT [T_∞=35]" overlaps with the "CTD". (b) $\bar{P}$ x D_{min} vs. output difference for different power consumptions in the CP mode.

Also, Figs. 3.2d and 3.2f suggest that for the CT and CTD modes there is a certain distance D_x where the output $\Delta T(D_x,U_\infty)$ is relatively constant regardless of the U_∞. It is that point in Fig. 3.3a where the output difference is zero. Evidently, D_x must be avoided as the position to place the temperature sensors since the flow sensor becomes rather insensitive to velocity variations. Figs. 3.2d and 3.2f also show that for $D<D_x$ the output increases as the flow increases, while for $D>D_x$, it decreases for an increasing velocity. Hence, if large D is not an issue, larger than D_x distances can be chosen if one is more interested in the lower end of the velocity range. In addition, by comparing the two CT curves in Fig. 3.3a, it is evident that for a given temperature sensor with known measurement accuracy, it can measure low-temperature flows more accurately than high-temperature flows.

The simulation suggests that for the CP mode, the temperature sensors should be placed far from the heater for the highest $|\Delta T_1 - \Delta T_2|$. In previous studies, the heater

power was usually decided according to the predefined temperature sensor's resolution and pre-defined temperature sensor locations. However, that would be an optimisation process towards only the power. The simulation results of this work suggest that the necessary temperature sensor resolution is affected by both the heater power and temperature sensor-heater distance which should be optimised together. The simulation results in Fig. 3.3a suggest that one can get a 30-step of 0.02 ^{o}C resolution between 0.25 m/s and 1.25 m/s (i.e., $\Delta T_1(D,1.25) - \Delta T_2(D,0.25) = 30 \times 0.02 = 0.6$ ^{o}C) using either the CTD, the CP or the CT mode and by placing the temperature sensors at 0.6, 1.45 and 0.6 mm respectively (for the CT the case of 35 ^{o}C inlet temperature is considered). To have a single parameter which allows us to optimise power and size at the same time, a figure of merit is proposed which is defined as follows:

$$\text{FoM} = D_{\min} \times \bar{P} \tag{3.6}$$

where $D_{\min}$ is the minimum distance needed to achieve the necessary resolution, and $\bar{P}$ is the average value of heater's power over the inlet temperature and velocity range of interest. For both, CT and CTD mode, $\bar{P}$ can be calculated using (3.5) and the mean value theorem of integrals, thus:

$$\bar{P} = \frac{1}{U_B - U_A} \int_{U_A}^{U_B} P \, dU \tag{3.7}$$

$$\bar{P} = \frac{1}{T_B - T_A} \frac{1}{U_B - U_A} \int_{T_A}^{T_B} \int_{U_A}^{U_B} P \, dU dT_\infty \tag{3.8}$$

where (3.7) refers to CTD and (3.8) to CT mode. U_A, U_B, T_A and T_B are equal to 0.25 m/s, 1.25 m/s, 20 ^{o}C and 35 ^{o}C, respectively. Table 3.2 shows that for 0.033 m/s (0.02 ^{o}C) resolution, the $\bar{P}$ for the CP, CT, and CTD is 5, 5.22 and 2.996 W, respectively. The $D_{\min}$ in Table 3.2 is extracted from Fig. 3.3a. Among the three different modes, the CTD has the lowest FoM for the given velocity range and measurement resolution. It results in significant power and size reduction at the expense of the incoming fluid's temperature monitoring.

The same analysis and FoM calculation can be applied to any other velocity range or experimental setup, providing a generic methodology for the optimisation of

calorimetric flow sensors. It can also be applied on a single mode. Since CP plot in Fig. 3.3a is monotonic for the distance range presented, the distance D corresponds to the D_{min} for the relevant output difference. Fig. 3.3b shows the product of $\bar{P}$ and D_{min} achieved over a range of output difference for different power values in the CP mode. The very similar product suggests that an increase in the heater power means the sensor size, which is described by D_{min}, can be decreased by the same factor and vice versa. Hence, it indicates the interplay and the equal importance of P and D_{min} and the fact that they should not be considered as two independent factors to optimise.

TABLE 3.2: FoM of the modes under test

Mode	D_{min} *(mm)*	$\bar{P}$ *(W)*	FoM *(mm×W)*
CP	1.45	5.000	7.25
CT	0.60	5.220	3.13
CTD	0.60	2.996	1.80

3.2 Asymmetrical Sensing Configuration For High Flows in CP Mode

Section 3.1 studied the effect of distance between the heater and the sensing elements of a symmetrical pair, consisting an important addition to the relevant literature [85][83]. However, studies of the effect of the asymmetrical locations of temperature sensors are rare. Nguyen and Dotzel [86] firstly used asymmetric topologies for flow measurements using CP mode for low flow rates (μL/min). However, they preferred to use one pair of temperature sensing elements and multiple asymmetrically located heating elements. Such a topology has the benefit of smaller transducer area when thermopiles are used, however, the flow sensor can operate using only symmetrical or asymmetrical locations at a time, but not combined. In [62], the authors have also studied the asymmetrical position of temperature sensing elements for constant current (CC) and constant temperature (CT) mode. However, as the authors stated, the CC measurements on a heater of high temperature coefficient are not as reliable as CT, while CT mode is not easy to implement.

On the other hand, CP offers simple implementation and reproducible

measurements. This section investigates and proves that the use of asymmetrical locations in CP mode improves substantially the sensitivity of the flow sensor after the turn-over velocity, a range sometimes unused due to its low performance in this mode. In the following sections, the experimental setup and results are presented.

3.2.1 System Setup

3.2.1.1 Sensor Board and Housing Box

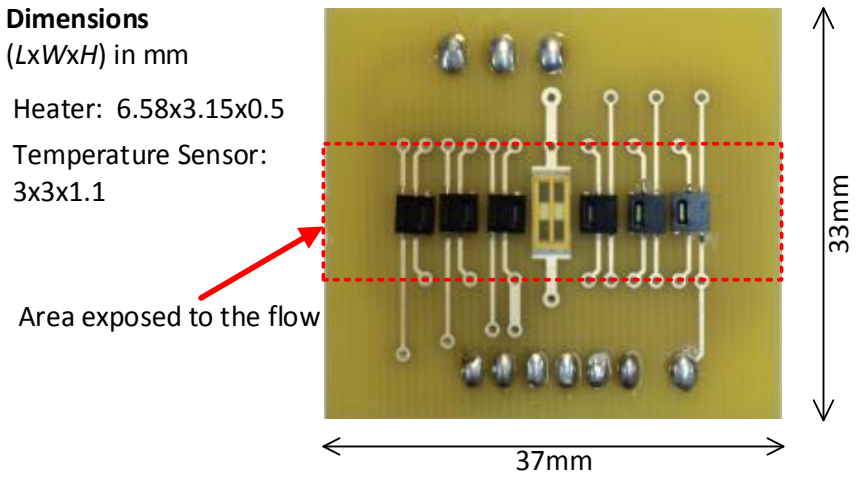

Fig. 3.4: Photo of the sensor board. The dimensions are stated and the area exposed to fluid is demonstrated

Fig. 3.4 depicts the calorimetric flow sensor used for the experiments and it is made of off-the-shelf components mounted on a typical 1.6 mm thick FR4 printed circuit board (PCB). It consists of a surface mount 10 Ω thin film resistor from Vishay® used as a heater, and six digital IC temperature sensors from Sensirion® (STS21). PCB offers a relatively low thermal conductivity compared to Si-based flow sensors, hence, MEMs techniques are not needed in order to achieve thermal isolation of the sensor's components. The temperature coefficient of the heater is 25 ppm which corresponds to a maximum deviation of resistance of 0.125% for a temperature range of 50 ^{o}C. In such a case, constant current on the heater can be considered as constant power with negligible error. The maximum power rating of the resistor is 2.5 W.

The digital IC temperature sensors are placed in pairs symmetrically in respect to the heater and in distances of 0.7, 3.35 and 8 mm, as Fig. 3.5 depicts. Each of these sensors incorporates a 14-bit ADC that provides a resolution of 0.01 ^{o}C and they can communicate with a micro-controller (MCU) using the I^2C protocol. I^2C is a rather popular serial, synchronous communication protocol. Its popularity is based on its simplicity and the fact that only two wires are needed: one for data, and one for the clock, usually referred as SDA and SCL, respectively.

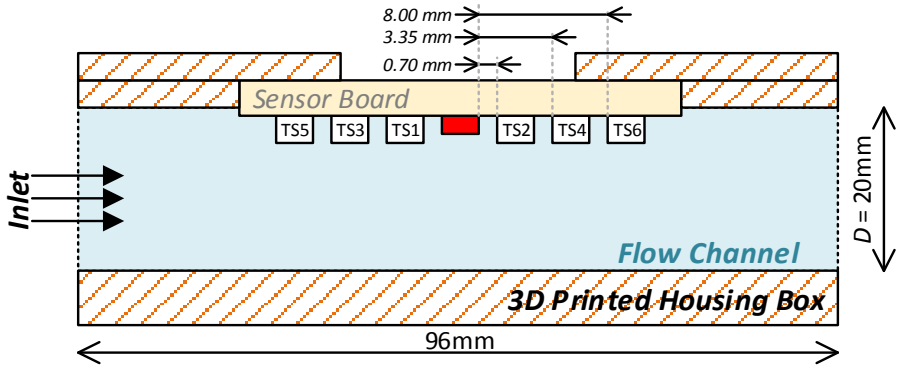

Fig. 3.5: Cross-sectional drawing view of the housing where sensor board is placed. The heating element is in red colour. TS1 to TS6 are the temperature sensors 1 to 6.

Compared to RTDs and thermopiles, both used extensively in the literature as temperature sensing elements in flow sensors, the digital temperature sensors have two advantages: firstly, the benefit of reduced noise since the measurement is converted into digital signal within the same chip. Secondly, it simplifies substantially the rest of the circuit design since there is no need for extra amplifiers or a Wheatstone bridge.

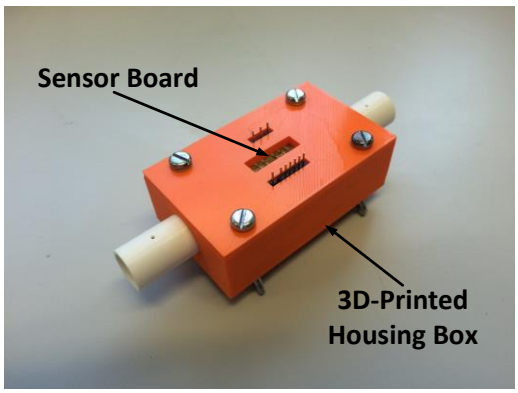

Fig. 3.6: The 3D-printed housing box carrying the sensor board.

The sensor board is then mounted in a customized 3D printed housing box (Fig. 3.6) made of PLA. It is designed to fit the sensor board perfectly, leaving only the sensing area exposed to the flow while providing access to the back of the board for the connections. The housing creates a cylindrical flow channel of 20 mm diameter and 96 mm of length, as shown in Fig. 3.5.

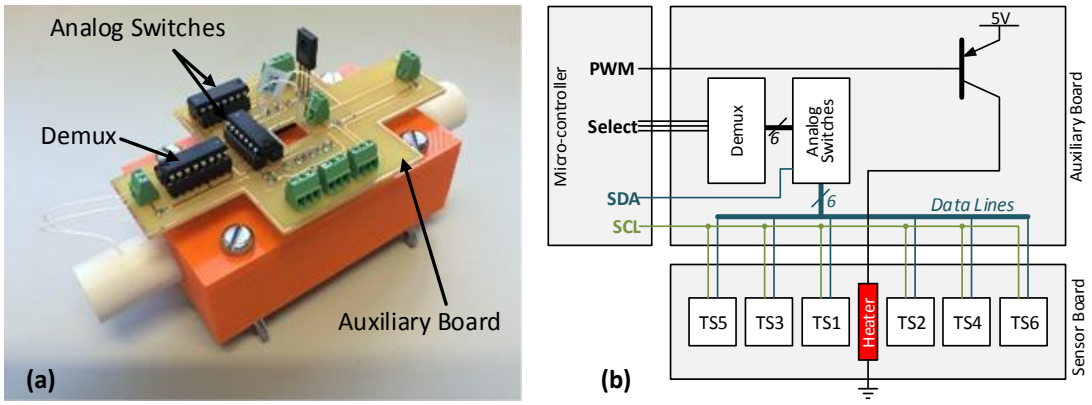

Fig. 3.7: (a) The housing box with the aux board mounted. (b) Schematic drawing of the PCBs and their connection to the MCU.

3.2.1.2 Auxiliary Board and Micro-Controller

An auxiliary (aux) PCB has also been designed to acquire the measurements from the temperature sensors and supply the heater with power. As Fig. 3.7a depicts, the aux board is directly connected to the sensor board. As Fig. 3.7b shows, the aux board carries a demultiplexer (demux) and the analog switches, necessary for the communication between the MCU and the temperature sensors. The reason is that all the digital temperature sensors have the same address, while the MCU has only one data line (SDA) for the I^2C protocol. Therefore, analog switches are used in order to connect the SDA from the MCU to the right sensor every time when this is necessary. A 3-to-6 demux is used in order to reduce the number of connections to the MCU, thus, only three select signals are needed from the MCU to control the six switches. The clock line (SCL) can be shared among the sensors without causing any issue. Also, the aux board has a pnp transistor, with its emitter connected to 5V external supply, which is used to drive the heater. The power at the heater is regulated with the application of a Pulse Width Modulation (PWM) signal to the transistor's base

generated by the MCU. Such a topology is preferred since the MCU is not capable of providing the heater with the necessary power. For the experiments presented here, an Arduino® is used as a MCU and the frequency of the PWM is at 490Hz.

To acquire the temperature sensors' measurements, the MCU asks all the IC sensors simultaneously to get a single measurement, hence, all the sensors start measuring at the exact same time. The typical time a sensor needs to get a single measurement is 66 ms and its last reading is stored within the IC chip. Then, the MCU asks each sensor, one after the other, to send their readings. The whole process of measuring and sending the readings to the MCU lasts 200 ms, hence, the sampling frequency is set at 5 Hz. This frequency is adequate for the majority of industrial and medical monitoring processes where only slow flow changes occur. The duty cycle of the PWM was set to 50/255 for a reference voltage of 5V, unless otherwise stated, which corresponds to an analog voltage of 0.98V at the base of the transistor. Subsequently, the current at the heater was measured at 0.383 A, and the power at the heater at 1.47 W. Note that the convective heat energy leaving the heater is directly related to the velocity of the fluid, hence, the power level supplied to the heater of a calorimetric sensor must increase in order to still be able to create a temperature gradient in high fluid velocities.

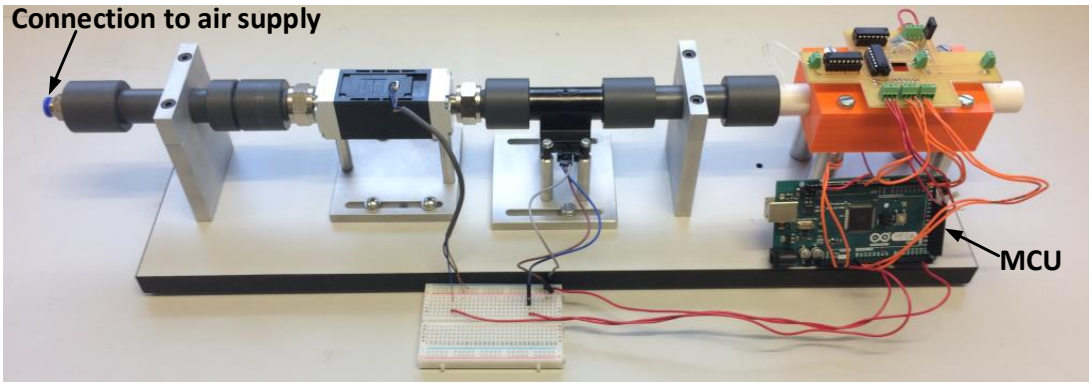

Fig. 3.8: The setup: The housing box is mounted at the end point of the structure. A micro-controller is connected to the sensor board (through the auxiliary board), and to the commercial flow sensors.

The housing box with the boards is then mounted in a setup of pipes, as Fig. 3.8 depicts, which facilitates the connection to fluid supply. The fluid used for the experiments is air and a Mass Flow Controller (MFC) from Bronkhorst® is used to control the flow. Using the MFC, the user has the ability to determine the flow rate, as

well as, to create different flow patterns and flow tests necessary for the experiments. The MFC used for this work can control and create flows up to 50 standard liters per minute (slm) with a setting resolution of 0.1 slm and measurement resolution of 0.01 slm. In series and before the housing box, two commercially available flow sensors are placed, one from OMRON®, and one from Honeywell®. Those sensors can be used as a reference for flow produced by the MFC.

3.2.2 Experimental Results

3.2.2.1 Calibration

Ideally, the temperature measurements between two symmetrical temperature sensors placed at the upstream, T_D^{up}, and downstream, T_D^{down}, and at distance *D*, must be equal when there is no flow, therefore, $\Delta T = T_D^{down} - T_D^{up} = 0$. However, practically this is not the case due to two main reasons:

- Measurement error of the sensors: the digital temperature sensors used have inherently an inaccuracy that differs from chip to chip. Hence, it is highly likely the temperature sensors produce a different output for the exact same temperature.

- The fact that their distances from the heater cannot be practically equal, hence not absolutely symmetrical to the heater. Therefore, the temperature at the exact spots where the temperature sensors are placed is not the same since their distance to the heating source is not the same.

Therefore, the offset of each pair is determined and removed. Before performing the experiments, the heater is on for 5 minutes without any flow through the air channel, providing more than enough time for the system to warm up. The average value of ΔT of the last minute for a measuring pair is calculated and removed as an offset from the measurements. As it was expected, the offset is larger for a pair closer to the heater than a pair far from it, since the ratio of misplacement, ε_D, over the heater-to-temperature sensor distance, *D*, becomes smaller as *D* increases.

3.2.2.2 Symmetrical Measurements

Fig. 3.9 shows the output of the flow sensor using symmetrically located sensing elements. After a certain flow rate, the output increases quickly for low velocities until it reaches a maximum, known as turn-over flow rate, and then slowly decreases almost linearly. Apparently, such a topology and mode of operation are quite limiting when the application requires accurate measurements of high fluid velocities. For the current test, the absolute gradient of the plots for flows between 25 to 50 liters is 0.062, 0.044 and 0.053, for the pairs TS2-TS1, TS4-TS3 and TS6-TS5, respectively. Considering the resolution of the temperature sensors used, the flow resolution ideally would be at 0.16 slm, 0.23 slm and 0.19 slm, respectively. It must also be noted that the lowest resolution occurs for the pair closest to the heater, validating the importance of distance *D* on sensitivity as discussed in section 3.1.

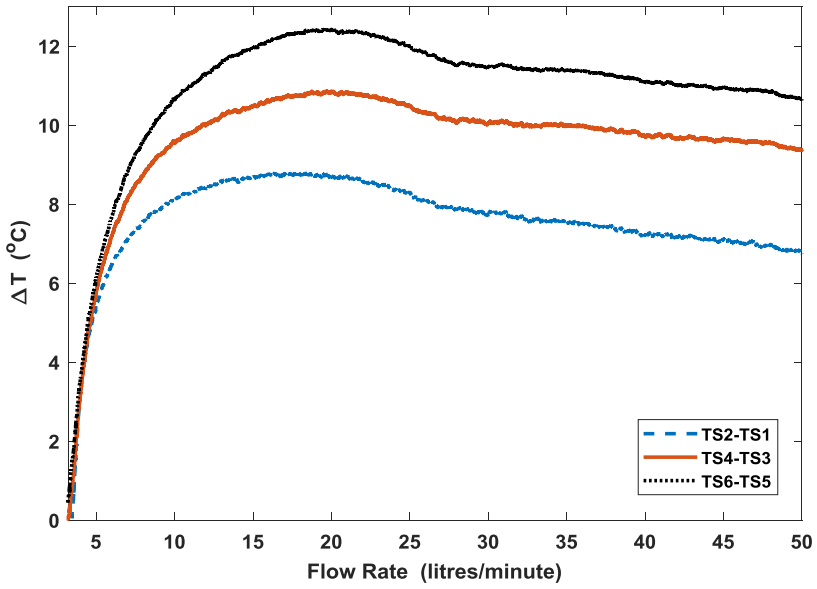

Fig. 3.9: Flow sensor's output using symmetrical pairs of temperature sensors. The pair TS2-TS1 is the one closest to the heater, while the pair TS6-TS5 the one further away from the heater.

3.2.2.3 Asymmetrical Measurements

Fig. 3.10 depicts the temperature difference between the sensor closest to the heater at the downstream (TS2) and sensor at the longest distance at the upstream (TS5), as well as, against the one in the middle (TS3), for the exact same measurement setup mentioned in the previous paragraph. Bear in mind that an offset is expected to occur due to the asymmetry and it is calculated and removed in the same way as in the

symmetrical measurements. Firstly, note that the maximum output occurs for a lower flow rate than that of the symmetrical topology, noticeably increasing the flow range of linear output for the high fluid velocities. Most importantly, the gradient of the output for that range is now approximately 0.26 and 0.18 for the pairs TS2-TS5 and TS2-TS3, respectively, ideally offering a flow resolution of 0.038 slm and 0.056 slm, respectively again. This is an up to six-fold improvement in resolution for the same power compared to that of the symmetrical pairs.

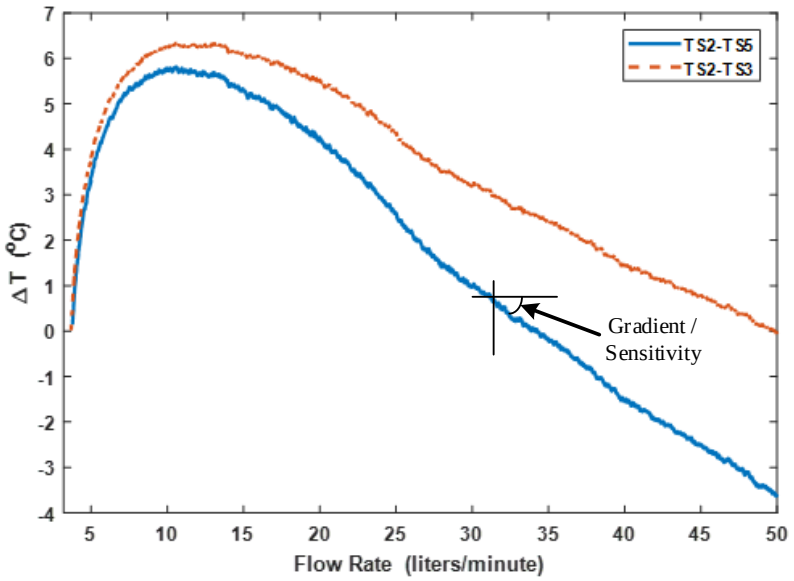

Fig. 3.10: Flow sensor's output using asymmetrical pairs of temperature sensors. Figure demonstrates that as the asymmetry increases, the sensitivity of the flow sensor at the output increases for flow rates greater than the turn-over point.

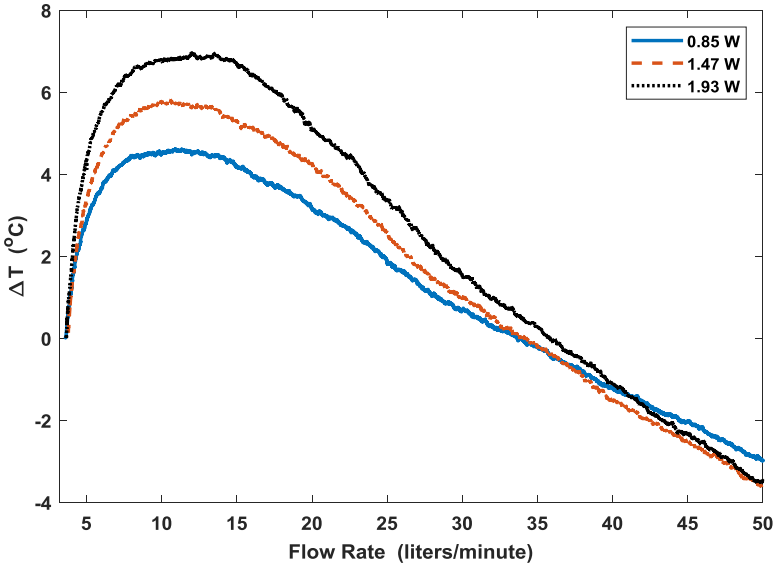

Fig. 3.11: Flow sensor's output using the asymmetrical pair TS2-TS5 for different power ratings at heater.

An apparent issue of measuring flow rates after the turn-over flow rate is the non-monotonicity of the output; hence, the same ΔT might correspond to two different flow rates. This can be easily resolved with the use of the T_{OVER}. In CP mode, the T_{OVER} changes as the flow rate varies, while a specific overtemperature, $T_{OVER,TO}$, is achieved at the turn-over flow rate. Therefore, the measured flow rate at any given moment, Q_M, can be determined by the sensor's output, ΔT_M, and whether its overtemperature, $T_{OVER,M}$, is greater or smaller than the $T_{OVER,TO}$.

3.2.2.4 Effect of Power

The effect of different power applied to the heater on flow resolution for asymmetrically located sensing elements has been also investigated. Fig. 3.11 shows the flow sensor's output using the TS2-TS5 pair as measuring sensors, for two more power consumptions, one lower at 0.85 W, and one higher at 1.93 W, defined by different PWM duty cycles. It can be extracted from the data that the flow resolution is 0.048 slm, 0.038 slm and 0.034 slm for the 0.85 W, 1.47 W and 1.93 W, respectively. It is proven that the trend for the flow resolution, when the power increases, is to also increase. However, it must be noted that the turn-over point moves to the right side with the increase of the power reducing the available flow range after the turn-over.

TABLE 3.3: Output sensitivity for flows larger than the turn-over for the pairs of temperature sensors under test

	Pair	**Sensitivity** ***(|°C litres^{-1} min|)***
Symmetric	TS2-TS1	0.062
	TS4-TS3	0.044
	TS6-TS5	0.053
Asym.	TS2-TS3	0.180
	TS2-TS5	0.260

3.3 DISCUSSION

This chapter investigated the effect of the temperature sensor's position in the flow sensor's performance, as a symmetrical pair, as well as, asymmetrical. A model

for the optimisation of medical calorimetric flow sensors for respiratory monitoring applications to facilitate the design of temperature readout circuits, such as ADCs, has been developed. A novel Figure of Merit has been proposed, greatly simplifying the multi-dimensional optimisation process in the design of calorimetric flow sensors, and proving for the first time the interplay between distance *D* and heater power. The performance of operating the heater in the CP, CT and CTD is compared. The simulation results presented in section 3.1 suggest that the CTD mode offers the best FoM for the given velocity range and measurement accuracy. Although the analysis and simulation in the paper were based on designs in the mm scale, the same principle and optimization process can be applied to any thermal flow sensor, including integrated sensor in sub-mm scale.

The second part of this chapter is more focussed on the CP mode. CP is commonly chosen due to its reliability and simple implementation, most of the times for low flow velocities and usually avoided for high flow rates due to its slowly changing output after the turn-over velocity. This work provides experimental evidence that asymmetrical locations of sensing elements can be used to practically solve that problem by increasing the sensitivity of the sensor for the same setup conditions while increasing the measurement without compromising the power budget, by moving the turn-over point to a lower velocity.

3.4 CONCLUSION

This chapter provided strong evidence of the great effect of the temperature sensor's position on the flow sensor's performance. In particular:

- The correlation between the heater's power and the distance (between the heater and the temperature sensor) has been proven, reducing the variables of a flow sensor's design.
- A Figure of Merit based on average expected power and the minimum distance needed to achieve to the required resolution has been proposed: $\mathrm{FoM} = D_{\min} \times \bar{P}$. The lower the value of FoM, the better.
- Experimental measurements demonstrate that the sensitivity after the turn-over point, and the measurement range can be substantially increased using

asymmetrically placed temperature sensors.

- For the setup presented, the sensitivity after the turn-over point increased almost 6 times for the same setup, without any change in power, but by only playing around with the flow sensor's geometry.

4

HEATER CONTROL CIRCUIT DESIGN: TOWARDS LOW-POWER AND BIOMEDICALLY SAFE THERMAL FLOW SENSORS

Thermal flow sensors need a heater control system to deliver the power at the heater. This heater control system is in charge of delivering the necessary power to the heater according to the operation mode of choice, such as CP or CTD. It is important that the heater control circuit operates accurately and according to the relevant equations so one can get reproducible results.

This chapter presents a brief overview of the main disadvantages of the prevalent topologies, and suggests a new heater control circuit for each mode of operation to address them. Then, it introduces a novel heater control circuit that consists a combination of the newly proposed control circuits, enabling flow sensor's multi-modal operation. Multi-modal operation allows the flow sensor to toggle between the operation modes, based on parameters such as power consumption or heater's temperature, addressing common issues of each mode which could not be resolved by modifying their individual heater control circuits. Solving these issues makes the use of thermal flow sensors more appealing since they can be safely used in biomedical applications or in industrial applications with inflammable gases.

4.1 DRAWBACKS OF EXISTING TOPOLOGIES

As described in previous chapters, the governing equation for heater's operation is derived by King's law [33]:

$$\frac{P}{T_H - T_\infty} = A + BU^n \tag{4.1}$$

where P is power at the heater, T_H and T_∞ are the temperatures of the heater and the ambient, respectively, U is the medium's velocity, and A, B, and n are constants that depend on fluid's properties and materials. Therefore, to acquire meaningful flow measurements from either, hot-wire or calorimetric topologies, the flow sensor must operate in one of its modes of operation. Some of the most common modes are the constant power (CP) where the power, P, at the heater is kept constant all the time, and the constant temperature difference (CTD) where the overtemperature, $T_{OVER} = T_H - T_\infty$, remains unchanged under any circumstances.

However, each mode has its own drawbacks, most of them mentioned in chapter 2. Considering the intended application of the flow sensor, the main disadvantage of CP is that the heater's temperature, T_H, can rise substantially in low or zero flow, which might cause discomfort or burn when the sensor is used for biomedical applications as an implantable flow sensor. In addition, it consists potential hazard and raises safety concerns when inflammable gases are intended to be measured. In contrast, temperature overshoot is not an issue for the CTD, however, power consumption can be difficult to be predicted when the flow is expected to vary substantially, hindering portability. Also, excessive power might be needed in high flow rates to maintain the overtemperature, which the circuit might be unable to provide, leading to erroneous flow measurements.

Other modes can be also found in the literature, such as the constant temperature (CT) referring to constant temperature at the heater, T_H. However, it has been experimentally proven that it is important to compensate for the ambient temperature to get reproducible results [39]. Hence, CT can be reliably used when the ambient temperature, T_∞, is constant, or by compensating for the T_∞ at a later stage of the readout. However, CT is a rather popular mode found in the literature due to its relatively easy implementation. In addition, CT has a great advantage when it comes

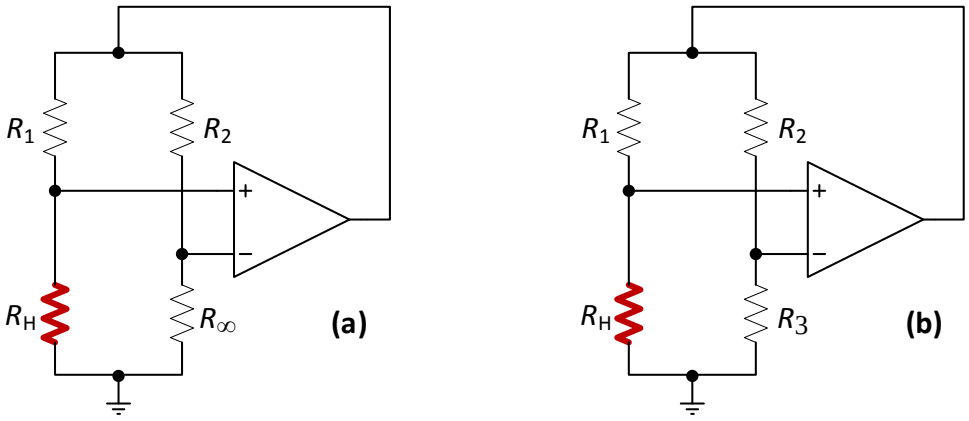

Fig. 4.1: A Wheatstone bridge used as a heater control circuit in (a) CTD, and (b) CT mode. R_H and R_∞ are the heating element and the ambient temperature sensing element, respectively.

to safety precaution since the heater's temperature can be selected in a way that makes the sensor safe for biomedical or industrial use.

Apart from disadvantages on their operation as mentioned above, most of the modes have issues on circuit design level. The most common topology to create the CTD and CT modes are shown in Fig. 4.1. It is a Wheatstone bridge where the values of the resistors have been carefully selected to establish the desired ratio for the CTD:

$$\frac{R_H}{R_\infty} = \frac{R_1}{R_2} \tag{4.2}$$

and the desired value for the CT:

$$R_H = \frac{R_1}{R_2} R_3 \tag{4.3}$$

where R_H is the heater, and R_∞ is the ambient temperature sensing resistor. However, there are two main issues with this topology. Firstly, the branch of R_H requires substantial current to operate as a heater, while the R_∞ for the CTD needs minimal current to avoid any self-heating. This means that R_∞ must be multiple times larger than R_H, which might lead to impractical resistance values. Secondly, unless the resistances of R_H and R_∞ are exponentially related to their temperature, Wheatstone bridge establishes a constant temperature ratio rather than a constant temperature difference, adding an error to the measured value of the CTD mode. Also, note that the R_1 and R_2 must have the same temperature coefficient, and be placed as close to

each other as possible to be at the same temperature. In this way, any resistance variation due to temperature change will be cancelled out. Otherwise, their temperature coefficient must be negligible to not introduce any error to the measurement. Negligible temperature coefficient must be the case for the R_3 for the CT mode, too. In chapter 2, topologies that make use of the temperature difference rather than the temperature ratio have been discussed (Fig. 2.12). However, these topologies still make use of the Wheatstone bridge, thus, the potential issue of R_∞'s self-heating still exists.

For the CP, the constant power is established either with the use of PC software, or with the application of constant current (CC) or constant voltage (CV). However, in the case of CC and CV the variations of R_H due to changes in T_H must be taken into account to reduce the error.

Therefore, it is apparent that there are still challenges to be addressed for the thermal flow sensors; firstly, enhancing the measurement accuracy by improving the heater control topologies, and secondly, broadening their application by making thermal flow sensor safer for biomedical and industrial applications.

The following sections describe the architecture of a multi-modal flow sensor with newly introduced heater control circuits for the different modes. The proposed system can be used as a smart flow sensor for biomedical applications or applications with inflammable gases, while at the same time addresses most of the common issues mentioned above. Specifically, this system can make use of the CT or CTD mode for the low flow rates where the heater's temperature is under control and within acceptable ranges, without spending excessive power. At the same time, it can operate in CP for high flow rates avoiding the increased power consumption of the CT or CTD in high flows, while taking advantage of the increased sensitivity of the CP mode.

4.2 PROPOSED ARCHITECTURE

4.2.1 Principle of Operation

The operation of both, the CT or CTD mode, dictates that the temperature coefficient resistance (TCR) of the heater should be large. High TCR makes the

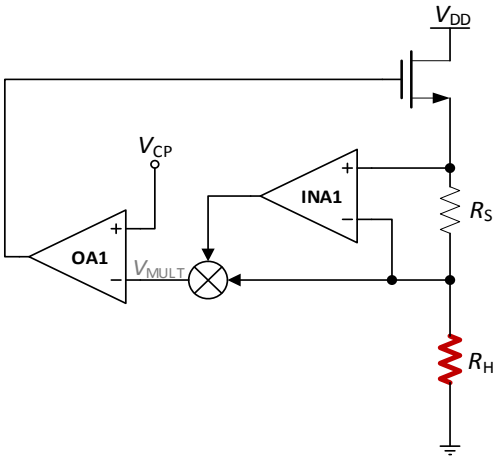

Fig. 4.2: A simplified schematic of the proposed heater control circuit for the CP mode. The sensing resistor R_S is used to quantify the current, and its voltage drop is multiplied by the heater's voltage to calculate the power consumption. The power consumption is defined by V_{CP}.

determination of the required heater's temperature, or of the overtemperature, easier and more accurate. On the other hand, a heater of minimum TCR facilitates the heater control circuit for the CP mode, since it can be replaced with CC or CV mode. If a heater with considerable TCR is to be used in CP, changes in heater's resistance must be considered to ensure the reproducibility of the results. This work proposes a system capable to operate in more than one mode, while the T_H or the T_{OVER} can be accurately and continuously measured for safety purposes, hence, a heater of high TCR is preferred.

Fig. 4.2 depicts the proposed heater control circuit schematic for the CP mode. Similar topologies for constant power supply to a varying load can be found in the literature [87][88]; nevertheless, they are implemented for other applications than heater control circuits for flow sensors. Specifically, a sensor resistor R_S is placed in series for measuring the current through the heater R_H. The voltage drop, V_{RS}, at R_S, and the voltage at the heater, V_H, are fed into an analog multiplier. Assuming G_1 the gain of the instrumentation amplifier INA1, and G_M the gain of the multiplier, the output of the multiplier V_{MULT} should be:

$$V_{\mathrm{MULT}} = G_M(G_1 V_{RS})V_H = (G_M G_1 R_S)\, I_H^2 R_H \tag{4.4}$$

Equation (4.4) states that the output of the multiplier is a linear function of the power at the heater $I_H^2 R_H$. The precision and stability of the two gains, as well as of

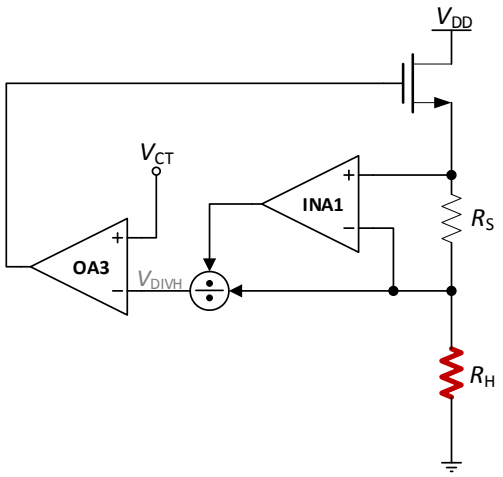

Fig. 4.3: A simplified schematic of the proposed heater control circuit for the CT mode. The heater's voltage is divided by the output of the in-amp INA1 that measures the current. The output of the analog divider corresponds to the resistance of the heater, hence, to its temperature. The heater's temperature is defined by V_{CT}.

the R_S, determine the precision and stability of the measured power. The V_{MULT} is then fed to the negative input of an op-amp OA1, while the positive input is connected to a reference voltage V_{CP} that corresponds to the desired power value for the heater. Hence, the op-amp will create the necessary voltage at its output to drive the heater and match its two inputs. Note that the proposed solution does not include any connection to a micro-controller (MCU) or PC for data processing; the circuit is fully implemented in analog domain and it is a closed-loop, self-regulated circuit based on V_{CP}.

The heater control circuit for the CT mode is similar to that of the CP, however, an analog divider is used instead of an analog multiplier. As Fig. 4.3 depicts the heater's voltage, V_H, is now divided with the output of the in-amp that represents the current flowing, I_H. Assuming that the gain of the divider is G_{DH}, the output of the analog divider will be:

$$V_{\mathrm{DIVH}} = G_{DH}\frac{V_H}{G_1\,V_{RS}} = G_{DH}\frac{I_H\,R_H}{G_1\,I_H\,R_S} = \frac{G_{DH}}{G_1\,R_S}\,R_H \tag{4.5}$$

Assuming that the resistance of the heater is dependent on the temperature as:

$$R_{\mathrm{H}} = R_{H0}\left(1 + TCR\,(T_H - T_{REF})\right) \tag{4.6}$$

where R_{H0} is the nominal resistance value of the heater at temperature T_{REF}, the output

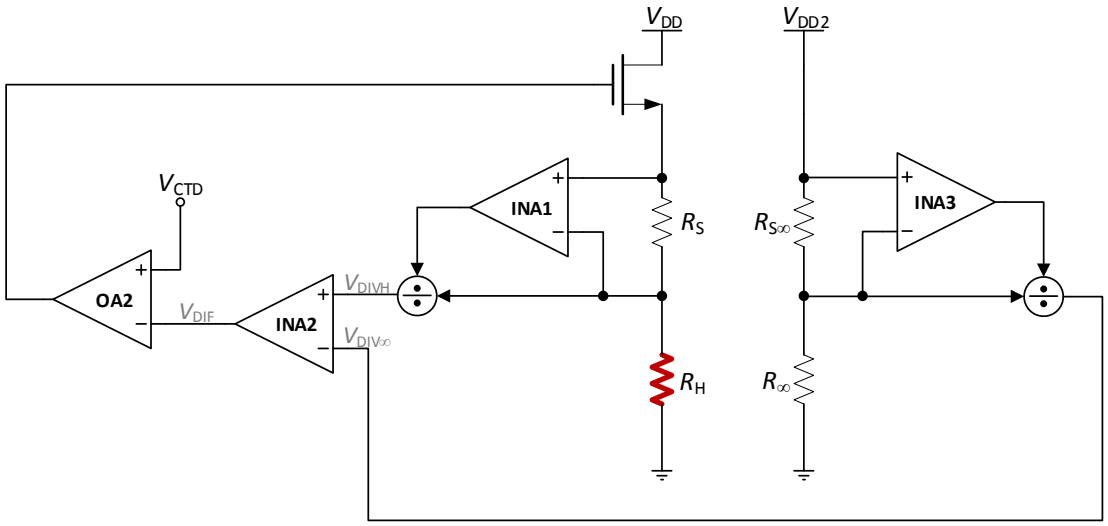

Fig. 4.4: A simplified schematic of the proposed heater control circuit for the CTD mode. Compared to CT, an extra branch has been added to measure the ambient temperature, using R_∞. The resistance of R_∞ is calculated (in a similar way to R_H) and then is subtracted from R_H, to measure the overtemperature. The system settles at the T_{OVER} defined by V_{CTD}.

of the analog divider will be:

$$V_{\mathrm{DIVH}} = \frac{G_{DH}}{G_1 R_S} R_{H0} \left(1 + TCR \left(T_H - T_{REF}\right)\right) \tag{4.7}$$

Considering:

$$G = \frac{G_{DH}}{G_1 R_S} R_{H0} \tag{4.8}$$

equation (4.7) can be re-written as:

$$V_{\mathrm{DIVH}} = G \left(1 + TCR \left(T_H - T_{REF}\right)\right) \tag{4.9}$$

Equations (4.7) and (4.9) clearly show that the output of the analog divider is a linear function of the heater's resistance, thus, it is a function of the temperature developed at the heater. Similar to the CP heater control circuit of Fig. 4.2, V_{DIVH} is fed to the negative input of the op-amp OA3 while its positive input is connected to a reference voltage V_{CT}. Thus, the op-amp will drive the gate of the transistor in such a way to match its two inputs.

CTD mode requires the measurement of the ambient temperature, T_∞, too, therefore, an extra temperature sensing element, R_∞, is added as Fig. 4.4 depicts. This

temperature sensing element needs to have a high TCR to ensure high precision measurements of the ambient temperature. The principle of measurement is similar to that of the heater's temperature presented above; a current sensing resistor, $R_{S\infty}$, is placed in series with the R_∞, and the voltage at R_∞ is divided by the voltage drop at $R_{S\infty}$ using an analog divider. The output of the analog divider is related to the resistance of the R_∞, hence, to the temperature measured using the R_∞. Assuming G_3 is the gain of the in-amp INA3, and $G_{D\infty}$ the gain of the analog divider, the output of the analog divider, $V_{DIV\infty}$, can be calculate as in equation (4.5), and it will be:

$$V_{\mathrm{DIV}\infty} = G_{D\infty}\frac{V_\infty}{G_3\, V_{RS\infty}} = G_{D\infty}\frac{I_\infty\, R_\infty}{G_3\, I_\infty\, R_{S\infty}} = \frac{G_{D\infty}}{G_3\, R_{S\infty}}\, R_\infty \tag{4.10}$$

and assuming that:

$$R_\infty = R_{\infty 0}\left(1 + TCR\,(T_\infty - T_{REF})\right) \tag{4.11}$$

with $R_{\infty 0}$ the nominal resistance of the ambient temperature sensor at temperature T_{REF}, the analog divider's output can be re-written similar to (4.7) as:

$$V_{\mathrm{DIV}\infty} = \frac{G_{D\infty}}{G_3\, R_{S\infty}}\, R_{\infty 0}\left(1 + TCR\,(T_\infty - T_{REF})\right) \tag{4.12}$$

By designing the components in a way that:

$$\frac{G_{DH}}{G_1\, R_S}\, R_{H0} = \frac{G_{D\infty}}{G_3\, R_{S\infty}}\, R_{\infty 0} = G \tag{4.13}$$

the (4.12) can be re-written as:

$$V_{\mathrm{DIV}\infty} = G\left(1 + TCR\,(T_\infty - T_{REF})\right) \tag{4.14}$$

Using (4.9) and (4.14), it can be easily proven that:

$$V_{DIF} = V_{DIVH} - V_{\mathrm{DIV}\infty} = G\ TCR\,(T_H - T_\infty) \tag{4.15}$$

Thus, V_{DIVH} and $V_{DIV\infty}$ are fed into the in-amp INA2, as Fig. 4.4 depicts, to produce the overtemperature at its output. This output, V_{DIF}, is then fed to the negative input of the op-amp OA2, while a reference voltage is connected to the positive input. The high gain op-amp will drive the gate of the transistor in way to match its two inputs.

Note that the nominal resistance of the heater, R_{H0}, and of the ambient temperature sensor, $R_{\infty 0}$, need not to be equal. As (4.13) clearly shows, G is a function of the analog dividers' gains, in-amps' gains, and sensing resistors' values. Such a characteristic offers great flexibility to the designer since those factors can be chosen in a way that satisfy the needs of the application (i.e. no self-heating at the R_∞ branch), and the specifications of the components used for optimal operation.

It is important that the current sensing resistors are of minimum TCR to avoid any temperature effect on those during measurements. Low tolerance is preferred but it is not necessary if the in-amps' gains can be tuned accordingly to satisfy (4.13).

Also note that based on (4.5) and (4.10), the values of the V_{DIVH} and $V_{DIV\infty}$, hence, the calculation of the T_H and T_∞, are independent of the currents flowing through the resistors. Therefore, V_{DIVH} and $V_{DIV\infty}$ remain unaffected by any variations in current during the measurement, and there is no need for highly accurate supply voltages, V_{DD} and V_{DD2}.

However, the TCR of R_H and R_∞ must be equal for the same T_{REF}, to measure the temperature difference accurately. Nevertheless, that is also the case for the prevalent CTD topology shown in Fig. 4.1b. The advantage of the proposed topology at Fig. 4.4 compared to that at Fig.4.1b is that its operation is based on temperature difference, $T_H - T_\infty$, rather than on temperature ratio, when the resistances with linear relation to the temperature are used. That is of great importance in order to satisfy King's law and ensure the reproducibility of the measurements.

Once the different resistances have been measured and the different gains have been set, the heater control circuits presented above can operate in any power, temperature, or temperature difference (for the CP, CT, or CTD mode, respectively) the user wants to, by defining the appropriate reference voltage V_{CP}, V_{CT}, or V_{CTD}. That offers great flexibility since the reference value can change easily, even on the fly. In contrast, for topologies such as those presented in Fig. 4.1 the necessary resistors should be trimmed accordingly every time the reference value needs to change.

The section below presents the actual implementation of each heater control circuit separately, and how they can be combined to create a multi-modal heater control system.

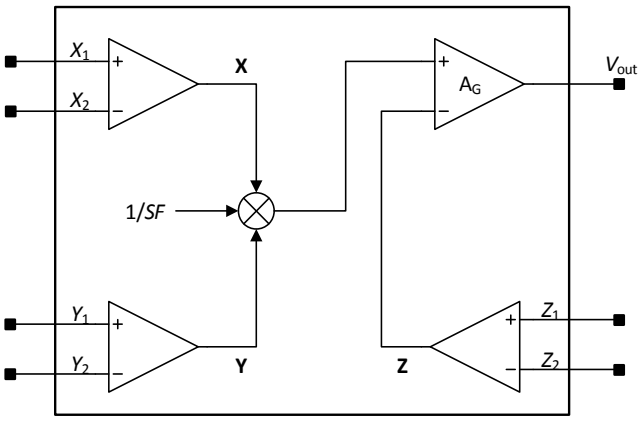

Fig. 4.5: The functional block diagram of the discrete component MPY634, used as analog multiplier and analog divider

4.2.2 Implementation

The previous section described the design and the principle of operation for the proposed heater control circuits for the three main modes, CP, CT, and CTD. This section presents the actual implementation of the designs in printed circuit technology using off-the-shelf components. As mentioned in previous chapters, PCB implementation offers an easy, quick, and inexpensive way to realise and test the proposed, novel designs.

4.2.2.1 Analog Multiplier/Divider

It is evident from the previous section that analog multiplier and dividers are the vital components of the designs, hence, this section starts with the description of the components used for those tasks. Nowadays, most of the manufacturers provide discrete components that incorporate an analog multiplier with extra amplifiers in the same chip. These ICs offer great flexibility, while they simplify the design of topologies that make use of analog multipliers and dividers. In fact, the same chip can be used either as a multiplier or as a divider, depending on how the component's terminals are connected.

The chip that we used was the MPY634 from Texas Instruments, and its functional block diagram is shown in Fig. 4.5. The component has three differential inputs, X, Y, and Z, and a single-ended output V_{out}. The transfer function for the MPY634 is:

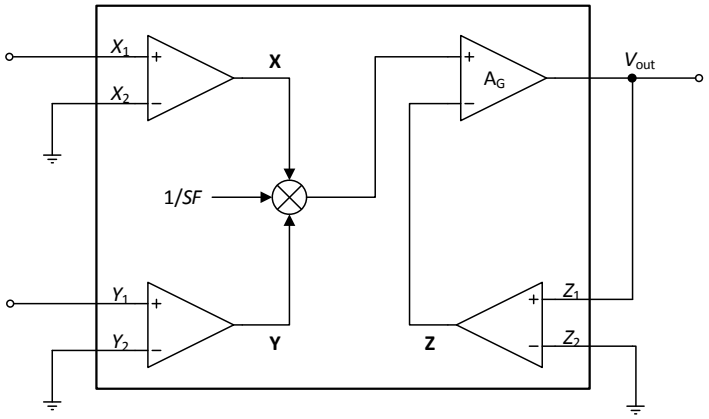

Fig. 4.6: The basic analog multiplier connection for the MPY634

$$V_{out} = A_G \left(\frac{(X_1 - X_2)(Y_1 - Y_2)}{SF} - (Z_1 - Z_2) \right) \tag{4.16}$$

Where A_G is the open loop gain of the output amplifier (85dB at DC according to manufacturer) and *SF* the scale factor. The *SF* is laser-trimmed to 10V, but it can be adjusted from 3V to 10V using external resistors. Since the provided *SF* is of high accuracy within 0.1% or less, I preferred not to use external resistors to modify it. In order to make the chip operate as a multiplier for my design, the connections should be as those shown in Fig. 4.6. Assuming that the gain A_G is infinite, the inputs of the output amplifier must be equal in a closed loop connection, hence, it can be easily shown using (4.16) that:

$$\frac{(X_1 - X_2)(Y_1 - Y_2)}{SF} - (Z_1 - Z_2) = 0 \Rightarrow$$

$$\frac{(X_1 - 0)(Y_1 - 0)}{10} - (V_{out} - 0) = 0 \Rightarrow$$

$$V_{out} = \frac{X_1 Y_1}{10} \tag{4.17}$$

According to (4.17), the gain of the multiplier, G_M, is equal to 0.1. Note that in Fig. 4.6 single ended inputs have been used by connecting the negative input terminals X_2 and Y_2 to the ground. However, differential inputs could be used if needed.

Analog dividers are usually constructed by using an analog multiplier at the feedback of a closed-loop op-amp, as Fig. 4.7 depicts. Ideally, the negative input is

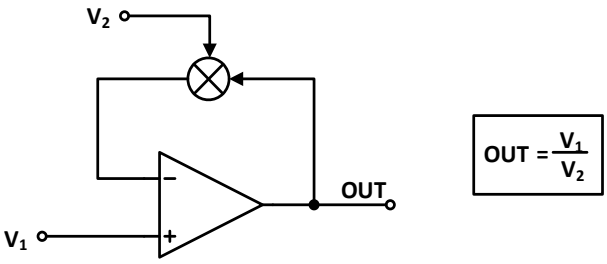

Fig. 4.7: The basic analog divider topology

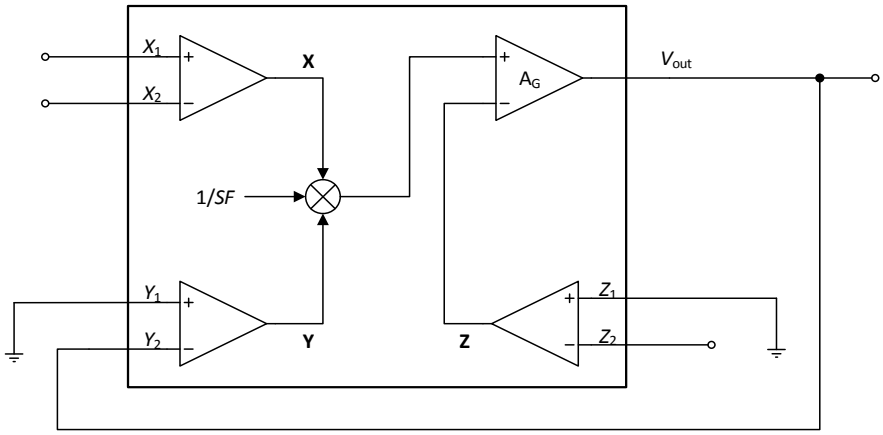

Fig. 4.8: The basic analog divider connection for the MPY634

forced to be equal to the positive input, hence, $OUT \cdot V_2 = V_1 \Rightarrow OUT = V_1/V_2$. In order to create an analog divider using the MPY634, the connections should be as Fig. 4.8 depicts. According to this figure and equation (4.16), it can be shown that:

$$\frac{(X_1 - X_2)(0 - V_{out})}{10} - (0 - Z_2) = 0 \Rightarrow$$

$$V_{out} = 10\frac{Z_2}{X_1 - X_2} \tag{4.18}$$

According to (4.18), the gain of the analog dividers, G_{DH} and $G_{D\infty}$, are equal to 10. Note that in (4.18) a differential input has been considered for the denominator and single ended for the nominator. Nevertheless, the denominator can be a single ended input, too, by connecting X_2 to the ground, and the nominator can be differential by making use of Z_1, if needed.

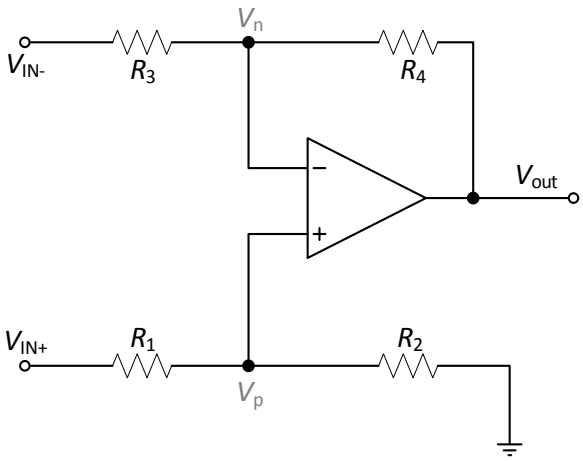

Fig. 4.9: The basic four-resistor differential amplifier

4.2.2.2 Differential Amplifier vs Instrumentation Amplifier

Another important component of my topologies is the in-amp, which has been preferred to the common four-resistor differential amplifier (Fig. 4.9). Although the differential amplifier of Fig. 4.9 looks simple, it might perform poorly. The transfer function of the amplifier in Fig. 4.9 is:

$$V_{out} = \left(\frac{R_2}{R_1 + R_2}\right)\left(\frac{R_3 + R_4}{R_3}\right)V_{IN+} - \frac{R_4}{R_3}V_{IN-} \tag{4.19}$$

Setting $R_1 = R_3$ and $R_2 = R_4$, equation (4.19) simplifies to:

$$V_{out} = \frac{R_2}{R_1}(V_{IN+} - V_{IN-}) \tag{4.20}$$

However, that is almost never the case, because the resistors are never exactly equal, hence, a measurement error occurs. Probably the most affected characteristic of differential amplifier's operation is the common mode rejection ratio (CMRR). A low CMRR means that part of the common mode signal applied at the inputs is amplified and appears at the output. It has been proven [89] that the CMRR using a perfect op-amp for the Fig. 4.9 topology, is:

$$CMRR \cong \frac{A_d + 1}{4t} \tag{4.21}$$

where A_d is the gain of the differential amplifier, and t the resistors' tolerance. Therefore, for unity gain and resistors' tolerance 2%, the CMRR is only 25V/V, or

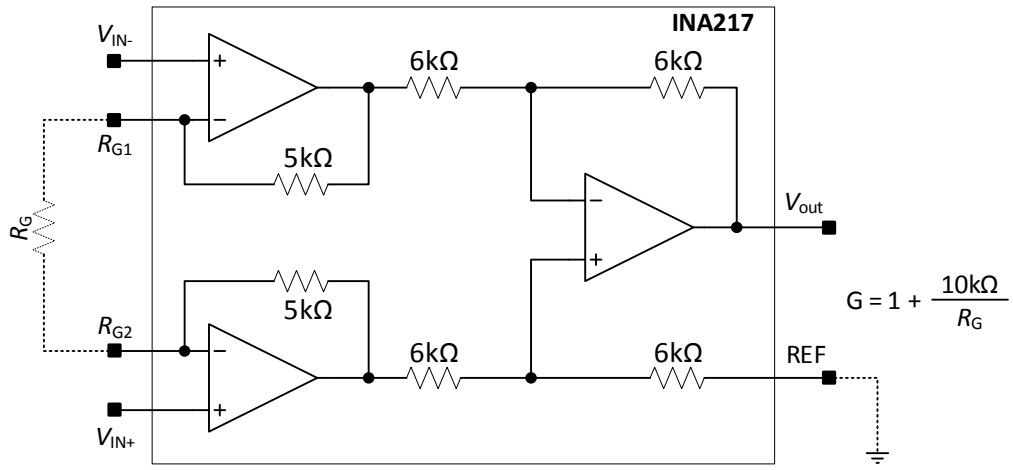

Fig. 4.10: The functional block diagram of the instrumentation amplifier INA217

28dB, which is a substantially small CMRR. Such a low CMRR can lead to instability in closed loop circuits like those presented here. Thus, one must invest on expensive low-tolerance matching resistors while using enough gain A_d, to achieve a good CMRR.

Another potential issue is the possible low input impedance of this topology. Assuming the ideal case where the bias current of the op-amp is zero, it can be proven that the input impedance of the differential amplifier topology is:

$$R_{IN(P)} = R_1 + R_2 \qquad \text{and} \qquad R_{IN(N)} = \frac{R_3}{1 - \frac{R_2}{R_1 + R_2}\frac{V_{IN+}}{V_{IN-}}} \tag{4.22}$$

for the non-inverting and for the inverting terminals, respectively. High input impedance and low bias current are required when accurate measurements are needed, especially in cases such as those of INA1 and INA3 in Fig. 4.4. Otherwise, the measured currents through the sensing resistors R_S and $R_{S\infty}$ will not correspond to the actual currents through R_H and R_∞, respectively.

Due to the aforementioned drawbacks, IC in-amps have been preferred. An in-amp makes use of three op-amps; one connected as a four-resistor differential amplifier, and the other two as non-inverting amplifiers for each signal input. The gain for an IC in-amp is determined by the external resistor R_G which does not require any resistor matching, simplifying the whole design substantially. In addition, the input impedance of both terminals is the same and equal to the input impedance of the input amplifiers, which is usually rather large. For my experiments the INA217 from Texas

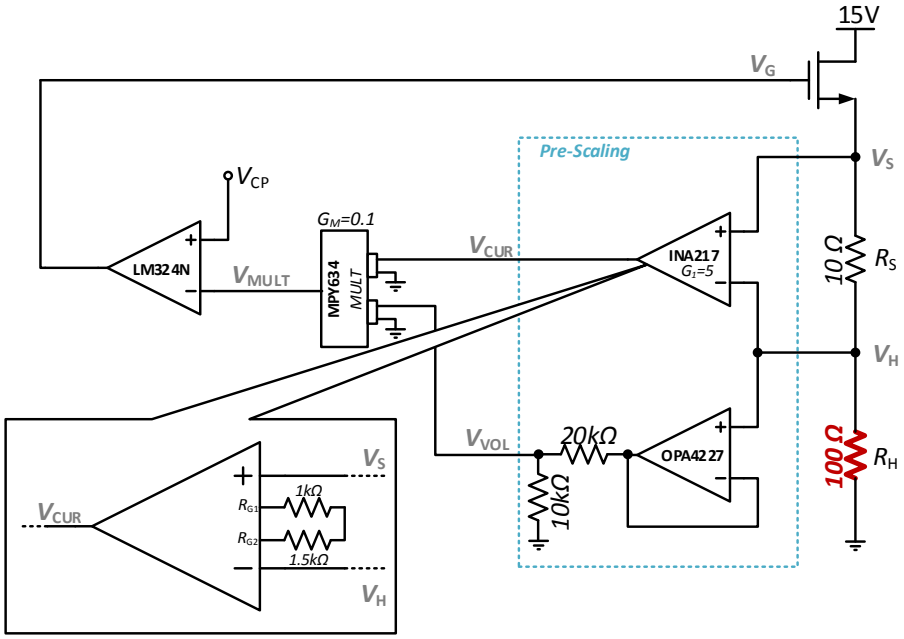

Fig. 4.11: Implementation of heater control for CP mode

Instruments has been used that offer 60MΩ input resistance with a bias current of 2μA, and CMRR equal to 80dB for gain equal to 1. Those are specifications difficult to be matched using a four resistor differential amplifier. For the topology presented in Fig 4.10, it can be proven that the gain of the in-amp is $G_1 = 1 + (10k\Omega/R_G)$, and for gain equal to 1, the R_{G1} and R_{G2} terminals can be left floating.

4.2.2.3 Multi-Modal Implementation on PCB

The actual implementation for the CP, CT, and CTD are shown in Fig. 4.11, 4.12, and 4.13, respectively. For the CP mode, the MPY634 chip is used as an analog multiplier, as explained above. Although, the multiplier has differential inputs, we prefer to use a pre-scaling part that transforms the differential values to single ended. The primary function of the pre-scaling for the presented system is to transform the measured quantities, V_{RS} and V_H, to values that will not challenge the available input and output voltage swing of the MPY634. In addition, they are chosen in a way to satisfy equation (4.13) as it will be shown below. An in-amp INA217 with gain G_1 equal to 5 is used to amplify the voltage drop at the current sensing resistor R_S, and two resistors of low tolerance have been mounted as close as possible to the chip to create the R_G resistance and determine the G_1. A 10Ω resistor has been chosen as R_S. This resistor from Vishay is designed for precision circuits, hence, it has low tolerance of 0.1%, and TCR equal to 2 ppm/°C. To reduce parasitic coupling and the impact of

traces' impedance, R_S has been mounted close to the in-amp input terminals, while the connection traces are of equal length and geometry. To get the right gain G in (4.13), the heater's voltage, V_H, needs to be attenuated by a factor of 3. This could be achieved with a simple voltage divider, however, this could lead to a discrepancy between the current measured at R_S, and the actual current through R_H. Therefore, a unity-gain stable op-amp is used as a buffer before the voltage divider. This is the OPA4227 op-amp from Texas Instruments that features a bias current of only 5nA, substantially smaller than the expected current through R_S. The voltage divider is created using three 10kΩ resistors; two of them connected in series to create a 20kΩ resistor. According to the above and the Fig. 4.11, it can be proven that:

$$V_{CUR} = G_1 \, V_{RS} = 50 \, I_H \tag{4.23}$$

and:

$$V_{VOL} = {}^{1}/_{3} \, I_H \, R_H \tag{4.24}$$

Therefore, taking into account the gain of the multiplier, $G_M = 0.1$, the output of the analog multiplier will be:

$$V_{MULT} = {}^{5}/_{3} \, I_H^2 R_H \tag{4.25}$$

which corresponds to:

$$V_{MULT} = {}^{5}/_{3} \, P \tag{4.26}$$

where P is the power at the heater. V_{MULT} is fed into an op-amp whose specifications are relatively relaxed. Hence, an inexpensive op-amp by Texas Instruments is used.

As a heating element, R_H, a platinum resistance temperature detector (RTD) is used. Basically, it is a resistor made of platinum fabricated in a typical surface mount case, such as those of 0805 or 1206. Platinum RTDs are widely used because they exhibit a linear relationship between their resistance and their temperature, with a large TCR. In addition, they have high accuracy and repeatability, and low drift [90]. They can operate as heaters as long as the achieved temperature is within the temperature limits of the RTD. For the work presented here, a platinum sensor from Innovative

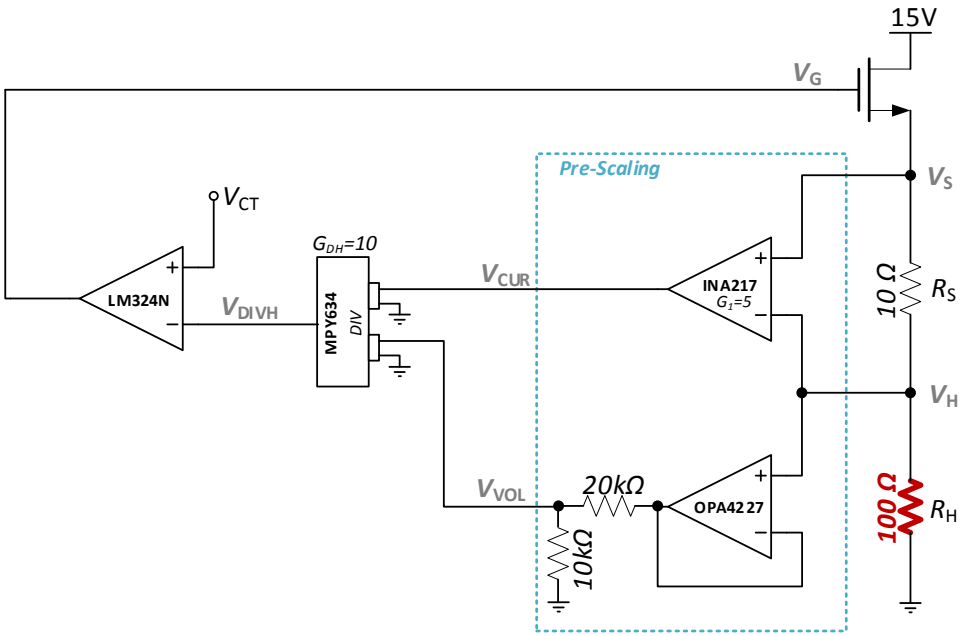

Fig. 4.12: Implementation of heater control for CT mode

Sensor Technology is used. It is a surface mount device (SMD) sensor with a nominal resistance of 100Ω at T_{REF} = 0°C, and TCR of 3850 ppm/°C. The maximum temperature that can be accurately measured according to the manufacturer is 150°C, which is more than enough for my experiments.

The implementation for the CT mode is depicted on Fig. 4.12. The only difference with the CP implementation shown in Fig. 4.11 is that the analog multiplier has been replaced with an analog divider. Hence, considering the equation (4.23) and (4.24), and that the gain G_{DH} is 10, the output of the analog divider will be:

$$V_{DIVH} = G_{DH}\frac{V_{VOL}}{V_{CUR}} \Rightarrow V_{DIVH} = \frac{R_H}{15} \tag{4.27}$$

Using the heater's specifications, equations (4.6) and (4.27), and substituting in (4.9), one gets:

$$V_{DIVH} = \frac{100}{15}(1 + 3.85 \times 10^{-3} \times T_H) \tag{4.28}$$

The CTD implementation is shown in Fig. 4.13. The same platinum RTD from the same company is used as a temperature sensing element, R_∞, in an effort to ensure a matching TCR with that of the R_H. The nominal resistance, however, has been chosen

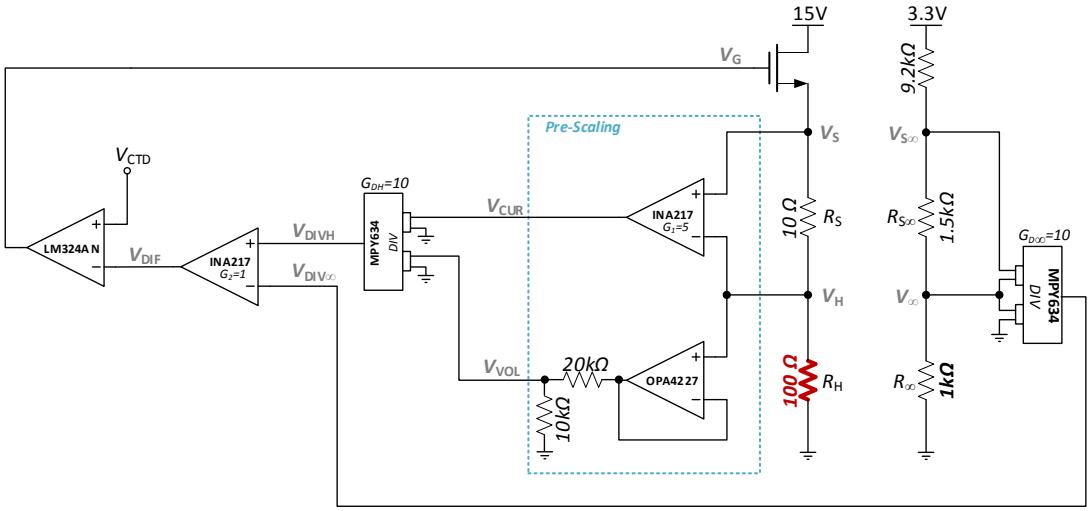

Fig. 4.13: Implementation of heater control for CTD mode

to be 1kΩ, due to the following reason: According to the manufacturer, the maximum suggested current to avoid self-heating at the resistor (hence, to avoid erroneous ambient temperature measurements) is 0.3mA for the 1kΩ RTD, and 1mA for the 100Ω RTD. That means that a voltage drop of approximately 300mV and 100mV, respectively, is expected to be measured. Lab measurements indicated that the error at the output of the analog divider $V_{\mathrm{DIV}\infty}$ increases, when one of the inputs falls below the 100mV. Therefore, the 1kΩ has been preferred. Nevertheless, the nominal values of the R_{H} and R_∞ do no need to be the same, as previously explained. In order to satisfy equation (4.14), $R_{\mathrm{S}\infty}$ has been chosen equal to 1.5kΩ using a low tolerance, low TCR resistor. Therefore, it can be proven that:

$$V_{DIV\infty} = \frac{100}{15}(1 + 3.85 \times 10^{-3} \times T_\infty) \tag{4.29}$$

Also, note that a resistor of 9.2kΩ has been also used in series with $R_{\mathrm{S}\infty}$ and R_∞. Its purpose is to reduce the current below the 0.3mA to avoid self-heating; therefore, there are not any particular requirements for this resistor, hence, a typical inexpensive SMD resistor has been used.

Considering that the gain of in-amp for measuring the temperature G_2 is equal to 1, the output V_{DIF} will be:

$$V_{DIF} = \frac{100}{15}\ 3.85 \times 10^{-3}(T_H - T_\infty) \Rightarrow$$

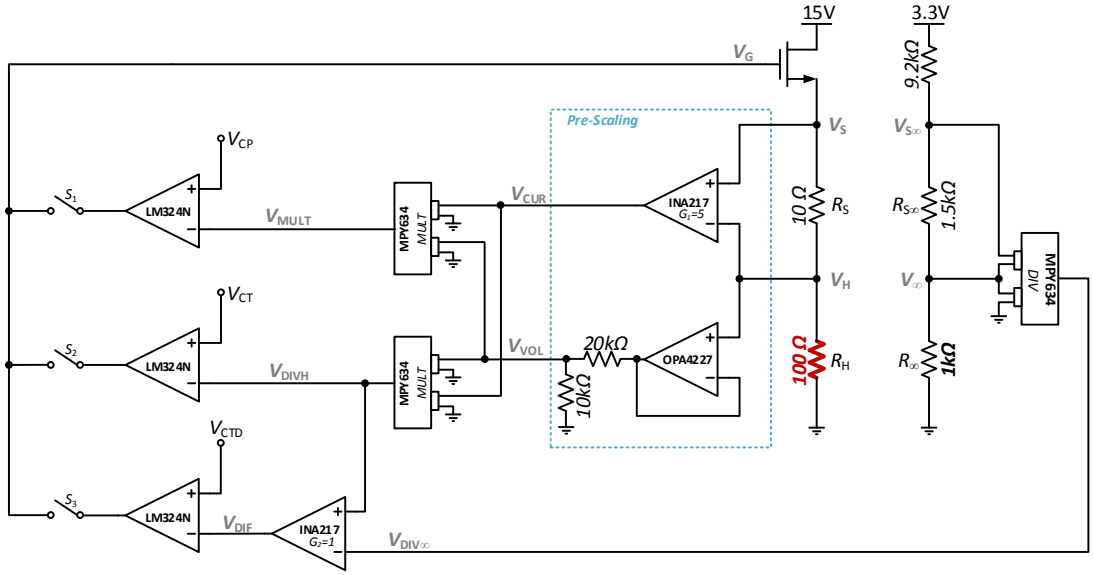

Fig. 4.14: Implementation of the multi-modal heater control topology

$$V_{DIF} = 0.02567\, T_{OVER} \tag{4.30}$$

Some of the properties of the components used are summarised in Table (4.1). In addition, the specifications of the important resistors used are shown in Table (4.2).

TABLE 4.1: Important electrical specifications of the off-the-shelf components used

		OPA4227	LM324N	MPY634	INA217
Open-loop Gain	(dB)	160	100	85	-
Input Impedance	(MΩ||pF)	10^3||3		10||-	60||2
Bias Current	(nA)	5	40	800	2000
CMRR	(dB)	138	85	80	80 (G=1)
Supply	(V)	±15	±15	±15	±15
Input Voltage Swing	(V)	±13	±15	±12	±12
Output Voltage Swing	(V)	±13	±13	±12	±12

TABLE 4.2: Information and characteristics of the resistors used

		R_G	R_S	R_D	R_H	R_∞	$R_{S\infty}$
Manufacturer		TT Electr.	Vishay	TE Conn.	IST	IST	TT Elect.
Type		SMD	SMD	SMD	SMD	SMD	SMD
Size		0805	2412	0805	0805	1206	0805
Tolerance	(%)	0.1	0.1	0.01	-	-	0.1
TCR	(ppm/°C)	5	2	2	3850	3850	5
Value	(Ohms)	1.5k + 1k	10	10k	100	1000	1500

Note that dual power supply ±15V has been used for the integrated components

mentioned above. To suppress parasitic coupling and noise coming from the supply, decoupling capacitors have been mounted as close as possible to the supply pins of each IC. Otherwise, overshoot, instability or ringing might occur due to improper by-passing. The 3.3V has been created from the +15V using a voltage regulator on the PCB.

All the components have been mounted on one side of the PCB, and most of the traces were tried to fit on the same side of the PCB. The other side was mainly used as an analog ground plane to establish the same ground voltage for all the ground terminals of the ICs, and to reduce crosstalk among traces. Since the current from the heater might be significant, a separate trace connects the lower end of the R_H with the analog ground at the point where the ground cable from the power supply connects on the PCB.

Fig. 4.14 depicts the proposed multi-modal heater control topology, which consists of all the three different control circuits presented before. Switches $S1$, $S2$, and $S3$, define which mode among CP, CT, and CTD, will be in operation. Analog switches (MAX14757), and manual switches have been used during the experiments. To create a smart flow sensor, the analog switches can be operated by an MCU, enabling the automatic toggling among the modes according to user's criteria defined within the code. The proposed novel smart flow sensor operates in CTD mode for low flows, and in CP for high flows. Under any mode during the sensor's operation, the power at the heater, P, and the overtemperature, T_{OVER}, are continuously monitored through V_{MULT} and V_{DIF}, respectively. If the power reaches the maximum power set during CTD, the state of the switches will change, activating the CP mode. Similarly, if the overtemperature reaches the maximum overtemperature set during CP the switches will swap and activate the CTD mode. Note that for the power to increase substantially during the CTD, the fluid's velocity should be relatively high, whereas for increased T_{OVER} to happen during CP, the fluid's velocity should be relative low. Hence, if the set thresholds are not extreme, it is not practically possible for a situation where P and T_{OVER} are simultaneously higher than their set values.

4.3 DISCUSSION

Newly introduced heater control circuit designs for thermal flow sensors were presented. Each topology is designed for one of the most common modes of operation for the calorimetric and hot wire thermal flow sensors, CP, CT, and CTD. Those designs were made in order to address some of the most common issues presented in the literature in terms of accuracy and repeatability, by better complying with King's law (equation (4.1)) and avoiding common Wheatstone bridge's issues such as the self-heating of R_{∞}. Apart from that, the proposed designs brought some extras benefits such as flexibility on the reference value, since it can change even on the fly by modifying the V_{CP}, V_{CT}, and V_{CTD} for the respective mode. The fundamental component of those designs is the analog multiplier/divider.

Apart from the principle of their operation, the actual implementation on PCB has been described, providing all the components' names and their necessary details to make the circuits work. The reasoning behind the chosen circuits and components has been also explained.

The intention is to create a smart flow sensor that can operate in more than one mode in order to overcome the challenges set by the modes and cannon be resolved by the heater control circuit; mainly, high temperature at low flow rates for CP, low sensitivity and increased power consumption at high flow rates for CT and CTD. Therefore, a topology that combines all the individual heater control circuits has been presented and a way toggle among them has been described.

4.4 CONCLUSION

In this chapter, novel heater novel control topologies toward biomedically and industrially safer thermal flow sensors, have been presented. From the analysis presented in this chapter, one might conclude that:

- There are ways to improve the accuracy of the existing thermal flow sensors using analog multiplier/dividers in their heater control circuits. The actual implementation has been described in this chapter.

- Multi-modal thermal flow sensors is the way forward in order to address the issues of each mode that individual heater control circuits cannot resolve. CTD for low flow rates, and CP for high flow rates is suggested in this chapter, however, CT can be also used.

5

MULTI-MODAL CALORIMETRIC THERMAL FLOW SENSOR'S MEASUREMENT PERFORMANCE

The previous chapter described the motivation, the principle of operation, and the implementation of new heater control circuits for the CP, CT, and CTD modes, and a hybrid multi-modal topology capable to toggle among them. This chapter presents how the proposed multi-modal calorimetric flow sensor has been set up and experimentally tested. The following sections present the operation of the sensor in CP and CTD modes, its accuracy, and its capability to maintain a constant power consumption at heater, and a constant overtemperature, respectively, towards a multi-modal operation. In addition, the flow sensor has been evaluated for asymmetrically located temperature sensors in order to improve the flow sensor's sensitivity and measurement range, as discussed in chapter 3.

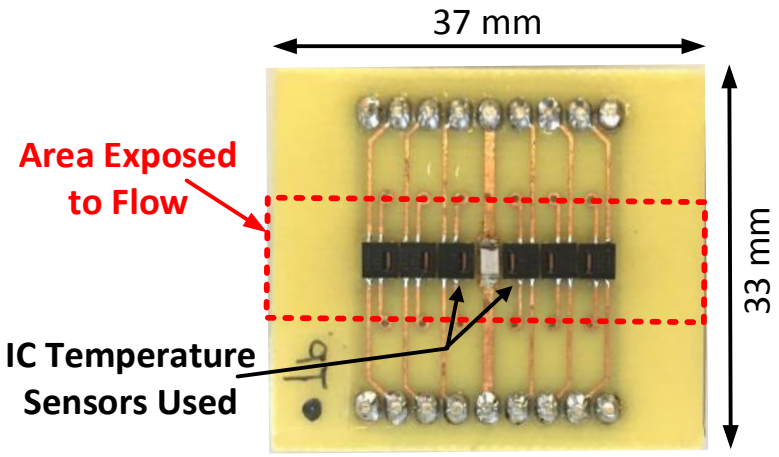

Fig. 5.1: A photo of the sensor board. Its components and the area exposed to the flow are also shown.

TABLE 5.1: Components' dimensions of the sensor board

		Heater	Temperature Sensor
Length	(mm)	2.00	3.00
Width	(mm)	1.25	3.00
Height	(mm)	0.45	1.10

5.1 EXPERIMENTAL SETUP

5.1.1 Sensor Board

A sensor board has been made to create the calorimetric thermal flow sensor transducer. It is a 0.8 mm thick FR4 printed circuit board, with the same length and width with the transducer presented in chapter 3. In a similar way, the heater has been placed in the centre of the board, and three pairs of digital temperature sensors have been symmetrically placed next to it; one of each pair at the upstream, one at the downstream. By design, the distances between the edge of the heater and the edge of the temperature sensors (TS) are 0.425 mm, 3.625 mm, and 6.825 mm. Note that the tracks of the board have been placed symmetrically to the central point of the board (where the heater is placed) in order to suppress any possible effect of the metal tracks on the thermal distribution on the board. The temperature sensors are the same digital IC temperature sensors used for previous experiments, the STS21 from Sensirion.

As previously explained, the use of discrete digital temperature sensors has its advantage, such as easy, quick, and inexpensive implementation. However, there are some drawbacks such as the greater transducer's area, and greater power consumption for the same sensitivity, as described in section 2.5. Nevertheless, the focus of this work is the evaluation of the newly introduced heater control circuits and the benefits of using of multiple operating modes, hence, the use of discrete components as temperature sensing elements is a sensible choice. The heater is the Platinum RTD sensor of 100Ω from IST that described in chapter 4.

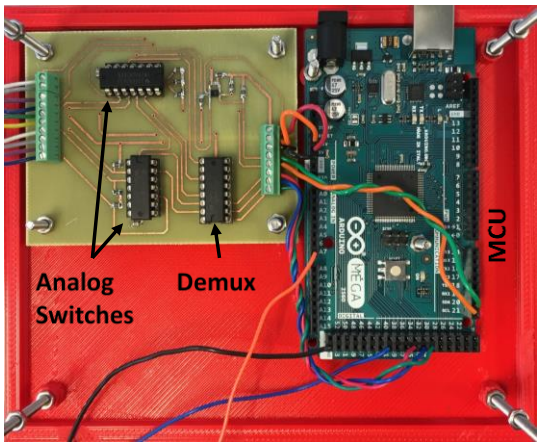

Fig. 5.2: The MCU Arduino Mega used for the acquisition of the temperature measurements. The board next to it contains the necessary circuitry to facilitate this task.

5.1.2 Flow Measurement Circuit

To acquire the measurements from the digital temperature sensors an Arduino Mega micro-controller (MCU) with the use of a demultiplexer and analog switches are utilised, similar to a previous chapter. A new PCB has been designed since the one presented in chapter 3 can be directly mounted on the housing box while carrying other discrete components which are not needed for the current experiments. The new all-digital PCB with the Arduino connected are shown in Fig. 5.2. Similar to the procedure described in chapter 3, the MCU asks simultaneously all the temperature sensors to acquire a measurement and store it within each chip. Then, the MCU asks each temperature sensor sequentially to provide its stored value, and those values are transmitted to the PC. This process consists a full cycle and it takes approximately 200

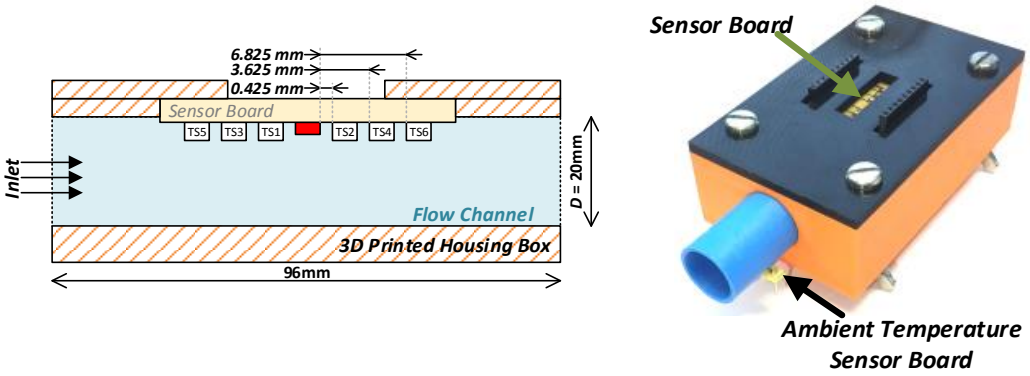

Fig. 5.3: At the left, a drawing depicting the cross-sectional view of the sensor board's housing box with the sensor board. The names of the temperature sensors (TS) are shown and distances between the components are mentioned. At the right, a photo of the housing box with the sensor board and the ambient temperature sensor board also shown.

ms, hence, the sampling frequency of the MCU is approximately 5Hz. Note that the MCU and the digital PCB are mounted on a plastic base. This base is 3D printed and its purpose is to accommodate all the PCBs (including the heater control system PCB) and the MCU in a stack, ensuring mechanically stable connections among them, and facilitating the transportation of the setup.

5.1.3 Experimental Structure

The sensor board is then enclosed in the 3D printed housing box (Fig. 5.3), where only the area of the heater and the digital temperature sensors is exposed to the flow (Fig. 5.1). With the use of the board connector and a ribbon cable, the connection between the sensor board and the stack of PCBs is established. The ambient temperature sensor board is mounted at the upstream orifice, as Fig. 5.3 depicts. Note that the ambient temperature sensor is mounted diametrically opposite to the sensor board and at a horizontal distance of about 6 cm, to eliminate any effect of the heater to the ambient temperature sensor measurements. In addition, the fact that the ambient temperature sensor is on a different board from that of the heater contributes significantly to the thermal isolation between R_H and R_∞.

The housing box is then mounted at the end point of our experimental pipe line. Placed in series and before the housing box, there is the commercially available flow sensor from OMRON (D6F-50A6-00) that can be used as a reference. At the inlet of

this structure, the mass flow controller (MFC) from Bronkhorst (F-201AV) is connected to control the flow. The MFC used for this work can create flows in the range of 0 to 50 standard litres per minute (slm) with a resolution of 0.1 slm. The inlet of the MFC is connected to the gas supply through a pressure gauge that maintains the pressure at ~3 bar. For the purpose of the experiment it is important that the pressure at the inlet of the MFC is stable ensure accuracy and reproducibility of the generated flow patterns. The fluid used for all of the experiments is air. Fig. 5.4 depicts the experimental setup.

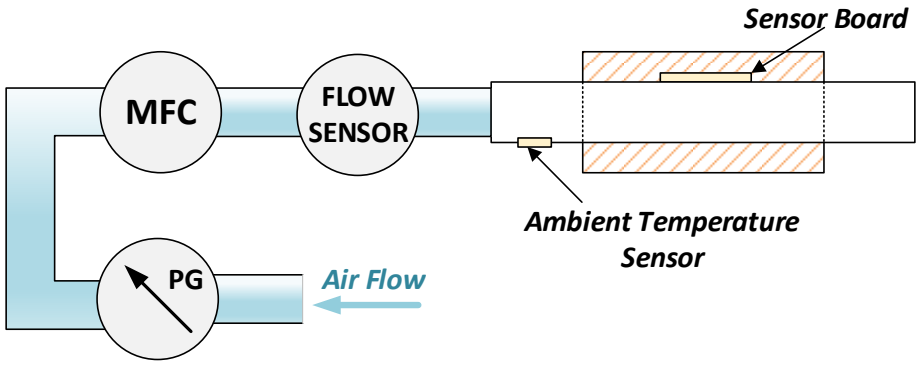

Fig. 5.4: A cross-sectional drawing of the system's setup. "PG" is the pressure gauge dropping the pressure at 3 bar, and "FLOW SENSOR" is the commercial flow sensor from OMRON. Note that the ambient temperature sensor is placed diametrically opposite to the sensor board at the upstream.

5.1.4 Software Development for Control and Monitoring

A DAQ from National Instruments (NI USB-6343) is used for the experiments. The purpose of the DAQ is three-fold:

- To collect the digital temperature measurements from the sensor board, hence, to acquire the flow measurements.
- Allow a user to set custom values for heater's power P at CP, overtemperature T_{OVER} at CTD, and heater's temperature T_H at CT.
- To monitor and dynamically adjust the heater control system.

Therefore, an interactive user interface (UI) has been developed using LabVIEW from National Instruments. During operation, the UI shows the voltage at any node of the heater control circuit. Also, it depicts each of the most important values, the power

at the heater P, the heater's temperature T_H, and the overtemperature T_{OVER}, and their corresponding voltages V_{MULT}, V_{DIVH}, and V_{DIF}, respectively, in the form of a graph plot. Both, V_{DIVH} and $V_{DIV\infty}$, are also calculated and displayed in Volts, sensor's resistance in Ohms, and Temperature in ^oC. For the different modes, the user defines the required power directly in W, or the required temperature in ^oC. The software will calculate the necessary voltage and it will create and implement the corresponding reference voltage. The DAQ features a 16-bit Digital-to-Analog Converter (DAC), hence, for the output voltage range of ±10 V, the minimum voltage increment is approximately 0.3 mV. This voltage increment can be translated into 0.18 mW minimum power step for the CP, and 0.12 ^oC minimum overtemperature step for the CTD. The voltage of the critical nodes can be continuously recorded and stored in a spreadsheet. A screenshot of the software during operation is shown in Fig. 5.6.

Fig. 5.5 is a photograph of the setup for the evaluation of the flow sensor and the operation of the heater control circuitry.

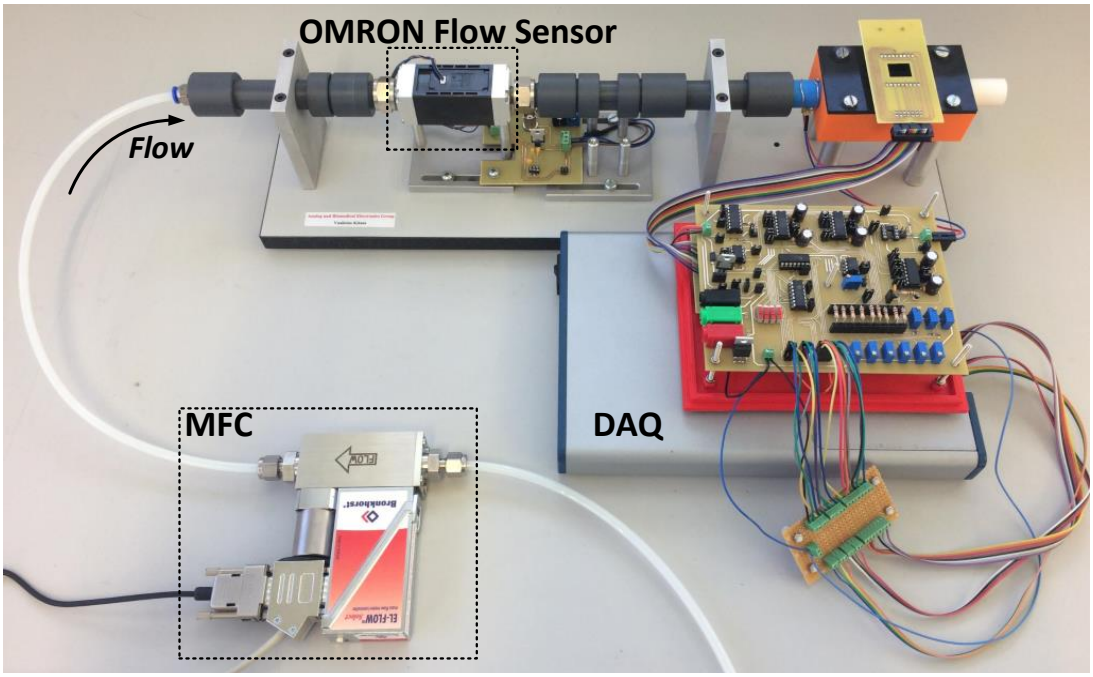

Fig. 5.5: A photograph of the setup

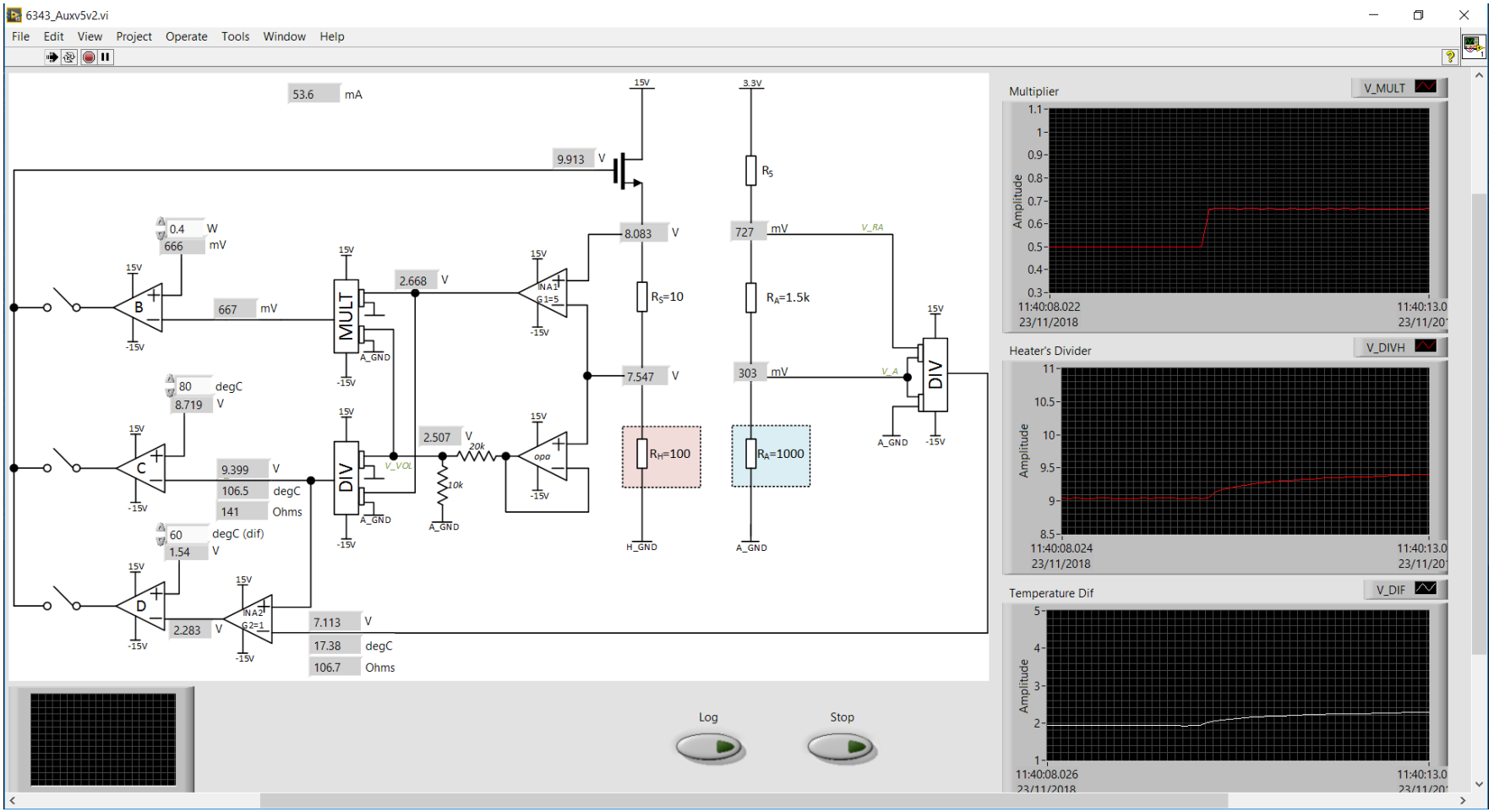

Fig. 5.6: A screenshot of the UI used for control and monitoring. B, C, and D, are the error amplifiers for CP, CT, and CTD mode, respectively. The user can define the Wattage, Temperature, or Temperature Difference for the respective mode in the white box next their positive input. Note that the voltages of all the nodes are displayed, and the output of the multiplier, the heater's divider and the temperature difference are plotted.

5.2 EXPERIMENTAL MEASUREMENTS

This section presents the measurements acquired for the different experiments. Our setup has been tested for the CP mode at heater's power ratings of 300, 350, 400 mW, and for CTD mode at overtemperatures of 75, 80, and 85 ^{o}C. CT control topology is a subsystem of the CTD control topology, therefore, the proper operation of the CTD circuit requires the proper operation of the CT topology. Therefore, separate testing of the CT mode is not necessary. In addition, CT mode testing would require a more elaborate experimental setup where the fluid's temperature can be controlled in order to reproduce the measurements.

The system has been tested for discrete flow values from 0 to 50 litres per minute. With the MFC programmed accordingly, the flow remained constant at each flow value for 3 minutes to ensure system's stability. The last 250 measurements (equivalent to approximately the last 50 sec) for each flow value have been taken into account. The maximum and minimum values measured, as well as, the calculated average and standard deviation, are presented. No filtering has been applied to the data presented below.

Section 5.2 is mainly divided into two parts: the first part presents results using symmetrical to the heater temperature sensors, whereas the second part is asymmetrical located temperature sensing elements, as in chapter 3.

5.2.1 Symmetrical Measurements

This paragraph presents the results using the symmetrical pair that is closest to the heater, TS1 and TS2.

5.2.1.1 Constant Power (CP) Mode

To begin with, the next figure shows the output of the flow sensor, ΔT, for the three different values of the constant power, 300, 350, and 400 mW. At zero flow, the average heater temperature measured during the experiments, was 95.64, 109.82, and 120.77 ^{o}C, respectively. It is apparent that temperatures at heater for CP mode can rise substantially, being potentially dangerous for temperature sensitive applications such

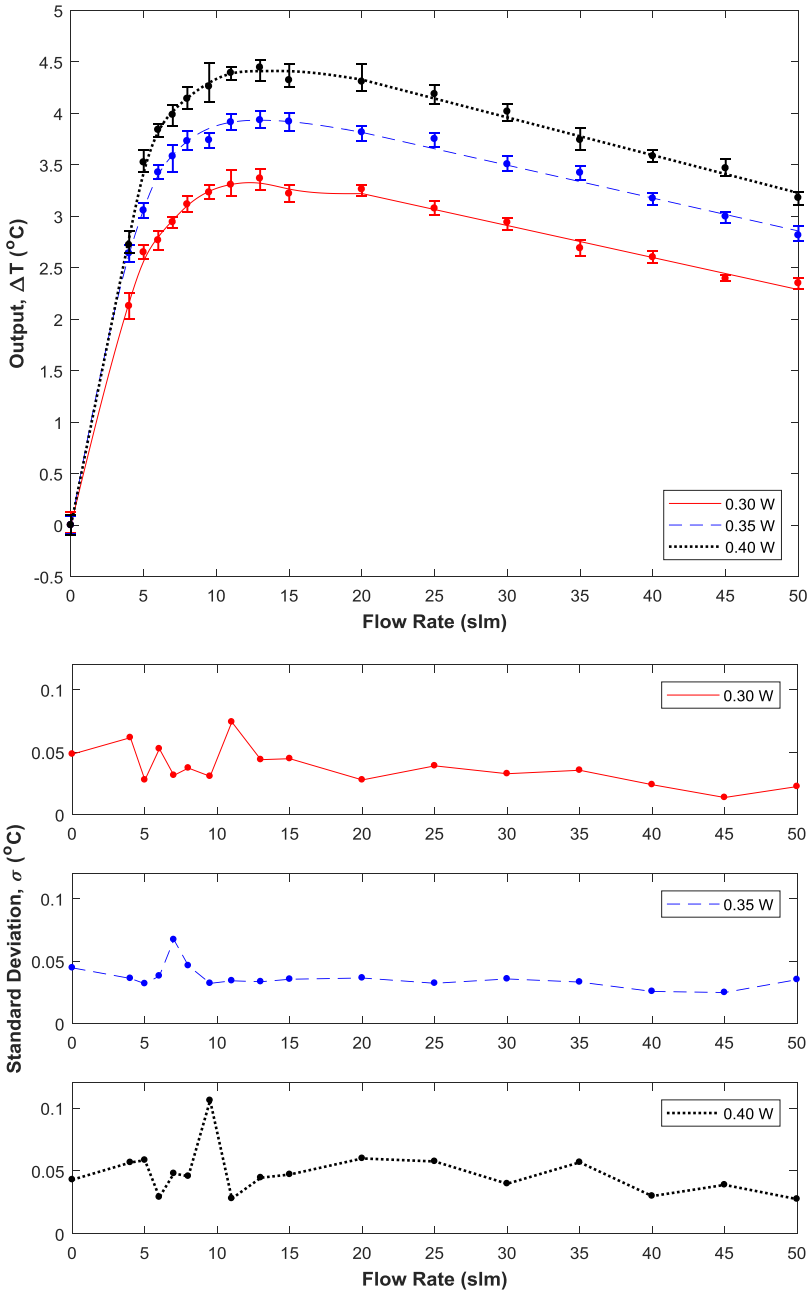

Fig. 5.7: At the top, the output of the flow sensor as a temperature difference of the temperature sensors TS1 and TS2 in CP mode, for different values of power at heater. The errorbars show the maximum and the minimum value measured. At the bottom, the standard deviation of the measurements for each power at heater.

as those in biomedical field. Nevertheless, notice that is below 150 ^{o}C, which is the maximum allowed by the manufacturer.

The dot points in the top graph of Fig. 5.7 represent the mean values out of the 250 measured for each flow. The errorbars that extend from each mean value indicate the absolute maximum and the absolute minimum value measured for each flow rate

value, demonstrating the whole range of values acquired during the experiment. To better depict the distribution of the measurements for each flow value, the graphs below show their standard deviation for each measurement. A fitting line based on the data has been also created to clearly demonstrate the flow sensor's output performance. Unless otherwise stated, the mean value at zero flow has been removed as an offset for each experiment. The origin of this offset has been discussed in chapter 3.

As expected in CP mode, the output increases quickly for low flow rates until it reaches its maximum, also known as turn-over flow rate, Q_{TO}. The turn-over flow rates have been calculated and presented in Table 5.2. Then, it slowly reduces, almost linearly. Qualitatively, that is a rather typical output of a calorimetric flow sensor in CP mode, as discussed in chapters 2 and 3, validating that this setup using off-the-shelf discrete components can operate as such. In addition, as one can notice, the output value increases for a certain flow value, as the power at the heater increases.

The standard deviation (σ) is fairly consistent across the entire range except for the points which occur near the turning point. The value of the σ is approximately 0.04 ^{o}C for all the different power ratings. Note that, as in every electronic circuit, the temperature readings from the commercial SMD temperature sensors incorporate noise, contributing to the measurement deviation noticed above. Another source of noise are flow fluctuations in microscopic level that, in turn, affect the amount of heat delivered to the temperature sensors. Hence, the true temperature at the temperature sensing element might fluctuate even if all the rest of variables are constant. Nevertheless, using the standard deviation presented above, the relative measurement error is less than 2.6% for flow rates below 15 litres per minute, while it reduces within the range of 0.52~1.2% for flow rates higher than 15 litres per minute. Those relative error values are comparable to those presented in the literature for micro-machined, integrated flow sensors [41].

Fig. 5.8 depicts the V_{DIF} and the V_{MULT} and their standard deviation. It is demonstrated that my control system is capable to keep the power at the heater constant under all the tested flow conditions and heater's resistance values (Fig. 5.9). Specifically, the relative error for the V_{MULT} is 0.17, 0.15, and 0.13% for P equal to 0.30, 0.35, and 0.40W, respectively, based on the data presented above.

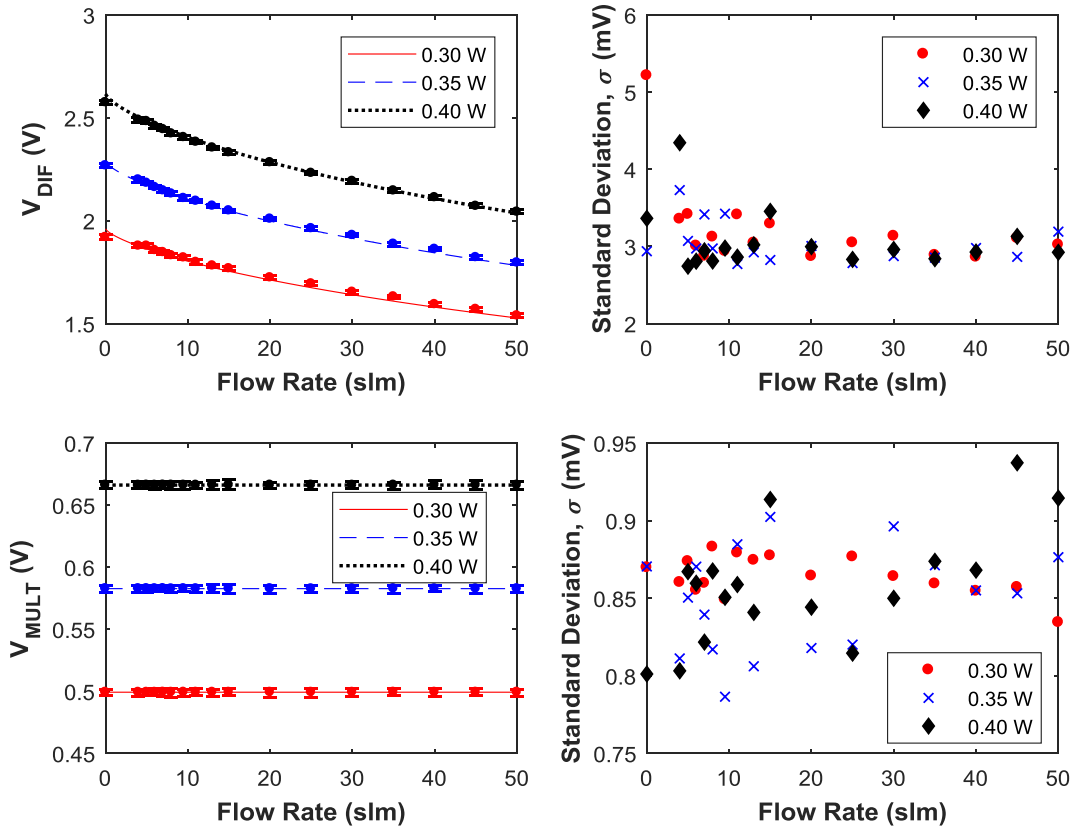

Fig. 5.8: At the top row, the voltage V_{DIF} as measured representing the temperature difference between heater and ambient in CP mode for different values of power at heater, and the standard deviation of the measurements. At the bottom row, the voltage V_{MULT} as measured representing the power delivered at the heater, and the standard deviation of the measurements. The lines in the left column are derived by the data and King's law.

V_{DIF} decreases as the flow rate increases, according to King's law. Based on the data presented in Fig. 5.8 and 5.11, the equation for my flow sensor describing the correlation among, V_{MULT}, V_{DIF}, and Flow Rate (Q), has been derived. Considering King's law as:

$$\frac{V_{\mathrm{MULT}}}{V_{\mathrm{DIF}}} = A + BQ^n \tag{5.1}$$

and my measurements, one can conclude that $A = 0.2547$, $B = 0.004125$, and $n = 0.732$, hence, the above equation can be re-written as:

$$\frac{V_{\mathrm{MULT}}}{V_{\mathrm{DIF}}} = 0.2547 + 0.004125\, Q^{0.732} \tag{5.2}$$

Note that all the lines (continuous, dashed, and dotted) in Fig. 5.8 and 5.11 represent the King's law as presented in equation (5.2). In turn, this equation can be used to

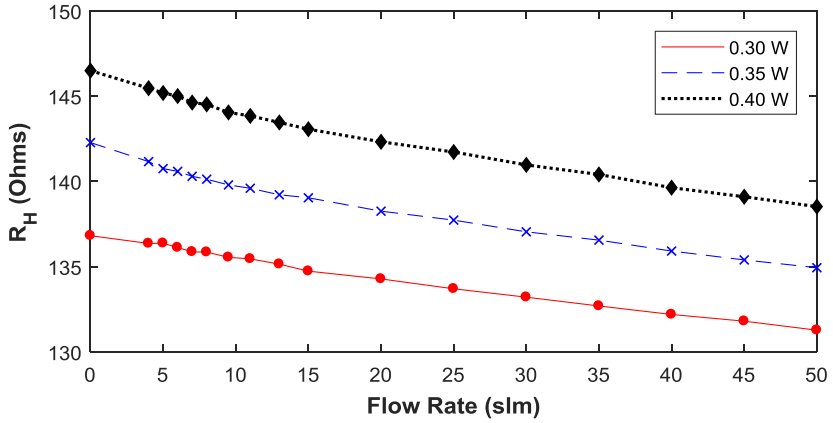

Fig. 5.9: Heater's resistance, R_H, in CP mode

predict the power and overtemperature for this flow sensor, for any other possible setup in CP or CTD that is not presented here.

TABLE 5.2: Turn-over flow rate for the six experiments undertaken

	Experiment	Q_{TO} (slm)
CP	**0.30 W**	12.4
	0.35 W	13.0
	0.40 W	14.2
CTD	**75 ºC**	18.4
	80 ºC	18.8
	85 ºC	19.0

5.2.1.2 Constant Temperature Difference (CTD) Mode

Similarly to CP mode, the setup has been tested for the CTD mode, and overtemperatures of 75, 80, and 85ºC. Although, the heater's power at no flow is approximately 290, 315, and 337 mW, respectively, at the maximum flow rate tested (50 litres per minute), the power reached the 380, 405, and 432 mW, respectively. Therefore, one can say that CTD mode can challenge the portability capability of the flow sensor.

Fig. 5.10 presents the output of the flow sensor and the standard deviation of the measurements, in a similar format to that used for the CP mode in Fig. 5.7. The output of the flow sensor for the CTD is qualitatively similar to that of the CP mode, where it quickly increases for low flow rates until it reaches a turn-over flow rate, and

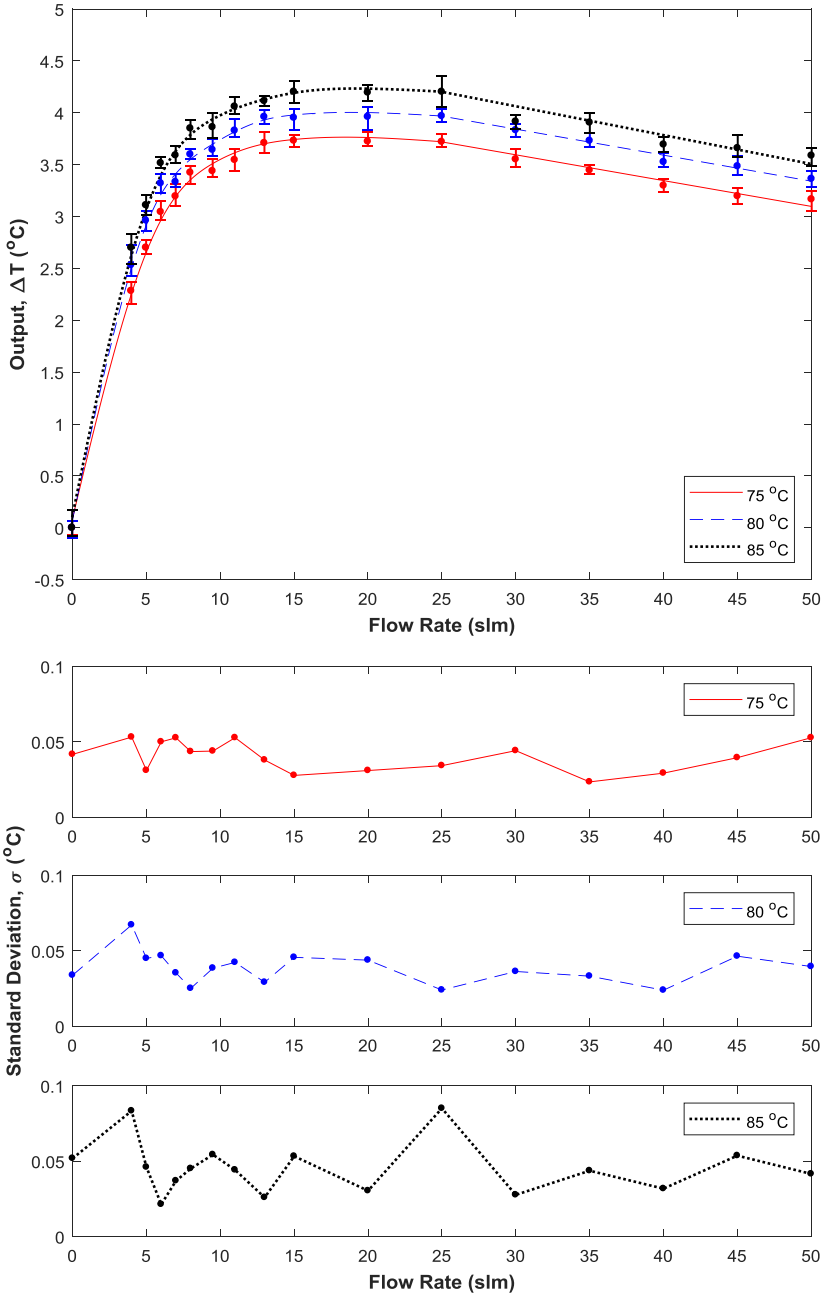

Fig. 5.10: At the top, the output of the flow sensor as a temperature difference of the temperature sensors TS1 and TS2 in CTD mode, for different values of overtemperature. The errorbars show the maximum and the minimum value measured. At the bottom, the standard deviation of the measurements for each overtemperature.

eventually starts decreasing. However, the CTD outputs seems to have a wider flow rate range of saturation around the turn-over flow rate. This can be a drawback of the mode if one wants to measure flow rates in both parts, before and after the turn-over point, since the sensitivity of the flow sensor is minimum for a considerable range of flow rates. On the other hand, the turn-over flow rate for the CTD experiments is higher than that of the CP mode, as presented in Table 5.2. Thus, the measurement

range of the flow sensor is greater in the CTD than in CP mode, if only the part from zero to turn-over flow rate is about to be used. Such a preference is popular in literature, as mentioned in previous chapters. Also note that as the power at heater increases for a certain mode, either CP or CTD, the turn-over flow rate increases, too. Hence, one can increase the measurement range of flow rates by increasing the power consumption, when the part 0~Q_{TO} is only used.

TABLE 5.3: Measured values for $Q < Q_{TO}$*

		S** (°C slm^{-1})	***P*** (mW)	T_{OVER} (°C)
CP	**0.30 W**	0.5299	300	75.76 ~ 69.28
	0.35 W	0.6113	350	88.33 ~ 80.59
	0.40 W	0.7046	400	100.28 ~ 91.56
CTD	**75 °C**	0.5400	289.5 ~ 334.1	75
	80 °C	0.5923	315.3 ~ 357.1	80
	85 °C	0.6218	336.8 ~ 379.7	85

Q_{TO}*: turn-over flow rate
*S***: maximum output sensitivity

TABLE 5.4: Measured values for $Q > Q_{TO}$

		S |°C slm^{-1}|	***P*** (mW)	T_{OVER} (°C)
CP	**0.30 W**	0.0311	300	69.28 ~ 59.93
	0.35 W	0.0319	350	80.59 ~ 69.94
	0.40 W	0.0367	400	91.56 ~ 79.56
CTD	**75 °C**	0.0249	334.1 ~ 379.6	75
	80 °C	0.0251	357.1 ~ 404.9	80
	85 °C	0.0278	379.7 ~ 431.6	85

Tables 5.3 and 5.4 summarise the power ratings and the overtemperatures measured before and after the turn-over flow rate. As expected, the greater the power, the better the sensitivity for the CP mode. Similarly, the greater the overtemperature, the better the sensitivity for the CTD mode. This is applicable for both parts of the flow rate range, before and after the Q_{TO}. However, note that even though the power consumption is greater for CTD than CP in $Q>Q_{TO}$, the sensitivity is better for the

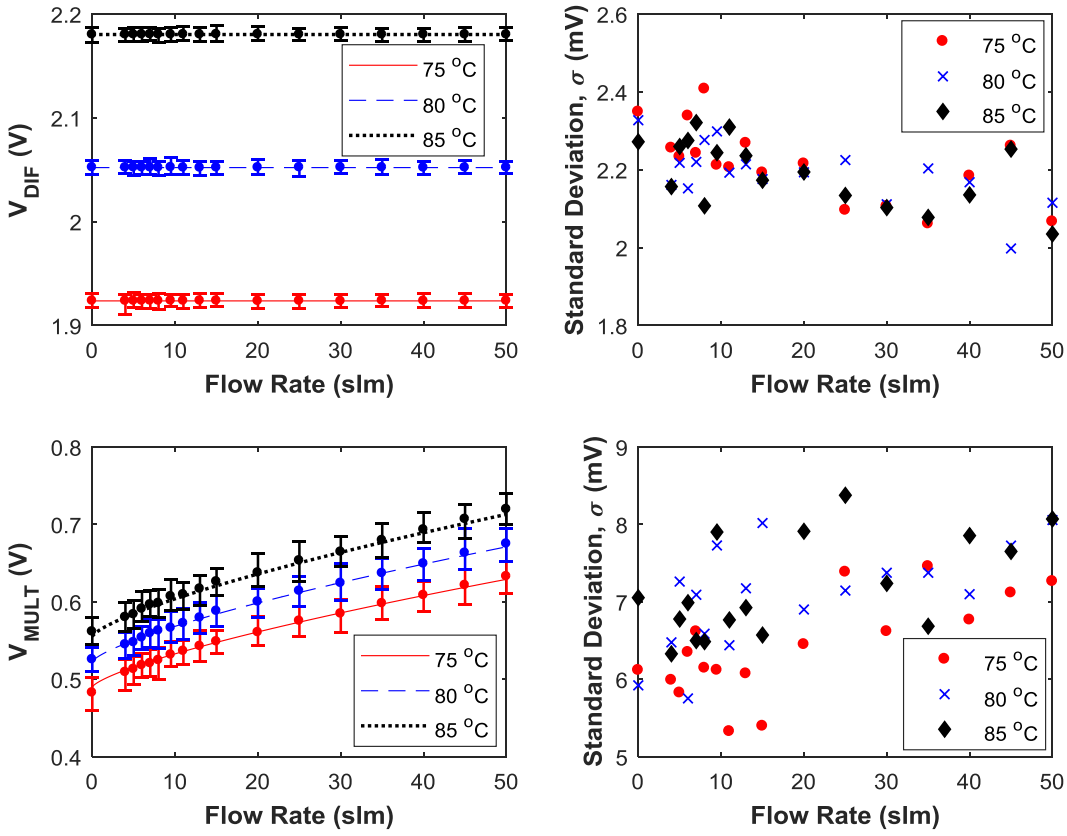

Fig. 5.11: At the top row, the voltage V_{DIF} as measured representing the temperature difference between heater and ambient in CTD mode for different values of power at heater, and the standard deviation of the measurements. At the bottom row, the voltage V_{MULT} as measured representing the power delivered at the heater, and the standard deviation of the measurements. The lines in the left column are derived by the data and King's law.

latter. In fact, the increase in power for the CTD as the flow increases, hinders the cooling down of the transducer area, thus, the output does not change substantially after reaching the saturation in turn-over flow rate. Tables 5.1, 5.2, and 5.3 clearly show the effect of power consumption on the measurement range (in case of measurements until Q_{TO}) and, on the sensitivity of the flow sensor.

Fig. 5.11 shows that the V_{DIF} and V_{MULT}, and the standard deviation of the measurements. The V_{DIF} plot clearly demonstrates that my proposed circuit is able to create a constant overtemperature under any flow and temperature conditions created during the experiments. This argument can be supported by the low variation measured and the small σ. As a matter of fact, the relative error for all the CTD test was always below 0.125%.

V_{MULT} seems to follow the King's law, as expected, and the equation (5.2). Based on the heater power measurements presented in Fig. 5.11, V_{MULT} needs to noticeably vary during a constant flow. However, the goal is to achieve a constant overtemperature, hence, fluctuations in power are not important in CTD mode as long as a stable overtemperature is achieved.

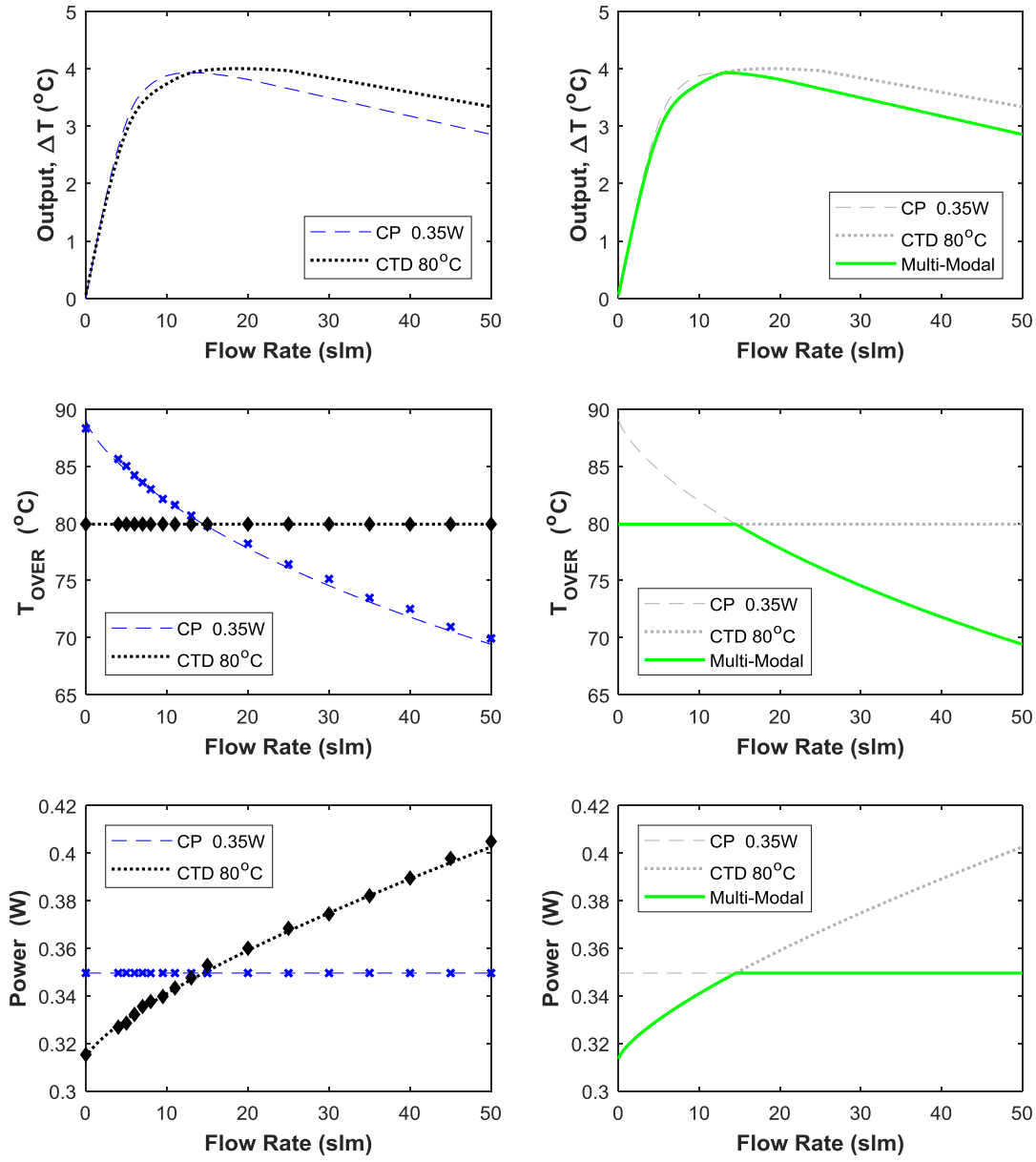

Fig. 5.12: At the left column, the output, overtemperature, and heater power for the 0.35W CP experiment, and the 80°C CTD experiment. At the right, the combined performance of a multi-modal flow sensor

5.2.1.3 Multi-Modal Results

The two previous sections, 5.2.1.1 and 5.2.1.2, demonstrated that the proposed topology is capable to operate in both, CP and CTD modes, controlling the power at heater accordingly, and producing accurate results. The goal is to create a multi-modal flow sensor, for the purpose described before, which can be only achieved by a heater control circuit that can operate in more than one mode, such as the one presented here. This section presents the outcome of using a flow sensor able to toggle between CTD and CP mode. The CTD will be used for low flows to overcome the problem of the excessive heater's temperature, and the CP for the high flows to avoid excessive power consumption and the low output sensitivity.

Fig. 5.12 presents the flow sensor's output ΔT, the overtemperature T_{OVER} in ^{o}C, and the power consumed by the heater P for the case of CTD with 80^{o}C overtemperature and the case of CP mode with 0.35 W heater power. This figure clearly illustrates the differences between the two modes, as experimentally measured and described in the previous sections. Specifically, the reduced sensitivity of the CTD compared to that of the CP is evident for high flows, although the power consumption is greater for the former. On the other hand, the overtemperature is up to 8 ^{o}C greater for the CP, representing a 10% overtemperature increase compared to CTD. That is an important difference that it must be taken account in applications where excessive heat can cause problems, such as those of biomedical purpose. In conclusion, Fig. 5.12 clearly demonstrates the necessity of a multi-modal flow sensor capable to operate in CTD for low flows, and in CP for high flow rates, to improve its performance in terms of power consumption, sensitivity, and safety.

Note in Fig. 5.12 that there is a flow rate value where the power at heater and the overtemperature is the same for both modes, hence, the output is the same. By choosing that point as the toggling point (the point where the sensor switches from CTD to CP, and vice versa), one can ensure a smooth transition from one mode to the other. That is valid since no abrupt changes in power delivered to the heater need to take place, ensuring a predictable sensor's output, in contrast to other works in the literature [64]. Since this point is common for both, it ensured that no transition time is needed, and no hysteresis will be created.

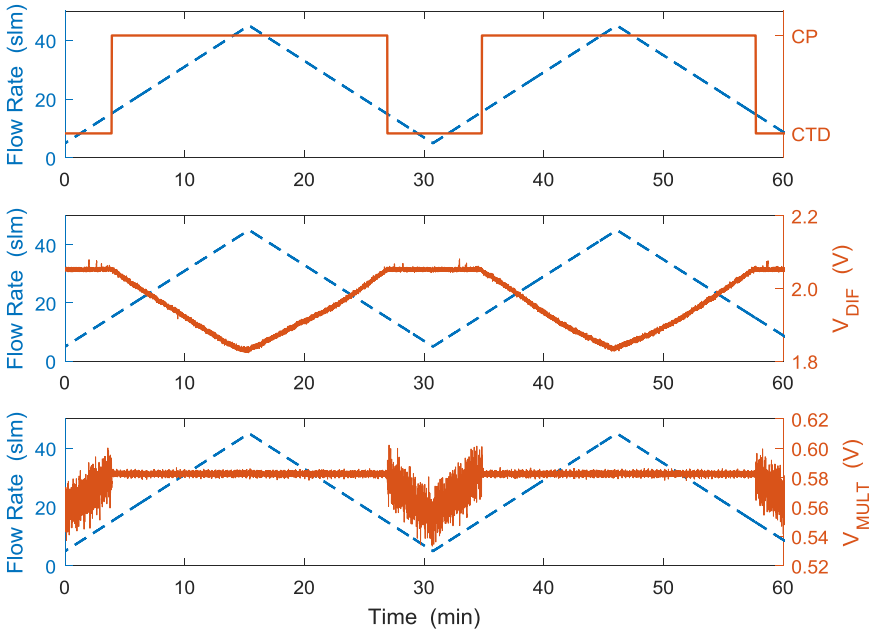

Fig. 5.13: Transient performance of the multi-modal flow sensor. The dashed line corresponds to applied flow rate as defined by the MFC. The top plot shows the operating mode of the sensor during the experiment. The second plot depicts the V_{DIF} that corresponds to the T_{OVER}, while the bottom plot shows the V_{MULT} (power at heater) for the same time period.

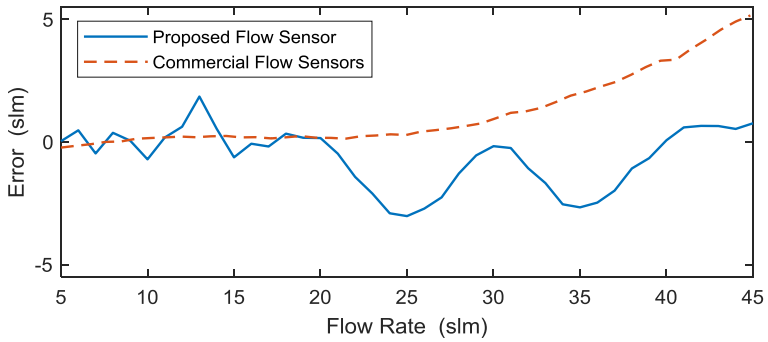

Fig. 5.14: Error as measured during the transient experiment for the proposed flow sensor and the OMRON flow sensor.

The switching can be easily implemented using analog switches, as described in chapter 4, and a simple part of programming code. For these experiments, it is the DAQ that controls which of the switches S_1 and S_3, as presented in Fig. 4.14, will be closed to set the CP or CTD mode, respectively. The default starting operating mode is the CTD since it provides better safety. The DAQ is always aware of the mode in operation. During CTD, the power at the heater, P, is continuously monitored. If P increases over 0.35W, the DAQ will automatically switch to CP mode of 0.35W. During CP, it is the T_{OVER} that is continuously monitored, and in case of a surge of

more than 85 ^{o}C, the DAQ will switch the operating mode back to CTD of 85 ^{o}C by opening and closing the appropriate switches.

Experimental evidence of the automated multi-modal operation of the proposed topology are shown in Fig. 5.13. A transient experiment where the flow gradually changes from 5 to 45 slm and back to 5 slm has been performed. The figure clearly shows that the sensor operates in one of the two distinctive operating modes: in CTD for low how flow rates by keeping the V_{DIF} constant (hence, constant T_{OVER}), or in CP by maintaining a constant V_{MULT} (thus, constant P). For this experiment, the mode toggling takes place automatically, based on the thresholds defined above.

Note in Fig. 5.12 that as the flow rate increases for the multi-modal topology, the CTD's mode output increases monotonically, whereas the CP's mode output decreases monotonically; hence, the Q_{TO} of the multi-modal sensor is the toggling point. Therefore, the measured flow rate at any point can be determined by the measured output, ΔT_M, and the mode in operation.

The green fitting line for the multi-modal sensor's output, ΔT, shown in the first row of Fig. 5.12 can be now used as the ideal output of the proposed flow sensor; hence, the accuracy of the flow sensor can be measured. In fact, the inaccuracy of the multi-modal flow sensor has been calculated during the above transient experiment and presented in Fig. 5.14. This figure provides a direct comparison between the measurement error of the proposed topology and the commercial flow sensor from OMRON. Although the measurement error for the OMRON is relatively low for low flow rates, it increases substantially as the measured flow rate rises. In fact, the error reaches more than 5 slm for an real flow rate of approximately 45 slm. On the other hand, the measurement error of the multi-modal flow sensor never exceeded the ±3 slm, even though the suggested topology has not been optimised for high accuracy but for multi-modal operation.

To sum up, this section is a direct comparison between CP and CTD modes, and it provides experimental evidence of the performance improvement by using a multi-modal flow sensor instead of a single mode one. According to the measurements of the proposed topology, one can achieve overtemperature reduction up to 9.5% by using CTD for low flows instead of CP, and heater power reduction up to 13.6% by

using CP for high flow rates instead of CTD, while improving the sensor's sensitivity at the same time. The transient performance and the automated mode switching has been also demonstrated, whereas its measurement error has been measured showing that the proposed PCB-level flow sensor can offer a similar accuracy with that of a micromachined, commercially available flow sensor.

5.2.2 Asymmetrical Measurements

The effect of asymmetrically positioned temperature sensors have been also studied during these experiments, in the same manner as that in chapter 3. The results shown below are acquired during the same experiments described in the previous sections of this chapter, by using the temperature sensing elements placed further away from the heater. The following sections demonstrate the effect at the output by using the TS closest to the heater at the downstream side (same TS used for the symmetrical measurements) and the TS away from the heater at the upstream side.

5.2.2.1 Constant Power (CP) Mode

Fig. 5.15 depicts the flow sensors output in CP mode for 0.35 W using the pairs TS2–TS3 (or TS23) and TS2–TS5 (or TS25) in comparison with the symmetrical pair TS2–TS1 (or TS21), where TS5 is the one further away from the heater, as shown in Fig. 5.3. Note that it is expected that the asymmetrical topology to have a great offset since the temperature sensors are not at the same distance from the heater. That offset measured at zero flow is removed from the results shown here to facilitate the comparison among the different outputs.

According to Fig. 5.15, sensitivity of the flow sensor deteriorates for flow rates lower than the turn-over flow rate, while the turn-over flow rate decreases. Therefore, asymmetrical topology in flow range of 0~Q_{TO} in CP does not offer any benefit compared to the symmetrical, since both, sensitivity and measurement range, decrease for the same heater's power. However, it is evident that the flow sensor's sensitivity after the Q_{TO} increases substantially as the upstream temperature sensor moves away from the heater. Specifically, the absolute value of the gradient for high flows is 0.0319, 0.0842, and 0.1189 for the pairs TS21, TS23, and TS25, respectively. That means that one can get up to 272% increase at the sensitivity of the sensor for high

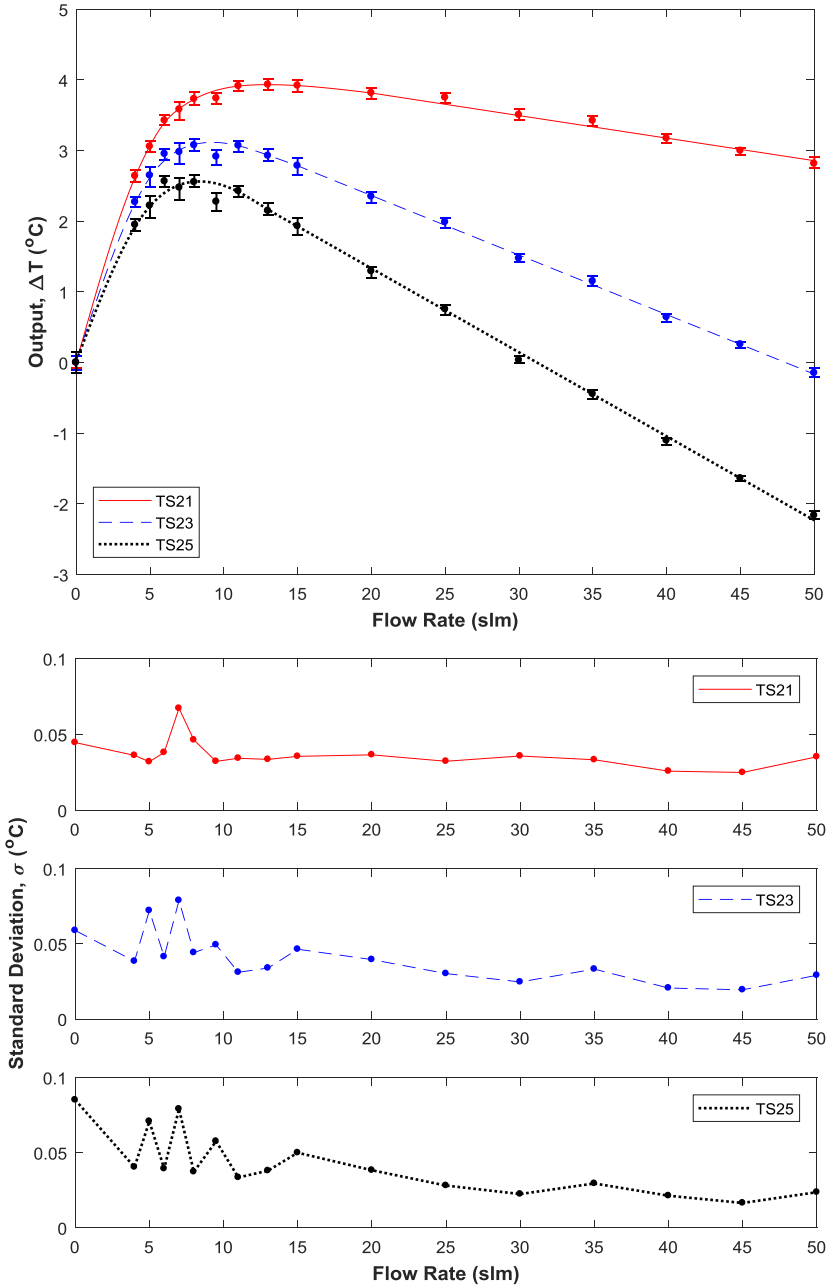

Fig. 5.15: Flow sensor's output for different pairs of temperature sensors for 0.35 W in CP mode. TS21 symmetrical pair, TS23 the first asymmetrical, and TS25 the second asymmetrical with the greatest asymmetry. The standard deviation of the measurements follows.

flows, without any change in heater's power consumption, simply by placing the temperature sensing elements asymmetrically. That is a vast improvement in flow sensor's performance, hence, asymmetrically placed temperature sensors should be taken into consideration for the design of flow sensors for high flows.

The reproducibility and accuracy of proposed flow sensor's design is confirmed by the low standard deviation presented in Fig. 5.15. As in the symmetrical topology

discussed before, the σ seems relatively stable at 0.04 ºC, apart from variance in the area of the turn-over flow rate.

TABLE 5.5: Turn-over flow rate for asymmetrical pairs

	Pair	Q_{TO} (slm)
CP (P=0.35W)	**TS21**	13.0
	TS23	9.2
	TS25	8.4
CTD (T_{OVER}=80ºC)	**TS21**	18.8
	TS23	15.4
	TS25	10.2

TABLE 5.6: Output sensitivity for asymmetrical pairs and $Q>Q_{TO}$

	Pair	***S*** |ºC slm^{-1}|
CP (P=0.35W)	**TS21**	0.0319
	TS23	0.0842
	TS25	0.1189
CTD (T_{OVER}=80ºC)	**TS21**	0.0251
	TS23	0.0441
	TS25	0.0661

5.2.2.2 Constant Temperature Difference (CTD) Mode

Fig. 5.16 depicts the output of the same pairs (TS21, TS23, TS25), but for the CTD mode of 80ºC overtemperature. Similarly to the CP mode, the turn-over flow rate moves to a lower value whereas the sensitivity after Q_{TO} increases, as the asymmetry becomes greater. At low flows, however, there is not important difference in sensitivity among the topologies, hence, there is not any significant benefit using asymmetrically located temperature sensors. Nevertheless, the gradient for the high flow is 0.0251, 0.0441, and 0.0661 for the pairs TS21, TS23, and TS25, respectively. Although sensitivity for $Q>Q_{TO}$ is improved for asymmetrical topologies, those values

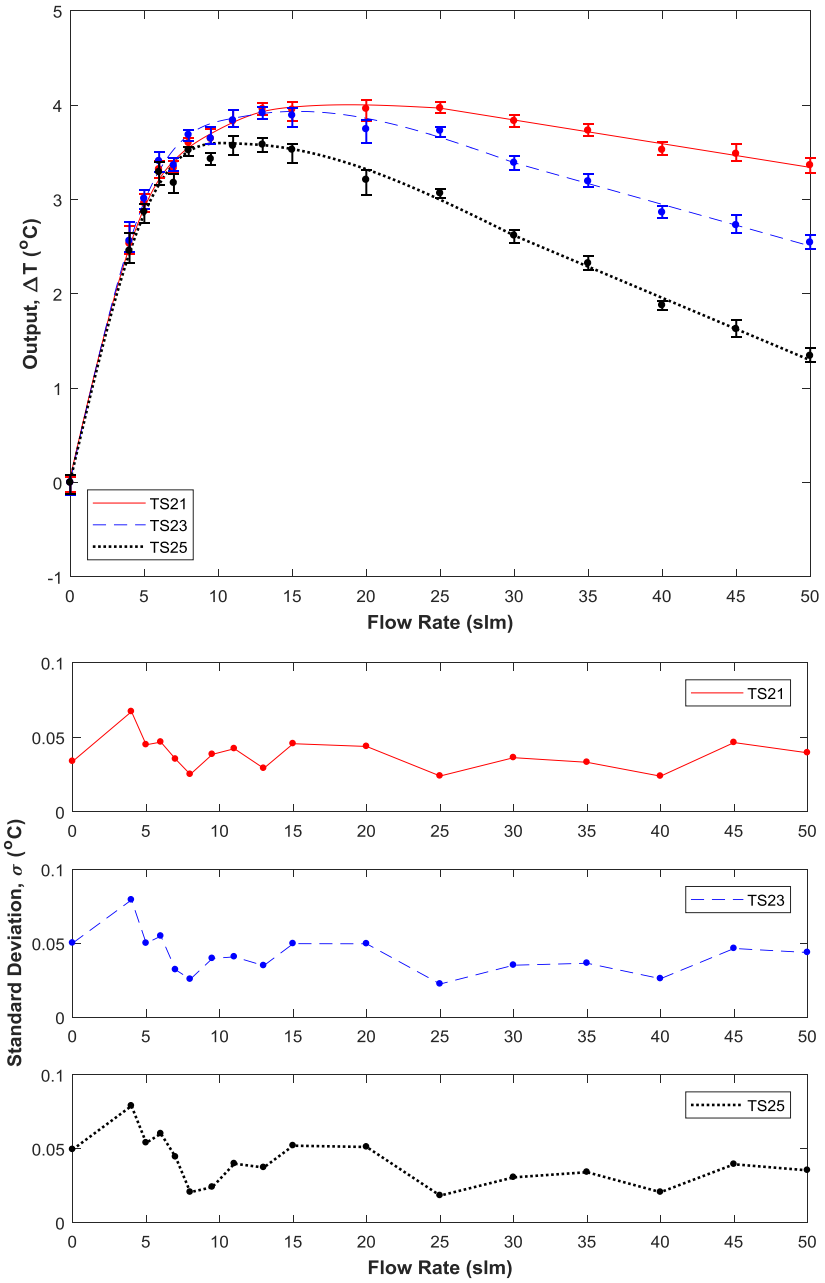

Fig. 5.16: Flow sensor's output for different pairs of temperature sensors for 80ºC in CTD mode. TS21 symmetrical pair, TS23 the first asymmetrical, and TS25 the second asymmetrical with the greatest asymmetry. The standard deviation of the measurements follows.

are considerably smaller compared to those of the CP mode. In fact, the sensitivity of the CP mode in high flow rates using the same asymmetric pair is up to 79.9% larger. Thus, it is proved that CP offers greater performance, in terms of sensitivity and power consumption, than the CTD, for flows after the Q_{TO}, confirming that CP should be the mode of choice for high flows, either for symmetrically or asymmetrically located temperature sensors. Table 5.6 summarises the sensitivities measured for the pairs tested for both, CP and CTD, modes.

5.2.2.3 Multi-Modal Results

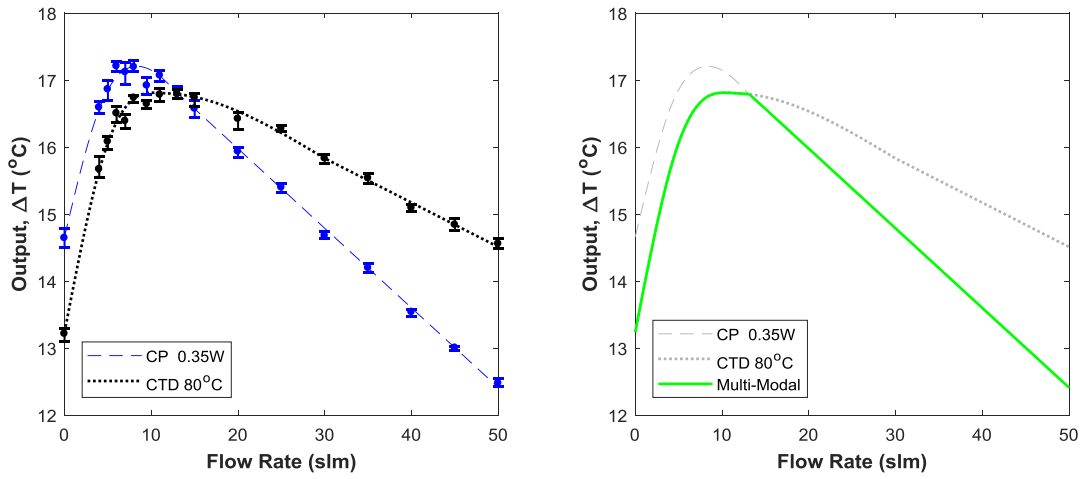

Fig. 5.17: At the left, the output of the flow sensor for the pair TS25 in CP mode for 0.35 W, and in CTD mode for 80ºC. At the right, the results of a multi-modal flow sensor.

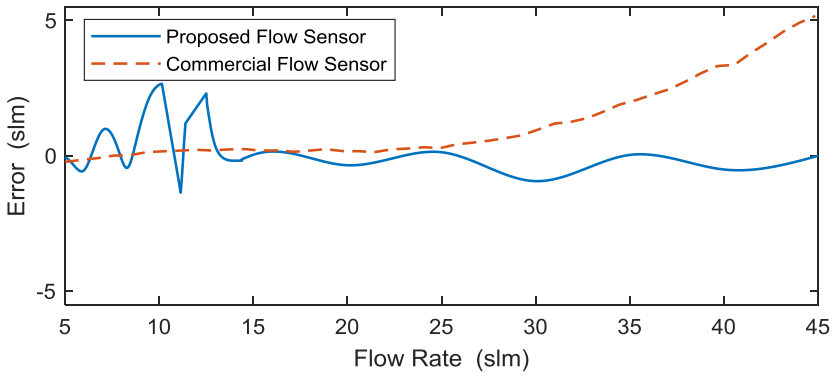

Fig. 5.18: Error as measured during the transient experiment for the asymmetrically located temperature sensors of the proposed flow sensor and error of the OMRON flow sensor.

The multi-modal operation can be also achieved in the case of an asymmetrically positioned pair, where the CTD mode can be used for low flow rates while the CP for high flow rates. The topology here ensures the same overtemperature protection and controlled power budget as this one presented in section 5.2.1.3 for the symmetrical one, since both, T_{OVER} and P, remain unchanged and exactly the same as the ones presented in Fig. 5.12. The power and overtemperature lines of the two modes cross each other at the same point; it is the same crossing point depicted in Fig. 5.17. As previously explained, that is the flow rate point where T_{OVER} is the same for CP and CTD (same applies for P), hence, the output of the sensor must be the same, no matter which mode is used. Again, a smooth transition between the modes can be achieved

by choosing that point as the toggling flow rate of the multi-modal flow sensor. Note that in contrast to Fig. 5.15 and 5.16, Fig. 5.17 shows the outputs of the asymmetrical flow sensor topology for CP and CTD without their offset removed.

The green fitting line for the output, ΔT, of the multi-modal flow sensor shown in Fig. 5.17 can be used as the expected output; hence, the sensor's accuracy for asymmetrically located temperature sensing elements can be measured. The measurement error of the proposed topology during the transient experiment has been calculated and presented in Fig. 5.18. Similar to the symmetrical topology, the measurement error of the asymmetrical is comparable with that of the micromachined commercial flow sensor.

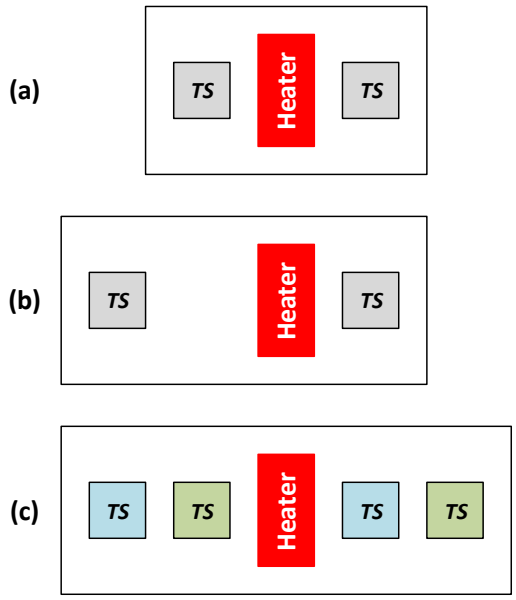

Fig. 5.19: Simplified drawing of the transducer area of (a) a symmetrical flow sensor, (b) an one-direction asymmetrical flow sensor, and (c) a bi-directional asymmetrical flow sensor. "*TS*" represents a temperature sensing element.

The main benefit of the asymmetrical topology is the higher output sensitivity for $Q>Q_{TO}$, which for the current setup can be increased up to 272%, as mentioned before. In this work, I am interested in the flows over the Q_{TO}, otherwise wide measurement range can be achieved only by increasing the power, subsequently affecting the sensor's portability. Nevertheless, asymmetrical topology comes with an increased transducer area, which might be important in some applications where the available space is limited. Moreover, the asymmetrically located temperature sensors cause

asymmetries at the output in case of bi-directional flow. It is expected that the output will not be symmetrical to zero for the case of Fig. 5.19b when the flow changes its direction. Therefore, two more temperature sensing elements need to be added in order to ensure output's symmetry (Fig. 5.19c). However, this option further increases the transducer's area, while it increases the complexity of the read-out. To sum up, there is a trade-off between output sensitivity at high flows against transducer area / complexity. For an application where high accuracy or wide measurement range are not demanded, the symmetrical topology should be preferred. However, if transducer's area is not a concern, asymmetrical topology can offer much greater output sensitivity.

5.3 DISCUSSION

This chapter presented the experimental setup and measurements of the flow sensor and its heater control circuit described in chapter 4. A quantitative analysis and comparison between the CP and CTD has been presented, demonstrating the pros and cons of each mode for flows higher and lower than the turn-over flow rate. The trade-off between power and sensitivity/Q_{TO} has been experimentally demonstrated, suggesting that, if low power is a priority, the measurement range should be extended after the Q_{TO}.

The presented analysis and comparison reinforced the argument for a multi-modal flow sensor, since CP offered a way better performance in high flows than the CTD, while the latter still offers an important overtemperature protection in low flow rates.

This flow sensor is equipped with a heater control circuit that enables the flow sensor to operate in more than one mode of operation, facilitating the toggle among the different modes. The toggling point has been determined as the point where the two modes' outputs meet, and its choice has been justified based on smooth transition from one to the other. It has been clearly demonstrated that my implementation is capable to operate in constant power and in constant overtemperature and produce reproducible results for a large range of flow rates, even with no control over the inlet temperature, T_{∞}.

The effect of the asymmetrically located temperature sensors has been also studied in this chapter for the current setup, similarly to chapter 3. The experimental results demonstrated that this topology offers greater output sensitivity for high flows, especially for the case of the CP mode. However, that comes at the cost of greater transducer area, and possibly increased read-out complexity.

5.4 CONCLUSION

- The experimental results of the first hybrid heater control circuit designed for more than one modes, have been presented and discussed. The benefits of a multi-modal flow sensor have been experimentally proven.
- This heater control system has been implemented in a calorimetric flow sensor, showing high accuracy on maintaining: the constant heater's power at CP mode, and the constant overtemperature at CTD mode, regardless of the inlet temperature and the flow rate.
- This is the first analog heater control system that enables a thermal flow sensor to operate in more than one mode, while capable to toggle among them based on the flow rate measured.
- The alternative transducer's topology of asymmetrically positioned temperature sensors have been also tested in this chapter, proving that it can substantially increase the sensitivity of a calorimetric flow sensor for flows greater than the turn-over flow rate at the cost of transducer area.

6

CONCLUSIONS AND FUTURE WORK

6.1 GENERAL CONCLUSIONS

This thesis reports the work undertaken towards the development of methods and topologies for low-power, highly sensitive calorimetric flow sensors for biomedical applications. This work is part of the development of a portable airway climate explorer (ACE), primarily, for the in situ assessment of heat and moisture exchangers' (HMEs) performance. That will be the first ACE of this purpose, providing significant information to the patient, clinicians, and HME manufacturers. The main focus of this thesis is the flow sensor of the ACE since it is the most power hungry part, and due to safety concerns of potentially high temperatures. Although the proposed methods and circuits have been developed for the application above, they could be also adopted for flow sensors for several other applications such as the flow measurement of flammable gasses.

The vast majority of the already published work addresses the issues of power consumption and sensitivity using etching and other post-processing techniques, and/or utilising non-typical materials for standard CMOS technology. These techniques, although proven successful and useful, increase the time and cost of production which contradicts with the idea of a low-cost ACE for mass production. Therefore, this thesis proposes solutions that could be implemented even on standard CMOS technology. For the purpose of quick and easy prototyping and testing, the

newly introduced methods and circuits are realised in PCB scale, using off-the-shelf components. Nevertheless, the proposed solutions have been designed and presented in way proving that they could be applied on flow sensors of any scale. In fact, the intended miniaturisation is expected to positively contribute to power consumption and sensitivity in absolute values, as many times proven in literature and analytically shown in chapter 3.

The first part of this work (section 3.1) is focussed on the transducer and how the relative positions of the sensing elements of a calorimetric flow sensor can affect the output sensitivity, and subsequently, the measurement range and the power consumption. In literature, the distance, *D*, between the heater and one of its symmetrically positioned temperature sensors often seems to be chosen arbitrarily, or for reasons not mentioned. This work provides simulation results performed for the flow range of interest and three different operating modes (CP, CT, and CTD) clearly showing the significant effect of *D* on the output sensitivity. In fact, it proves that for every mode there is a different optimal distance $D_{\min}$ that fulfils the required output sensitivity requirements. In addition, $D_{\min}$ can be chosen in a way that keeps the transducer's area as small as possible; a feature greatly important when increase in flow resistance should be avoided. Also, the interplay between $D_{\min}$ and power consumption, *P*, in CP mode is shown. The product $D_{\min} \times P$ remains unchanged for the same required output sensitivity. In other words, one can reduce the power consumption in CP by increasing the minimum required distance, or vice versa. Based on all the findings above, a novel figure of merit (FoM) that can be applied to any mode is proposed:

$$\mathrm{FoM} = D_{\min} \times \bar{P} \tag{6.1}$$

where $\bar{P}$ is the average power consumption. The FoM creates a single parameter that allows the designer to optimise power and distance simultaneously.

This work proposes additional novel modifications on the transducer for the flow sensor's performance, by investigating the effect of asymmetrically located temperature sensors in CP mode (section 3.2). A flow sensor prototype was built on a PCB using three pairs of digital SMD temperature sensors as the sensing elements. Initially, the prototype was experimentally tested for the flow range of 0~50 litres per

minutes as a typical calorimetric flow sensor of symmetrical temperature sensors, proving that it can operate accordingly. The test also proved the argument derived by the simulation results of the same chapter (chapter 3) that the greater the distance from the heater, the better the output sensitivity.

This prototype (Fig. 3.4) exhibits a typical calorimetric flow sensor's output (Fig. 3.9), which increases quickly at the beginning until reaching a maximum output, known as turn-over flow rate, Q_{TO}. After the Q_{TO} point, the output slowly decreases. It is common in literature that only the flow range 0~Q_{TO} is used due to the small output sensitivity after the Q_{TO}. It has been also proved in the literature and in this thesis, that Q_{TO} can increase by rising the power consumption. However, increasing the power for the sake of increased measurement range, contradicts the initial objective of low-power operation. Using the symmetrical topology as a reference, this work proves that the output sensitivity for flows greater than Q_{TO} can increase up to 6 times by placing the temperature sensors asymmetrically. It is an important breakthrough because flow rates greater than Q_{TO} can be now included in the measurement range without any increase in the power. From a different perspective, similar measurement ranges with less power can be achieved by utilising asymmetrically positioned temperature sensors.

As previously mentioned, the vast majority of the published work is focussed on the optimisation of the transducer to minimise power consumption and elevate output sensitivity, paying little attention to the electronics aspect of a calorimetric sensor. In fact, there is only a relatively small amount of published work with an integrated flow measurement circuit, and an even smaller amount with a more sophisticated heater control circuit. This thesis presents a hybrid, multi-modal heater control circuit that enables the flow sensor to operate and toggle between CP and CTD modes (Fig. 4.14). It constitutes a successful attempt to address practical issues such as the total power consumption through the whole measurement range, and resolve safety concerns arisen due to its particular application. The CTD is used for low flow rate, ensuring a smaller and more regulated heater temperature, T_H, compared to CP. CP is used for high flow rates, offering a lower and more predictable overall power budget. The toggling point is experimentally chosen as the point where the power, P, and overtemperature, T_{OVER}, are the same for both modes, hence, the output, ΔT, is also

the same, ensuring a smooth transition between the modes. Specifically, a T_{OVER} reduction of up to 9.5% is achieved by using CTD instead of CP in low flow rates, and a heater power reduction up to 13.6% by using CP instead of CTD in high flow rates. This is the first dual-mode heater control circuit to operate in CP/CTD.

The novel heater control circuit was tested for transducers of symmetrically and asymmetrically placed temperature sensors for both modes, CP and CTD. Experimental evidence suggest that the output sensitivity after the Q_{TO} increases for CP and for CTD too, when asymmetrical temperature sensors are used. In particular, it is more than 272% and 163% increase for the CP and the CTD, respectively, suggesting that flow rates larger than Q_{TO} can be also included in the measurement range, without challenging the flow measurement circuit.

To implement the novel dual-mode heater control circuit, two new heater control circuits, one for each mode, are introduced (Fig. 4.2 and Fig. 4.4). It is the first time those topologies are used as heater control circuits for calorimetric flow sensors. There are different reasons why these new topologies should have been introduced for the dual-mode system. Since a heater of high TCR is required to enable the heater's temperature monitoring, the application of constant voltage or current at the heater will never work as CP. Hence, a method for the accurate power delivery at a heater should be devised. As far as CTD is concerned, self-heating issues of the ambient temperature sensing resistor, as well as the use of temperature ratio (T_H/T_∞) instead of the temperature difference (T_H - T_∞) often affect the reproducibility and accuracy of the measurements.

The proposed circuits address those issues by using analog multiplier and analog dividers to accurately determine P and, T_H and T_∞, respectively. In addition, the current flowing through the ambient temperature sensing resistor, R_∞, is completely independent of the current through the heater, R_H, thus, self-heating is not an issue anymore. In fact, R_H and R_∞ can be easier realised now on a different substrate, facilitating the thermal isolation of those two resistors. The newly introduced heater control circuit designs are bringing other benefits as well, such as flexibility. The defining parameter of the mode (i.e. T_{OVER} for the CTD, or P for the CP) can now be modified quicker, or even on the fly, since it is defined by a reference voltage (i.e. V_{CTD} or V_{CP}, for the CTD and the CP respectively), as Fig. 4.14 depicts.

The design of the individual heater control circuits, as well as the dual-mode one, are described in detail in chapter 4. Their measured performance in chapter 5 shows that the proposed designs offer excellent reproducibility, even though T_{∞} was free to fluctuate during the experiments.

In summary, this thesis proposes novel methods and circuits towards the next inexpensive, low-power and biomedically safe calorimetric flow sensor. The solutions consist of investigations for the optimisation of the transducer's area and, of the development of smart, multi-modal heater control circuits. Although the proposed methods are intended for respiratory monitoring, they could also be adopted by other applications.

6.2 FUTURE WORK

This section discusses methods and potential future work for the further improvement of the work presented in this thesis.

6.2.1 Further Asymmetrical Calorimetric Flow Sensor Investigations

Investigation of the asymmetrically located temperature sensors' impact on the flow sensor's output have been presented in this work. However, only the temperature sensor closer at the heater at the downstream side has been used (TS2 as Fig. 6.1 depicts) with all the possible combinations at the upstream (TS1, TS3, and TS5). Studies with asymmetrical topologies formed using the rest of the downstream temperature sensors (TS4 and TS6) should also be conducted. The impact of the rest possible pairs on the sensitivity, power consumption, and measurement range should be evaluated, as conducted for the pairs described in the previous chapters.

Such an investigation will provide a complete description of the effect of all the possible combinations of the temperature sensors on flow's measurement output, for better optimisation of the temperature sensors' relative position.

In addition, the output for flows of the opposite direction should be also investigated. This is of high importance since the flow sensor must be able to operate for both directions. For asymmetrical pairs, it is expected that the output of the flow

sensor, ΔT, will not be symmetrical to the zero flow point. The study of the output for both flow directions will determine the necessity or not to use only one asymmetrical pair or two, as discussed in chapter 5 (Fig. 5.16).

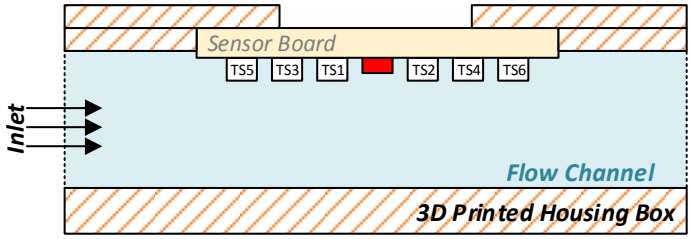

Fig. 6.1: Cross-sectional drawing of a transducer and its housing box, used for this work. "*TS1"* to "*TS6*" are the temperature sensors. The heater is illustrated in red colour.

6.2.2 Miniaturisation

As mentioned before, the ultimate goal of the whole project is the development of an integrated ACE, requiring the miniaturisation of the flow sensor. It has been proven in literature and analytically shown in chapter 2, that miniaturisation is expected to lower the power consumption for the same measurement range, as well as improve sensitivity and response time. The cost of the ACE should remain as low as possible, hence, standard CMOS is preferred, avoiding expensive post-processing techniques. However, 'no-use of etching' combined with the use of a substrate of high thermal conductivity will have an undesirable impact on the power consumption. Nevertheless, flow sensors fabricated in standard CMOS only, exhibit lower power consumption than the one presented here, even for a wider measurement range [81].

A polysilicon resistor is a common choice of heater in standard CMOS. Thermopiles will be preferred as temperature sensing elements. As explained in chapter 2, a thermopile is self-powered, which is an important benefit for the low-power ACE, and its design is rather straightforward. Thermopiles are extensively used in CMOS flow sensors due to their easy implementation and the high Seebeck coefficient one can get. Combinations of n-poly/Al, p-poly/Al, and p-poly/n-poly are prevalent in the literature, offering Seebeck coefficients of hundreds of μV/K [54], [68], [69].

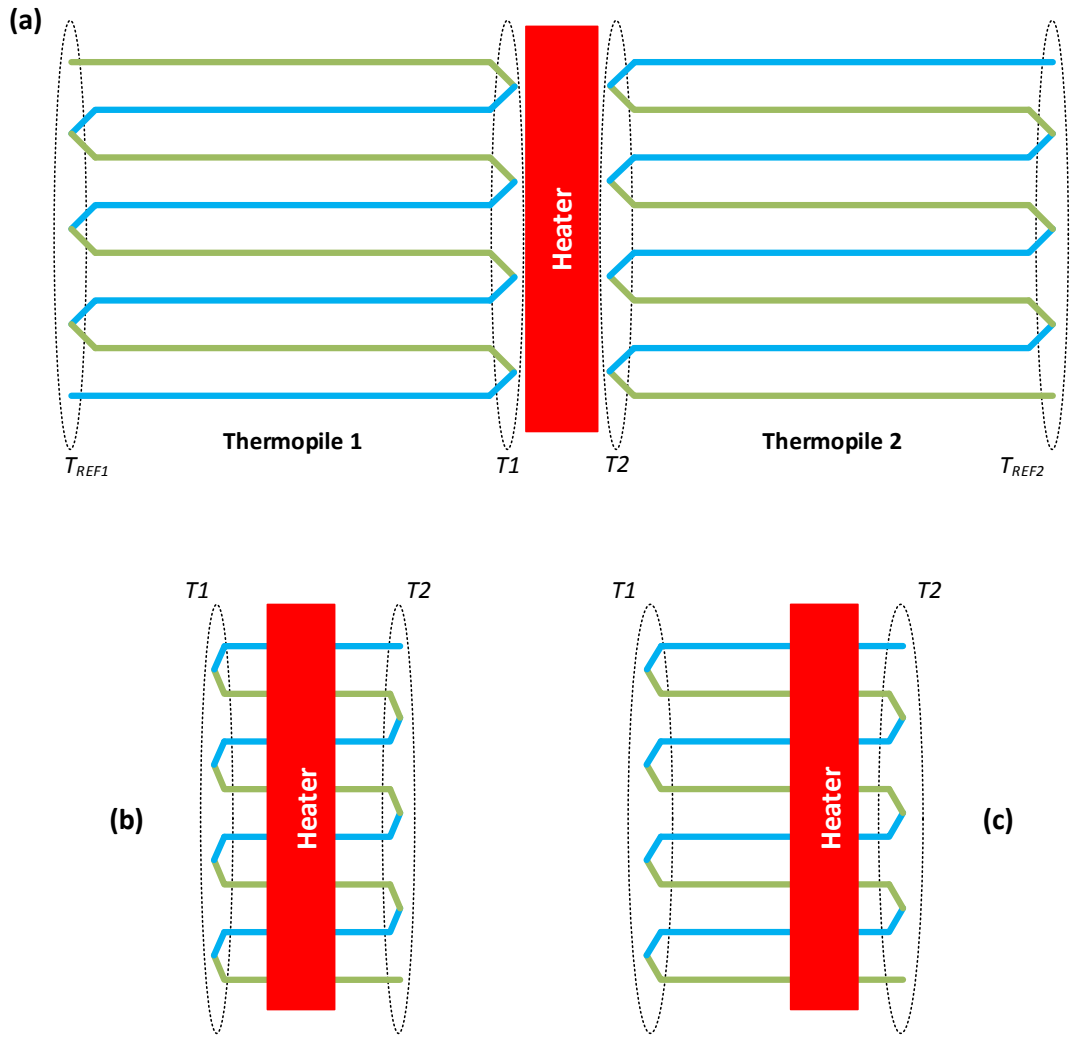

Fig. 6.2: (a): Typical thermoelectric flow sensor illustration using one thermopile at each side to measure the output ΔT. A modified thermoelectric flow sensor using only one thermopile to directly measure the output, ΔT, at (b) symmetrical, and (c) asymmetrical positions.

Typically, a thermoelectric flow sensor is implemented as Fig. 6.2a depicts. Assuming that the output of a thermopile, V_{TX}, is:

$$V_{TX} = n\, S_{AB}\, (T_X - T_{REFX}) \tag{6.1}$$

where n is the number of thermocouples and S_{AB} the Seebeck coefficient, the output, ΔT, of Fig. 6.2a will be:

$$\Delta T = V_{T1} - V_{T2} = n\, S_{AB}\, (T_1 - T_2 + T_{REF2} - T_{REF1}) \tag{6.2}$$

Hence, the flow sensor's output is the true temperature difference, $T_1 - T_2$, only when $T_{REF1} = T_{REF2}$. As previously explained, the value of the reference temperatures might

not be equal, leading to erroneous measurements. A common method in literature to avoid this issue is to make the thermopiles large enough so the reference temperatures are not affected by the heater. However, this option leads to an increase in the transducer's area, which consequently increases the total size and cost of the ACE.

In Fig. 6.2b a new thermoelectric transducer design is proposed. Specifically, one only thermopile is used that directly produces the flow sensor's output, ΔT, at its two terminals, hence, no reference temperatures are required to be cancelled out. In addition, the size of the thermopile can be small, reducing the area of the transducer substantially compared to Fig. 6.2a. An asymmetrical implantation is also possible, as Fig. 6.3c depicts.

Further improvements can be implemented on the multi-modal heater control circuit presented in this work. In particular, one only analog multiplier cell can be implemented, instead of three as presented in previous chapters. This cell will alternate its operation among the operations that the three other cells do in this work; calculation of V_{MULT}, V_{DIVH}, and $V_{\mathrm{DIV}\infty}$. Such an implementation might significantly contribute towards the reduction of the total power consumption of the ACE.

Lastly, practical issues must be also considered due to the harsh environment where the ACE is going to operate. In fact, a highly humid environment is expected, as well as possible pollutants. Pollutants or moisture that might deposit on the transducer is expected to significantly affect the flow sensor's output. Therefore, the surface of the flow sensor must be protected to ensure reliability of the sensor and reproducibility of its measurements. As discussed in chapter 2, two techniques are commonly used in the literature: back surface sensing, and ceramic plate adhesion on the transducer's area. The former has a more negative effect on the power consumption than the latter. In addition, the back surface sensing might not be possible in this case, since the chip will carry other sensors as well that might require their direct contact to the fluid. Therefore, the adhesion of a ceramic board on the transducer is preferred, to offer a smooth surface for the flow while protecting the flow sensor.

6.2.3 Flow Sensor's Assessment under Respiration Conditions

The proposed flow sensor will have to be experimentally tested under conditions similar to those during respiration, such as those of flow pattern, flow direction, and change in humidity.

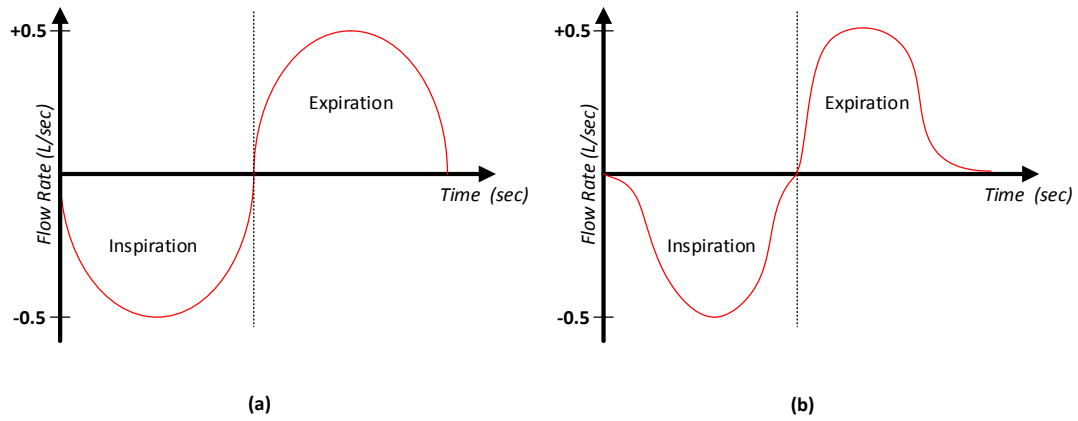

Fig. 6.3: (a): Simplified human respiratory pattern over time as commonly assumed in literature. (b) A more realistic flow regime during respiration.

Respiratory flow regime in rest might differ substantially among healthy adults since it depends on various factors, such as gender, age, and fitness level. Nevertheless, its waveform is usually depicted as sinusoidal of a period of 6 sec and amplitude of 0.5 litres per second (30slm) [91]–[93]. Such a waveform is shown in Fig. 6.3a. However, Fig. 6.3a is an idealised situation, hence, a more realistic respiratory flow pattern is shown in Fig. 6.3b [94]. One should notice that the inspiration waveform is skewed to the right whereas the expiration to the left, but most importantly, note that there is a period of approximately of one second after the expiration that the flow rate is zero, where the T_{OVER} could rise substantially if CP mode was used.

In order to reproduce more accurately human's respiration, the flow sensor should also be tested bi-directionally; hence, a more elaborate lab test will be required to implement it.

Another important aspect of human's respiration is the vast changes in humidity. In fact, relative humidity during expiration is expected to be around 100%, whereas relative humidity at inhalation will be the same of the environment, commonly 20 to

50%. Nevertheless, recent work [95] claim that the effect of humidity on the output of a calorimetric flow sensor is less than 0.6% for T_∞ = 20 ºC, and less than 1.8% when T_∞ = 40 ºC; therefore, the vast and quick changes in humidity are not expected to significantly impact the flow sensor's accuracy.

APPENDIX

A. HEAT TRANSFER MODES

Heat Transfer is the discipline that studies the exchange of thermal energy between physical objects. There are three modes of heat transfer [96]:

- Conduction
- Convection
- Radiation

Any energy exchange between physical objects occurs through one of these phenomena or a combination of them.

Thermal **conduction** is the transfer of energy due to interactions and collisions of the particles within an object. The thermal energy is moved for the more energetic particles to the less energetic. Conduction takes place in solids and standing fluids, and it is described by Fourier's law:

$$q = -k\nabla T \tag{A.1}$$

where q is the heat flux, k is the thermal conductivity of the object, and T is the temperature.

Heat flux (q) is the amount of heat energy passing through a unity surface, and it is measured in W/m^2.

Thermal conductivity (k) is the property of a material to conduct heat, and it is measured in W/(m K). It describes the amount of heat energy transferred in 1m distance within the material, assuming that the temperature difference is 1K. Gasses usually have lower thermal conductivity than solids.

In contrast, *thermal diffusivity (a)* is a measure of how fast a material can carry heat away and it is equal to $k/\rho C$, where k is the thermal conductivity, ρ the density, and C the specific heat capacity, of the material. Thermal diffusivity is an important factor in transient problems.

Thermal **convection** is the mode of heat transfer that takes place only in moving fluids, and consists of two mechanisms: one taking place in microscopic level and the other one in macroscopic. Energy moves due to interactions among particles (microscopic) and, in bulk as particles move collectively due to the motion of the fluid (macroscopic). Convection is described by the Newton's law of cooling as:

$$q = h(T_H - T_\infty) \tag{A.2}$$

where T_H is the temperature of the hot surface that interacts with the fluid, and T_∞ the temperature of the fluid.

h is the heat transfer coefficient (W/m^2K) and it depends conditions of the boundary layer, the surface geometry, and the properties of the fluid. Any study of convection ultimately reduces to a study of determining h [73]. The value of heat transfer coefficient might vary from single digits up to 5 orders of magnitude. For the same physical setup, and for a fluid of a stable composition and temperature, h varies mainly due to changes in fluid's velocity.

Thermal **radiation** is the emission of thermal energy from a matter in the form of electromagnetic waves. Compared to thermal conduction and convection, thermal radiation does not require the presence of a material medium. In fact, radiation is more efficient in a vacuum, and it is described by Stefan-Boltzmann law:

$$q = \sigma\left({T_H}^4 - {T_\infty}^4\right) \tag{A.3}$$

where $\sigma = 5.67 \times 10^{-8}\ W/m^2\ K^4$ is the Stefan-Boltzmann constant.

BIBLIOGRAPHY

[1] "NHS UK." [Online]. Available: http://www.nhs.uk/conditions/Cancer-of-the-larynx/Pages/Introduction.aspx.

[2] "Cancer Research UK." [Online]. Available: http://www.cancerresearchuk.org/health-professional/cancer-statistics/statistics-by-cancer-type/laryngeal-cancer/incidence.

[3] A. H. Ackerstaff, F. J. M. Hilgers, N. K. Aaronson, M. F. De Boer, C. A. Meeuwis, P. P. M. Knegt, H. A. A. Spoelstra, N. van Zandwijk, and A. J. M. Balm, "Heat and moisture exchangers as a treatment option in the post-operative rehabilitation of laryngectomized patients," *Clin. Otolaryngol.*, vol. 20, no. 6, pp. 504–509, Dec. 1995.

[4] T. Keck, J. Dürr, R. Leiacker, G. Rettinger, and A. Rozsasi, "Tracheal climate in laryngectomees after use of a heat and moisture exchanger," *Laryngoscope*, vol. 115, no. 3, pp. 534–7, Mar. 2005.

[5] J. K. Zuur, S. H. Muller, F. H. C. De Jongh, N. Van Zandwijk, and F. J. M. Hilgers, "The physiological rationale of heat and moisture exchangers in post-laryngectomy pulmonary rehabilitation: A review," *Eur. Arch. Oto-Rhino-Laryngology*, vol. 263, no. 1, pp. 1–8, 2006.

[6] R. J. Scheenstra, S. H. Muller, A. Vincent, M. Sinaasappel, and F. J. M. Hilgers, "Influence of breathing resistance of heat and moisture exchangers on tracheal climate and breathing pattern in laryngectomized individuals," *Head Neck*, vol. 32, no. 8, pp. 1069–78, Aug. 2010.

[7] R. J. Scheenstra, S. H. Muller, and F. J. M. Hilgers, "Endotracheal temperature and humidity in laryngectomized patients in a warm and dry environment and the effect of a heat and moisture exchanger," *Head Neck*, vol. 33, no. 9, pp. 1285–93, Sep. 2011.

[8] M. Chandler, "Measurement of heat and moisture exchanger efficiency,"

Anaesthesia, vol. 68, no. 9, pp. 953–60, Sep. 2013.

[9] J. K. Zuur, S. H. Muller, A. Vincent, M. Sinaasappel, F. H. C. de Jongh, and F. J. M. Hilgers, "Assessment of tracheal temperature and humidity in laryngectomized individuals and the influence of a heat and moisture exchanger on tracheal climate," *Head Neck*, vol. 30, no. 8, pp. 1072–82, Aug. 2008.

[10] W. Grolman, E. D. Blom, R. D. Branson, P. F. Schouwenburg, and R. C. Hamaker, "An Efficiency Comparison of Four Heat and Moisture Exchangers Used in the Laryngectomized Patient," *Laryngoscope*, vol. 107, no. 6, pp. 814–820, Jun. 1997.

[11] T. Rui, H. Hai, Y. Yong Mo, J. Oiler, L. Mengbing, and Y. Hongyu, "Three-Dimensional Flexible Thermal Sensor for Intravascular Flow Monitoring," *IEEE Sens. J.*, vol. 13, no. 10, pp. 3991–3998, 2013.

[12] A. Baldwin, L. Yu, and E. Meng, "An Electrochemical Impedance-Based Thermal Flow Sensor for Physiological Fluids," *IEEE J. Microelectromechanical Syst.*, vol. 25, no. 6, pp. 1015–1024, 2016.

[13] Z. Yi, M. Qin, and Q.-A. Huang, "Experiment of the MEMS Wind Sensor Based on Temperature-Balanced Mode," *IEEE Sens. J.*, vol. 17, no. 8, pp. 2316–2317, 2017.

[14] M. Ahmed, W. Xu, S. Mohamad, M. Duan, Y.-K. Lee, and A. Bermak, "Integrated CMOS-MEMS Flow Sensor With High Sensitivity and Large Flow Range," *IEEE Sens. J.*, vol. 17, no. 8, pp. 2318–2319, 2017.

[15] F. Hedrich, K. Kliche, M. Storz, S. Billat, M. Ashauer, and R. Zengerle, "Thermal flow sensors for MEMS spirometric devices," *Sensors Actuators A Phys.*, vol. 162, no. 2, pp. 373–378, 2010.

[16] G. Bonmarchand, V. Chevron, C. Chopin, D. Jusserand, C. Girault, F. Moritz, J. Leroy, and P. Pasquis, "Increased initial flow rate reduces inspiratory work of breathing during pressure support ventilation in patients with exacerbation of chronic obstructive pulmonary disease," *Intensive Care Med.*, vol. 22, pp. 1147–1154, 1996.

[17] M. R. Hetzel and T. J. Clark, “Comparison of normal and asthmatic circadian rhythms in peak expiratory flow rate.,” *Thorax*, vol. 35, pp. 732–738, 1980.

[18] N. T. Nguyen, “Micromachined flow sensors—a review,” *Flow Meas. Instrum.*, vol. 8, no. 1, pp. 7–16, Mar. 1997.

[19] J. T. W. Kuo, L. Yu, and E. Meng, “Micromachined thermal flow sensors-A review,” *Micromachines*, vol. 3, pp. 550–573, 2012.

[20] K. Imin, A. Kumar, and J. Binder, “Smart MEMS Flow Sensor: Theoretical Analysis and Experimental Characterization,” *IEEE Sens. J.*, vol. 7, no. 5, pp. 713–722, 2007.

[21] P. Enoksson, G. Stemme, and E. Stemme, “A silicon resonant sensor structure for coriolis mass-flow measurements,” *IEEE J. Microelectromechanical Syst.*, vol. 6, no. 2, pp. 119–125, 1997.

[22] O. Berberig, K. Nottmeyer, J. Mizuno, Y. Kanai, and T. Kobayashi, “The Prandtl micro flow sensor (PMFS): a novel silicon diaphragm capacitive sensor for flow-velocity measurement,” *Sensors Actuators A Phys.*, vol. 66, no. 1–3, pp. 93–98, 1998.

[23] W. Xu, K. Song, S. Ma, B. B. Gao, Y. Chiu, and Y.-K. Lee, “Theoretical and Experimental Investigations of Thermoresistive Micro Calorimetric Flow Sensors Fabricated by CMOS MEMS Technology,” *IEEE J. Microelectromechanical Syst.*, vol. 25, no. 5, pp. 954–962, 2016.

[24] B. W. van Oudheusden, “Silicon thermal flow sensors,” *Sensors Actuators A Phys.*, vol. 30, no. 1–2, pp. 5–26, Jan. 1992.

[25] H. Berthet, J. Jundt, J. Durivault, B. Mercier, and D. Angelescu, “Time-of-flight thermal flowrate sensor for lab-on-chip applications,” *Lab Chip*, vol. 11, no. 2, pp. 215–223, 2011.

[26] L. Yu, B. J. Kim, and E. Meng, “An implantable time of flight flow sensor,” in *IEEE Int’l Conf. on Micro Electro Mechanical Systems (MEMS)*, 2015, vol. 2015–Febru, no. February, pp. 620–623.

[27] C. Yang and H. Søeberg, “Monolithic flow sensor for measuring millilitre per minute liquid flow,” *Sensors Actuators A Phys.*, vol. 33, no. 3, pp. 143–153, Jun. 1992.

[28] J. van Kuijk, T. S. J. Lammerink, H.-E. de Bree, M. Elwenspoek, and J. H. J. Fluitman, “Multi-parameter detection in fluid flows,” *Sensors Actuators A Phys.*, vol. 46–47, no. 1–3, pp. 369–372, 1995.

[29] A. Al-Salaymeh, J. Jovanović, and F. Durst, “Bi-directional flow sensor with a wide dynamic range for medical applications,” *Med. Eng. Phys.*, vol. 26, no. 8, pp. 623–37, Oct. 2004.

[30] C. Offenzeller, M. Knoll, T. Voglhuber-Brunnmaier, M. A. Hintermuller, B. Jakoby, and W. Hilber, “Fully Screen Printed Thermocouple and Microheater Applied for Time-of-Flight Sensing in Microchannels,” *IEEE Sens. J.*, vol. 18, no. 21, pp. 8685–8692, 2018.

[31] H. B. Liu, N. Lin, S. S. Pan, J. Miao, and L. K. Norford, “High sensitivity, miniature, full 2-D anemometer based on MEMS hot-film sensors,” *IEEE Sens. J.*, vol. 13, no. 5, pp. 1914–1920, 2013.

[32] E. L. W. Gardner, T. A. Vincent, R. G. Jones, J. W. Gardner, J. Coull, A. De Luca, and F. Udrea, “MEMS Thermal Flow Sensors— An Accuracy Investigation,” *IEEE Sens. J.*, vol. 19, no. 8, pp. 2991–2998, Apr. 2019.

[33] L. V. King, “On the Convection of Heat from Small Cylinders in a Stream of Fluid: Determination of the Convection Constants of Small Platinum Wires, with Applications to Hot-Wire Anemometry,” *Proc. R. Soc. London A Math. Phys. Eng. Sci.*, vol. 90, no. 622, pp. 563–570, 1914.

[34] W. Xu, B. Gao, S. Ma, A. Zhang, Y. Chiu, and Y. K. Lee, “Low-cost temperature-compensated thermoresistive micro calorimetric flow sensor by using 0.35μm CMOS MEMS technology,” in *IEEE Int’l Conf. on Micro Electro Mechanical Systems (MEMS)*, 2016, pp. 189–192.

[35] P. C. Stainback and K. A. Nagabushana, “Review of Hot-Wire Anemometry Techniques and the Range of their Applicability for Various Flows,” *Electron.*

J. Fluids Eng. Trans. ASME, vol. 167, pp. 1–54, 1993.

[36] A. F. P. van Putten and S. Middelhoek, "Integrated silicon anemometer," *Electron. Lett.*, vol. 10, no. 21, pp. 425–426, 1974.

[37] S. Wu, Q. Lin, Y. Yuen, and Y. C. Tai, "MEMS flow sensors for nano-fluidic applications," *Sensors Actuators A Phys.*, vol. 89, pp. 152–158, 2001.

[38] C. Sosna, R. Buchner, and W. Lang, "A Temperature Compensation Circuit for Thermal Flow Sensors Operated in Constant-Temperature-Difference Mode," *IEEE Trans. Instrum. Meas.*, vol. 59, no. 6, pp. 1715–1721, Jun. 2010.

[39] R. P. C. Ferreira and R. C. S. Freire, "Hot-wire anemometer with temperature compensation using only one sensor," *IEEE Trans. Instrum. Meas.*, vol. 50, no. 4, pp. 954–958, 2001.

[40] M. M. Sadeghi, R. L. Peterson, and K. Najafi, "Air flow sensing using micro-wire-bonded hair-like hot-wire anemometry," *J. Micromechanics Microengineering*, vol. 23, p. 085017, 2013.

[41] Y.-Q. Zhu, B. Chen, M. Qin, and Q.-A. Huang, "2-D Micromachined Thermal Wind Sensors - A Review," *IEEE J. Internet Things*, vol. 1, no. 3, pp. 216–232, 2014.

[42] R. G. Johnson and R. E. Higashi, "A highly sensitive silicon chip microtransducer for air flow and differential pressure sensing applications," *Sensors and Actuators*, vol. 11, pp. 63–72, 1987.

[43] S. Cerimovic, A. Talić, T. Sauter, F. Kohl, R. Beigelbeck, J. Schalko, and A. Jachimowicz, "A novel thermal transduction method for sub-mW flow sensors," in *IEEE SENSORS*, 2009, pp. 1325–1328.

[44] M. Ahmed, S. Mohamad, and A. Bermak, "A nested-chopped current-feedback instrumentation amplifier for MEMS flow sensors," in *IEEE MWSCAS*, 2016, no. October, pp. 1–4.

[45] Y.-Q. Zhu, M. Qin, J. Q. Huang, Z. Yi, and Q.-A. Huang, "Sensitivity Improvement of a 2D MEMS Thermal Wind Sensor for Low-Power

Applications," *IEEE Sens. J.*, vol. 16, no. 11, pp. 4300–4308, Jun. 2016.

[46] W. Brevet, F. Sebastiano, and K. A. A. Makinwa, "A 25 mW smart CMOS wind sensor with corner heaters," in *IEEE IECON*, 2015, pp. 1194–1199.

[47] M. Ahmed, W. Xu, S. Mohamad, F. Boussaid, Y.-K. Lee, and A. Bermak, "Fully Integrated Bidirectional CMOS-MEMS Flow Sensor With Low Power Pulse Operation," *IEEE Sens. J.*, vol. 19, no. 9, pp. 3415–3424, May 2019.

[48] J. Wu, C. van Vroonhoven, Y. Chae, and K. A. A. Makinwa, "A 25mW CMOS sensor for wind and temperature measurement," in *IEEE SENSORS*, 2011, pp. 1261–1264.

[49] Z. Dong, Q.-A. Huang, and M. Qin, "Thermal asymmetry compensation of a wind sensor fabricated on ceramic substrate," in *IEEE SENSORS*, 2010, pp. 595–599.

[50] P. Bruschi, A. Diligenti, D. Navarrini, and M. Piotto, "A double heater integrated gas flow sensor with thermal feedback," *Sensors Actuators A Phys.*, vol. 123–124, pp. 210–215, 2005.

[51] A. Glaninger, A. Jachimowicz, F. Kohl, R. Chabicovsky, and G. Urban, "Wide range semiconductor flow sensors," *Sensors Actuators A Phys.*, vol. 85, no. 1–3, pp. 139–146, Aug. 2000.

[52] W. Xu, B. Lijin, M. Duan, X. Wang, J. Wicaksana, A. Min, M. Ahmed, R. Wang, N. X. Fang, A. Bermak, and Y. Lee, "A wireless dual-mode micro thermal flow sensor system with extended flow range by using CMOS-MEMS process," in *IEEE Micro Electro Mechanical Systems (MEMS)*, 2018, pp. 824–827.

[53] M. Ashauer, H. Glosch, F. Hedrich, N. Hey, H. Sandmaier, and W. Lang, "Thermal flow sensor for liquids and gases based on combinations of two principles," *Sensors Actuators A Phys.*, vol. 73, no. 1–2, pp. 7–13, 1999.

[54] M. Piotto, M. Dei, F. Butti, G. Pennelli, and P. Bruschi, "Smart flow sensor with on-chip CMOS interface performing offset and pressure effect

compensation," *IEEE Sens. J.*, vol. 12, no. 12, pp. 3309–3317, 2012.

[55] G. P. Shen, M. Qin, and Q.-A. Huang, "A cross-type thermal wind sensor with self-testing function," *IEEE Sens. J.*, vol. 10, no. 2, pp. 340–346, 2010.

[56] G. Kaltsas, P. Katsikogiannis, P. Asimakopoulos, and A. G. Nassiopoulou, "A smart flow measurement system for flow evaluation with multiple signals in different operation modes," *Meas. Sci. Technol.*, vol. 18, p. 3617, 2007.

[57] B. Mimoun, A. van der Horst, R. Dekker, D. van der Voort, A. van der Horst, M. Rutten, F. van de Vosse, and R. Dekker, "Thermal flow sensors on flexible substrates for minimally invasive medical instruments," in *IEEE SENSORS*, 2012, pp. 1–4.

[58] T. S. J. Lammerink, N. R. Tas, M. Elwenspoek, and J. H. J. Fluitman, "Micro-liquid flow sensor," *Sensors Actuators A Phys.*, vol. 37–38, pp. 45–50, 1993.

[59] C. Hoera, M. M. Skadell, S. A. Pfeiffer, M. Pahl, Z. Shu, E. Beckert, and D. Belder, "A chip-integrated highly variable thermal flow rate sensor," *Sensors Actuators B Chem.*, vol. 225, pp. 42–49, Mar. 2016.

[60] S. Takagi, "A hot-wire anemometer compensated for ambient temperature variations," *J. Phys. E.*, vol. 19, pp. 739–743, 1986.

[61] W. Xu, B. Gao, M. Ahmed, M. Duan, B. Wang, S. Mohamad, A. Bermak, and Y.-K. Lee, "A wafer-level encapsulated CMOS MEMS thermoresistive calorimetric flow sensor with integrated packaging design," in *IEEE Int'l Conf. on Micro Electro Mechanical Systems (MEMS)*, 2017, pp. 989–992.

[62] A. Petropoulos and G. Kaltsas, "Study and Evaluation of a PCB-MEMS Liquid Microflow Sensor," *Sensors*, vol. 10, no. 10, pp. 8981–9001, Oct. 2010.

[63] Y. Ye, Z. Yi, S. Gao, M. Qin, and Q.-A. Huang, "Effect of Insulation Trenches on Micromachined Silicon Thermal Wind Sensors," *IEEE Sens. J.*, vol. 17, no. 24, pp. 8324–8331, 2017.

[64] S. Wang, J. Wang, Z. Yi, M. Qir, and Q.-A. Huang, "Experimental Study of a Dual-Mode Control MEMS Wind Sensor with High Accuracy," in *IEEE*

SENSORS, 2018, pp. 31–34.

[65] S. Dalola, S. Cerimovic, F. Kohl, and R. Beigelbeck, "MEMS thermal flow sensor with smart electronic interface circuit," *IEEE Sens. J.*, vol. 12, no. 12, pp. 3318–3328, 2012.

[66] Y. Ye, Z. Yi, S. Gao, M. Qin, and Q.-A. Huang, "DRIE Trenches and Full-Bridges for Improving Sensitivity of 2-D Micromachined Silicon Thermal Wind Sensor," *IEEE J. Microelectromechanical Syst.*, vol. 26, no. 5, pp. 1073–1081, Oct. 2017.

[67] A. Talić, S. Cerimovic, R. Beigelbeck, F. Kohl, A. Jachimowicz, and F. Keplinger, "Novel Thermal Flow Sensors Based on a Wheatstone Bridge Read-out," *Procedia Chem.*, vol. 1, no. 1, pp. 136–139, Sep. 2009.

[68] P. Bruschi, M. Dei, and M. Piotto, "An offset compensation method with low residual drift for integrated thermal flow sensors," *IEEE Sens. J.*, vol. 11, no. 5, pp. 1162–1168, 2011.

[69] K. A. A. Makinwa and J. H. Huijsing, "A wind sensor with an integrated low-offset instrumentation amplifier," in *IEEE ICECS*, 2001, pp. 1505–1508.

[70] A. De Luca, C. Falco, E. L. W. Gardner, J. D. Coull, and F. Udrea, "Diode-based CMOS MEMS Thermal Flow Sensors," in *Int'l Conf. on Solid-State Sensors, Actuators and Microsystems (TRANSDUCERS)*, 2017, pp. 2211–2214.

[71] A. S. Sedra and K. C. Smith, *Microelectronic Circuits*, 6th ed. New York, Oxford: Oxford University Press, 2011.

[72] G. C. M. Meijer, *Smart Sensor Systems*. Chichester, UK: John Wiley & Sons, Ltd, 2008.

[73] F. P. Incropera, D. P. DeWitt, T. L. Bergman, and A. S. Lavine, *Fundamentals of heat and mass transfer*, 6th ed. USA: John Wiley & Sons, 2007.

[74] G. Kaltsas and A. G. Nassiopoulou, "Novel C-MOS compatible monolithic silicon gas flow sensor with porous silicon thermal isolation," *Sensors*

Actuators A Phys., vol. 76, no. 1–3, pp. 133–138, Aug. 1999.

[75] Y.-Q. Q. Zhu, B. Chen, M. Qin, J. Q. Huang, and Q.-A. Huang, "A self-packaged self-heated thermal wind sensor with high reliability and low power consumption," in *IEEE Int'l Conf. on Nano/Micro Engineered and Molecular Systems*, 2015, pp. 193–196.

[76] T. Sauter, T. Glatzl, F. Kohl, H. Steiner, and A. Talić, "Thermal flow sensors based on printed circuit board technology," in *IEEE Int'l Symp. on Quality Electronic Design*, 2014, pp. 748–753.

[77] R. Que and R. Zhu, "A Compact Flexible Thermal Flow Sensor for Detecting Two-Dimensional Flow Vector," *IEEE Sens. J.*, vol. 15, no. 3, pp. 1931–1936, 2015.

[78] R. Buchner, K. Froehner, C. Sosna, W. Benecke, and W. Lang, "Toward flexible thermoelectric flow sensors: A new technological approach," *IEEE J. Microelectromechanical Syst.*, vol. 17, no. 5, pp. 1114–1119, 2008.

[79] J. Chen, Z. Fan, J. Zou, J. Engel, and C. Liu, "Two-Dimensional Micromachined Flow Sensor Array for Fluid Mechanics Studies," *J. Aerosp. Eng.*, vol. 16, no. 2, pp. 85–97, Apr. 2003.

[80] J. Sun, M. Qin, and Q.-A. Huang, "Flip-Chip Packaging for a Two-Dimensional Thermal Flow Sensor Using a Copper Pillar Bump Technology," *IEEE Sens. J.*, vol. 7, no. 1, pp. 990–995, 2007.

[81] J. Wu, Y. Chae, C. Van Vroonhoven, and K. A. A. Makinwa, "A 50mW CMOS wind sensor with ±4% speed and ±2° direction error," in *IEEE ISSCC Dig. Tech. Papers*, 2011, pp. 106–108.

[82] C. H. Hsueh, C. R. Luttrell, and T. Cui, "Thermal stress analyses of multilayered films on substrates and cantilever beams for micro sensors and actuators," *J. Micromechanics Microengineering*, vol. 16, no. 11, pp. 2509–2515, 2006.

[83] N. Sabaté, J. Santander, L. Fonseca, I. Gràcia, and C. Cané, "Multi-range silicon

micromachined flow sensor," *Sensors Actuators A Phys.*, vol. 110, pp. 282–288, 2004.

[84] W. T. Blows, *The Biological Basis of Nursing: Clinical Observations*. London: Routledge, 2001.

[85] V. Kitsos, S. West, A. Demosthenous, and X. Liu, "Design Considerations and Optimization of Calorimetric Flow Sensor for Respiratory Monitoring," in *IEEE Biomedical Circuits and Systems Conference (BioCAS)*, 2016, no. 2, pp. 26–29.

[86] N. T. Nguyen and W. Dötzel, "Asymmetrical locations of heaters and sensors relative to each other using heater arrays: a novel method for designing multi-range electrocaloric mass-flow sensors," *Sensors Actuators A Phys.*, vol. 62, pp. 506–512, 1997.

[87] D. Sackett, "Supply Constant Power Level To A Varying Load Impedance," *Electronic Design Magazine*, Dec-2006.

[88] D. Sackett, "Application Note 4470: Constant-Power Source. Maxim Integrated Products," 2009.

[89] R. Pallas-Areny and J. G. Webster, "Common Mode Rejection Ratio for Cascaded Differential Amplifier Stages," *IEEE Trans. Instrum. Meas.*, vol. 40, no. 4, pp. 677–681, 1991.

[90] A. Bakker and J. H. Huijsing, *High-Accuracy CMOS smart temperature sensors*. Dordrecht, The Netherlands: Kluwer Academic Publishers, 2000.

[91] A. Davies and C. Moores, *The Respiratory System*, 2nd ed. Churchill Livingstone, 2010.

[92] M. Cloutier, *Respiratory Physiology*, 2nd ed. Elsevier, 2018.

[93] A. Myers and P. McGowan, *Crash Course: Respiratory System*, 1st ed. Saunders, 2005.

[94] N. Staub, *Basic Respiratory Physiology*, 1st ed. Churchill Livingstone, 1991.

[95] W. Xu, S. Ma, X. Wang, Y. Chiu, and Y.-K. Lee, “A CMOS-MEMS Thermoresistive Micro Calorimetric Flow Sensor With Temperature Compensation,” *IEEE J. Microelectromechanical Syst.*, no. (early access), pp. 1–9, 2019.

[96] J. H. Lienhard V and J. H. Lienhard IV, *A Heat Transfer Textbook*, 4th ed. Mineola, New York: Dover Publications, Inc, 2011.